IN VITRO AND IN VIVO TESTING OF ULTRA-SMALL GOLD NANOPARTICLES AS A NOVEL DRUG DELIVERY PLATFORM FOR ENHANCING THE BRAIN PENETRATION AND RECEPTOR BINDING AFFINITY OF CENTRAL NERVOUS SYSTEM DRUGS
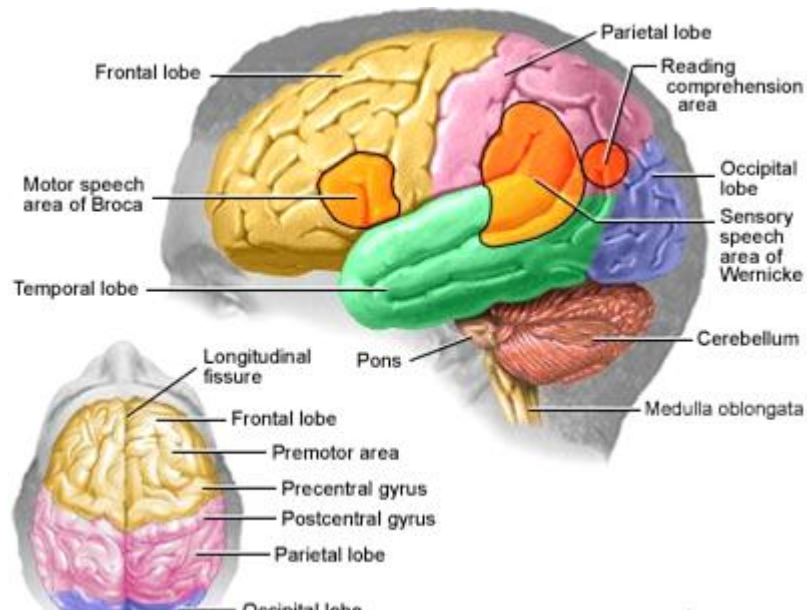
by

Paul Okwabi Nkansah

A dissertation submitted in partial fulfillment
of the requirements for the degree of
Doctor of Philosophy
(Chemical Engineering)
in the University of Michigan
2013

Doctoral committee:

      Professor Nicholas A. Kotov, Chair
      Professor Henry Wang
      Professor Joerg Lahann
      Assistant Professor Mohamed E.H. El-Sayed

Frontal lobe · Parietal lobe · Reading comprehension area · Motor speech area of Broca · Occipital lobe · Sensory speech area of Wernicke · Temporal lobe · Cerebellum · Longitudinal fissure · Pons · Medulla oblongata · Frontal lobe · Premotor area · Precentral gyrus · Postcentral gyrus · Parietal lobe · Occipital lobe

"For every complex problem there is an answer that is clear, simple, and wrong".

- H.L. Mencken

DEDICATION

To Mom & Dad

With love

ACKNOWLEDGMENTS

One of the most difficult tasks I have encountered in preparing this dissertation has been how to best express my gratitude to the faculty, students, family and friends who have helped me on this incredible journey. First and foremost, I would like to thank my thesis advisor, Professor Nicholas Kotov for his mentorship, scientific guidance and infectious optimism throughout the course of my studies at the University of Michigan. I am grateful for his assistance and look forward to life-long friendship and collaboration.

I would like to thank the other members of my dissertation committee. Professor Henry Wang, Professor Joerg Lahann and Professor Mohamed El-Sayed for their critique and the time they took to review my work. I especially like to thank Professor Henry Wang who first recruited me to the University of Michigan and over the years have been a mentor, confidant and sounding board.

I thank the Chemical Engineering Department for allowing me the opportunity to do my graduate studies under very untraditional circumstances. Special thanks to Mrs. Susan Hamlin, Professor Robert Ziff and Professor Phillip Savage for their invaluable counsel and flexibility.

I would like to acknowledge the financial support that I received from Pfizer Inc. In that regard, I especially thank Drs. Richard (Ruey) Hwang, Thomas Hayden, Amy Antipas and Marc Tesconi for helping to make this possible. Special thanks to former and current colleagues

TABLE OF CONTENTS

LIST OF FIGURES

LIST OF TABLES

LIST OF ABBREVIATIONS

Abbreviation	Term
6-MMP	6-methylmercaptopurine
6-MMPR	6-methylmercaptopurine riboside
6-MMPN	6-methylmercaptopurine nucleotides
6-MP	6-mercaptoputine
6-MPN	6-mercaptopurine nucleotides
6-MPR	6-mercaptopurine riboside
6-MPR-AuNPs	6-mercaptopurine riboside gold nanoparticles
6-TU	6-thiouric acid
6-TGN	6-thioguanine nucleotides
ACSF	artificial cerebrospinal fluid
ADHD	attention deficit-hyperactivity disorder
ALL	acute lymphoblastic leukemia
Apo E	apolipoprotein E
Apo A-I	apolipoprotein A-I
AS	astrocytic end-feet
AUC	area under the concentration-versus-time curve
AUC%extra	percentage AUC obtained by extrapolating first and last concentration
AuNPs	gold nanoparticles
BBB	blood-brain barrier
BCSFB	blood- cerebrospinal fluid barrier
BL	basal lamina
cHSA	cationized human serum albumin
CAC	carotid artery cannula
CHO	chinese hamster ovary
CHO-D2S	Chinese hamster ovary cell line expressing human dopamine receptor
CNS	central nervous system
CSF	cerebrospinal fluid
C_0	concentration at time 0 after an intravenous bolus dose
CT	computer tomography
CL	total body clearance
CNS	central nervous system
CED	convection-enhanced delivery
CNT2	cationic amino acid transporter and the adenosine transporter
D_{1-5}	dopamine subtype 1, 2,3,4,5 receptor
D2R	human D2 receptor
DA	dopamine
DOX	doxorubicin
DDC	decarboxylase
EDTA	ethylenediaminetetraacetic aicd
EC	endothelial cell
FITC	fluorescein isothiocyanate

Abbreviation	Term
GLUT1	glucose transporter 1
GSH-OEt	glutathione ethyl ester
GBR12783	1,2-(diphenylmethoxy)ethyl-4-(3-phenyl-2-propenyl)-piperazine
GBM	glioblastoma multiforme
3H	tritiated
HepG2	human hepatocarcinoma
HGPRT;HPRT	Hypoxanthine-guanine phosphoribosyltransferase
IBD	inflammatory bowel disease
ICC	inverted colloidal crystal
IV	intravenous, intravenously
JVC	jugular vein cannula
K_e	elimination rate constant
LAT1	large amino acid transporter 1
LC/MS/MS	liquid chromatography/tandem mass spectrometry
L-DOPA	L-3,4-dihydroxyphenylalanine
LDL	low-density lipoprotein
LDLR	low density lipoprotein receptor
LLOQ	lower limits of quantification
LRP	LDLR-related protein
MAbs	Monoclonal antibodies
MCT1	monocarboxylic acid transporter 1
MDR1	multidrug resistance protein 1
MND	mental and neurological disorder
MRP	multidrug resistance associated proteins
NCEs	new chemical entities
NPs	nanoparticles
OAT	organic anion transporter
P-gp	P-glycoprotein
PLA	Polylactic acid or polylactide
PLGA	poly(lactic-co-glycolic acid
QAbetaCD	quaternary ammonium beta-cyclodextrin (QAbetaCD)
QWBA	quantitative whole-body autoradiography
RMT	receptor-mediated transport
RO	receptor occupancy
S-D	Sprague-Dawley
$t_{1/2}$	terminal elimination half-life
TEM	transmission electron microscopy
Tf	transferrin
TfR	transferrin receptor
TPMT	thiopurine methyltransferase
TJ	tight junction
ULOQ	upper limit of quantification
Vd_{ss}	steady-state volume of distribution
WBSFI	whole-body section fluorescence imaging
XO	xanthine oxidase

ABSTRACT

The endothelial cells of brain capillaries form the so-called blood brain barrier (BBB) and the BBB protects the central nervous system (CNS) from the entry of neurotoxins and blood components. Consequently, more than 98% of all potential CNS drugs fail because they cannot cross the BBB, to gain access to disease targets. Despite significant research efforts in this area, the delivery of drugs across the BBB into the brain remains the Achilles heel in CNS drug development. Therefore in this thesis, we describe the development and testing of ultra-small gold nanoparticles that can traffic drug molecules across the BBB into brain parenchyma, with the potential of also increasing the receptor-binding affinity of drugs. We present compelling results of *in vitro* and *in vivo* studies, combined with imaging and bioanalytical techniques to demonstrate the superior pharmacokinetics, brain penetration, and receptor binding of drugs conjugated to gold nanoparticles (AuNPs).

In chapter one, we provide an introduction to the global impact of CNS diseases and discuss the physiological basis of the CNS. The role of the highly specialized BBB in transporting molecules such as nutrients into the brain, while restricting the uptake of drug candidates, is discussed. Various CNS drug delivery and targeting strategies are described as well as their advantages and limitations. Finally we describe unique features of gold nanoparticles (AuNPs) that make them attractive as drug carriers for CNS delivery.

Chapter two describes a novel CNS drug-delivery strategy involving the conjugation of the anticancer agent 6-mercaptopurine riboside to AuNPs (6-MPR-AuNPs). 6-MPR and its antimetabolites have short half-life due to rapid metabolism by liver xanthine oxidase. The 6-MPR-AuNPs drastically decreased the clearance of 6-MPR from 6190 ± 810 to 22.45 ± 1.95 mL/min/kg. Correspondingly, the half-life of 6-MPR increased from 13.8 ± 5.94 to 44.16 ± 1.98 minutes and the AUC increased (about 100-fold) from 12.45 ± 1.25 to 3695 ± 315 ng/mL·h. Three-dimensional (3D) spheroid culture with human hepatocarcinoma cells confirmed the results of the rat pharmacokinetic studies. Furthermore, studies using rat liver homogenate

revealed that the AuNPs directly inhibited liver xanthine oxidase and can explain the dramatic improvement of the stability of 6-MPR-AuNPs compared to 6-MPR alone.

Chapter three examines the brain penetration of 6-MPR-AuNPs. Using whole-body fluorescence imaging and brain distribution experiments, we present compelling animal data that demonstrate brain uptake of 6-MPR after conjugation to AuNPs. We report on the biodistribution of fluorescein isothiocyanate-labeled 6-MPR-AuNPs (FITC/6-MPR-AuNPs) in rats. Compared to the control groups, the fluorescence intensity of rats injected with FITC/6-MPR-AuNPs was highest in the brain and cerebrospinal fluid (CSF). Tandem to these findings, we also observed that the $AUC_{0.083-0.75h}$ of CNS and plasma were respectively 5.3 and 142-fold higher in rats injected with 6MPR-AuNPs compared to rats given 6MPR alone. Correspondingly, the 6-MPR clearance decreased from 6076 ± 412 to 41.88 ± 3.24 mL/min/kg. Finally, transmission electron microscopy (TEM) of brain specimens provided further direct evidence that 6-MPR-AuNPs penetrated the intact BBB and was distributed into cerebral parenchyma and neuronal cells.

In chapter four, we use dopamine-conjugated AuNPs (DA-AuNPs) to overcome the poor brain permeability of dopamine (DA). In addition, we use receptor binding studies to address the central question of whether or not a drug conjugated to AuNPs will lose its efficacy. Competitive binding studies using human dopamine receptor whole cells revealed that the binding affinity of DA-AuNPs was 10-fold higher than free dopamine. Also, rat *ex vivo* binding studies showed that DA-AuNPs compared to control groups had the strongest affinity to central D2R, producing receptor occupancy(RO) approaching 100% at 1uM dose. Free dopamine achieved only 80% occupancy at 1uM. We investigated the effect of AuNP size on the binding affinity of dopamine, and found that the RO of 5, 15, and 50 nm DA-AuNPs were respectively 90%, 60%, and 20%, whereas 100 and 200nm NPs had RO of only 5%. Furthermore, TEM images of rat brain striata provided evidence that DA-AuNPs indeed penetrated the BBB and was transported into the brain parenchyma.

Finally, in chapter five, key findings of this thesis are summarized and perspectives on future research into brain drug targeting and nanotherapeutics are presented.

CHAPTER 1

GENERAL INTRODUCTION

1.0   BACKGROUND

1.1   Burden of neurological disorders

One out of every three individuals will experience a diagnosable mental and neurological disorder (MND) during their lifetime. [1,2] Despite significant advances in the field, MNDs remain a critical unmet medical need of this century. MNDs comprise a range of central nervous system conditions such as Alzheimer's, multiple sclerosis, Parkinson's disease, diabetic neuropathy, insomnia, migraine, attention deficit hyperactivity disorder, major depressive disorder, schizophrenia, bipolar disorder and epilepsy, that negatively impact mood, behavior, brain function, and cognition. CNS disorders represent five of the top ten causes of disability and constitute greater than 20% of total healthcare spending. The global market for CNS drugs has grown to $78 billion in 2010, from $36.8 billion in 2002 and is expected to rise to $82 billion in 2015.[3] The return on research dollars is low (4.5%) across all therapeutic areas, only second to the combined profits of anesthetics and analgesics (Figure 1-1-1). An aging population along with an increase in life expectancy is expected to increase the incidence of CNS disorders.[4] Chronic neurological disorders such Alzheimer's, Parkinson's disease, and the sequelae of stroke, affect older adults disproportionately and contribute to disability, diminish quality of life, and increased healthcare costs. Stroke and Alzheimer's afflict 30% and 20%, respectively, of persons over 65 years. For Alzheimer's, this rises to 49% of people ages 80 years or more.[5] Alzheimer's and Parkinson's alone, collectively affect approximately 40 million people worldwide and is expected to rise steeply to 115 million by 2050 with an annual cost exceeding $375 billion.[6,7]

1.2   Challenges in developing CNS drugs

Recent advances in biotechnology and pharmaceutical sciences have greatly expanded the number of new drug candidates that are being developed for the treatment of CNS disorders.

Despite this, the development of new medicines to treat diseases of the CNS is one of the most challenging undertakings of today's biopharmaceutical industry. CNS drugs take on average 40-50% longer to market than non-CNS drugs. CNS drugs have a higher attrition rate, 15% compared to 7%, on average, compared to other therapeutic areas.[8] For drugs involving new mechanisms of action, the success rate is very low (Figure 1-1-2).

The high risk of failure for new CNS drugs is linked to the extraordinary complexity of the anatomy and physiology of the human brain, and its pathologies. Part of the problem resides in the incomplete understanding of the underlying pathophysiology and drug targets of most CNS disorders, including multiple sclerosis, Alzheimer's, Huntington's, and Parkinson's disease. Another persisting problem is identifying the dose and schedule which are both efficacious and safe for patients. This difficulty is further aggravated if the drug candidate has a narrow therapeutic window and a validated biomarker is not available.[9] Further complications are presented in the many hurdles that a molecule has to overcome between administration and reaching the target site of action within the CNS. Drug concentration in the brain depends on several factors such as the free plasma concentration, drug half-life, protein binding and distribution within the brain, efflux, and the continual drainage of CSF and brain interstitial fluid.[10] Last and most importantly, the vasculature of the brain which forms the BBB serves as an obstacle to the entry of potential new CNS drugs into the brain. More than 98% of all new CNS drug candidates fail because they cannot cross the BBB in sufficient amounts to exert pharmacological effect.[11,12]

Efforts to design CNS drugs that overcome poor brain uptake, either by manipulating drug chemical properties, or cloaking drug properties in a delivery carrier or promoiety, have proven inadequate.[13] Therefore, there is need for new and effective CNS drug delivery systems that can circumvent the BBB in sufficient quantities. [14,15]
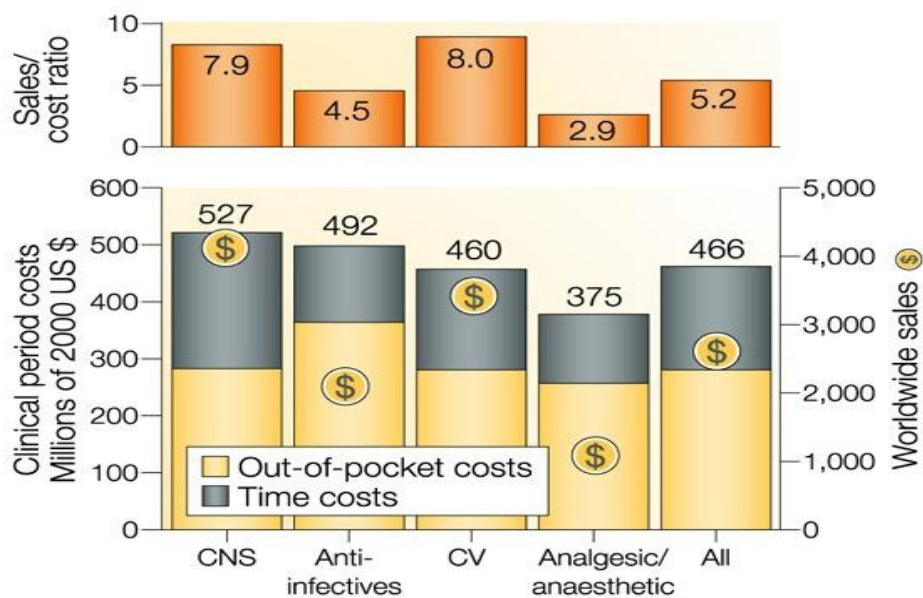
Figure 1-1-1. R&D costs and returns by Therapeutic Category. *DiMasi, J.A.; Grabowski, H.G.; Vernon, J. Drug Information Journal, 38, 211–223, 2004;* Therapeutic area influences drug development costs. *Frantz, S. News and Analysis: Nature Reviews Drug Discovery 2004, 3, 466*
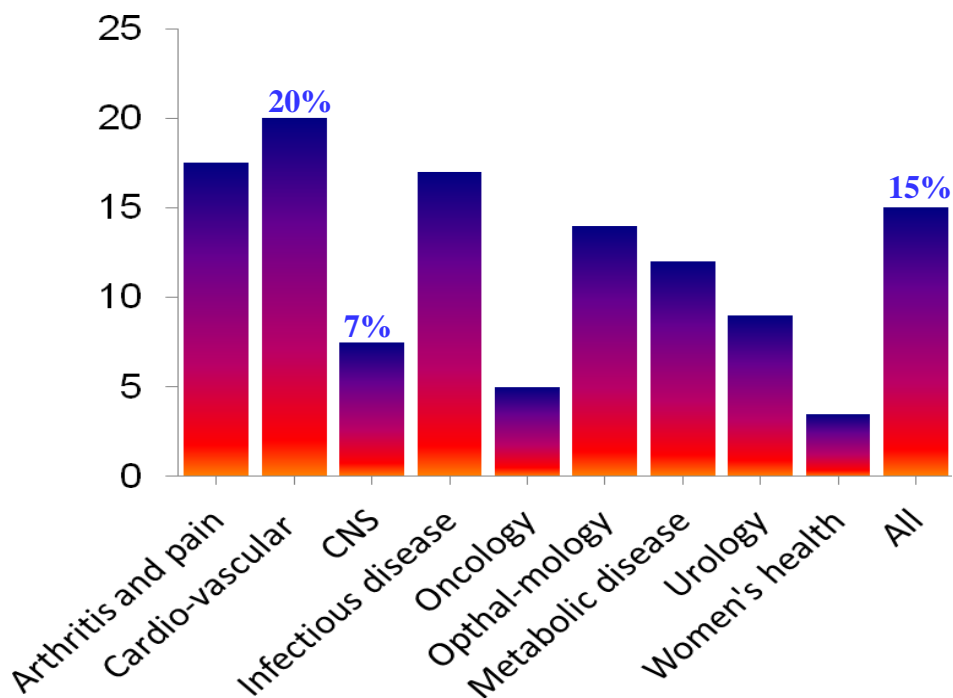
Figure 1-1-2. Probability of Success for New Mechanisms. Adapted from: *Kola and Landis, Nature Review Drug Discovery, 2004 (3):711-715*

2.0   BARRIERS OF THE CENTRAL NERVOUS SYSTEM

The CNS is separated from the peripheral blood circulation by physiological barriers which regulate movement of solutes from blood into the brain and provide a fully autonomous milieu for cells within the CNS. These barriers ensure a constant supply of nutrients and removes waste products from the CNS.[16] However, the CNS barriers also prevent access to cerebral targets for many useful drug molecules circulating in the blood stream. The three major independent barriers within the CNS are the BBB (Figure 1-2-1a), blood-CSF barrier (BCSFB) (Figure 1-2-1b) and arachnoid barrier (Figure 1-2-1c). [17,18] The fetal CSF–brain barrier (Figure 1-2-1d) and adult ependyma are also important (Figure 1-2-1e). Other interfaces with blood and neural tissues are the blood-retinal barrier and the nose-brain barrier. [19,20] The most important transport interface of CNS is however the BBB.

2.1   Blood-brain barrier

Paul Ehrlich (1885) and his student Edwin Goldmann (1913) provided the first experimental evidence of the existence of a barrier between the blood and the brain, which is today known as the BBB. The term "Blut-Hirn-Schranke" or blood-brain barrier was first coined by Lewandowsky. In 1941, Broman proposed that it was the cerebral capillary endothelial cells that contribute the physical barrier function of the BBB and not the astrocytic end feet. This was supported by electron microscopic cytochemical studies performed in 1967 by Reese and Karnovsky.

The current understanding is that the BBB is formed by cerebral endothelial cells sealed together by a very complex network of tight junctions (arrowhead). The BBB is not uniform throughout the brain because the capillaries in the circumventricular organs are fenestrated. The permeability of BBB is modulated by autocrine and paracrine secretions from several types of cells, such as the pericyte, astrocyte, and neurons[21]. The downside of the tightly controlled BBB is that it also limits the transport of therapeutics into the brain. Approximately 98% of the small molecule drugs and nearly 100% of the large molecule (e.g. peptides, proteins and nucleic acids) cannot substantially cross this barrier. [22]

2.2 Blood-cerebrospinal fluid

The blood–CSF barrier (BCSFB) separates choroid plexus blood vessels from CSF and is functionally and morphologically different from the BBB. The BCSFB originates from the tight epithelia cells of the choroid plexus in the ventricles rather than the endothelial cells lining the brain capillaries as is the case of the BBB. Unlike the capillaries that form the BBB, choroid plexus capillaries are fenestrated, forming a nonrestrictive barrier[23]. Notwithstanding its permeability, the blood–CSF barrier does not significantly increase the penetration of drugs into the brain. The epithelial cells have apical tight junctions towards their apical surface that restrict intercellular passage of molecules. Also the surface area of the BCSFB is ca.5000 times less than the BBB[24]. Additionally the BCSFB faces the CSF, not blood, and therefore, the BCSFB is not as important an influx barrier for CNS drugs as the BBB. Therefore, the BBB is generally viewed as having a greater role than the BCSFB in the delivery of CNS medications to the brain.

2.3 Arachnoid barriers

The arachnoid barrier is formed by the epithelium of the meninges and forms the physical barrier between CSF-filled subarachnoid space, dura mater and overlying structures. The arachnoid barrier is the least studied and structurally most complex of all the brain barriers. The blood vessels of the dura are fenestrated and provide little barrier function. However, the outer cells of the arachnoid membrane have tight junctions (arrowheads) and this cell layer is believed to form the physical barrier between the CSF-filled subarachnoid space and overlying structures. Finally, the blood vessels in the arachnoid and on the pial surface have tight junctions with similar barrier characteristics as cerebral blood vessels.

2.4 Cerebrospinal fluid–brain barrier and ependyma

The CSF–brain barrier, a barrier between the CSF and brain parenchyma, has been shown to be a functional barrier present only in early fetal development. In early development, the neuroependymal cells are connected to each other by strap junctions (open arrowheads) that are believed to form the physical barrier restricting the passage of larger molecules such as proteins but not smaller molecules such as sucrose. During later development, the neuroependymal cells

flatten and lose their strap junctions. The adult ventricular ependyma, therefore, does not restrict the exchange of molecules, at least as large as proteins, between CSF and brain.

Table 1-1: Landmarks in the understanding of BBB and development of CNS drug therapy[25,26]

1885	First lumbar puncture to administer cocaine for anesthesia
1885	Concept of BBB indicated by the observation that dyes injected into the vascular system were rapidly taken up by all the organs except the brain.
1900	Coining of the term ''blood–brain barrier'' to describe the phenomenon.
1913	BBB observed to be decreased in the choroid plexus.
1920	Intracerebral distribution of various substances administered systematically was observed.
1927	First injections into the cerebral circulation: contrast materials for cerebral angiography.
1940	Description of vertebral venous plexus and its connection to blood vessels of the brain laid the anatomical basis for use of epidural venous injection for drug delivery to the CNS.
1940s	Tor Broman of Goteborg, Sweden showed that the anatomical substrate of the BBB was the brain capillary wall. This was confirmed by electron microscopy a quarter century later.
1941	Opening of the BBB by pharmacological means.
1947	Stereotactic equipment for guided placement of instruments at selected targets in the depth of the brain for the treatment of movement disorders.
1950s	Electron microscopy used to show lack of extracellular fluid compartment between glia and neurons and this was given as explanation for why substances do not enter the brain.
1954	Injection of a mixture of procaine and alcohol into the globus pallidus of the brain for treatment of movement disorders.
1967	Electron microscopy confirmed brain capillary wall to be the BBB.
1973	First injection of a therapeutic substance (diazepam) into the carotid arteries.
1978	First implantable pump for intrathecal and intraventricular injection of morphine.
1980s	Studies in molecular biology of the BBB. Cloning and sequencing of glucose transporter gene.
1990s	Further development of direct injections of therapeutic substances, including biologics (e.g., gene therapy), into the brain, and development of strategies to overcome the BBB.
1995	Use of nanoparticles for drug delivery across BBB.
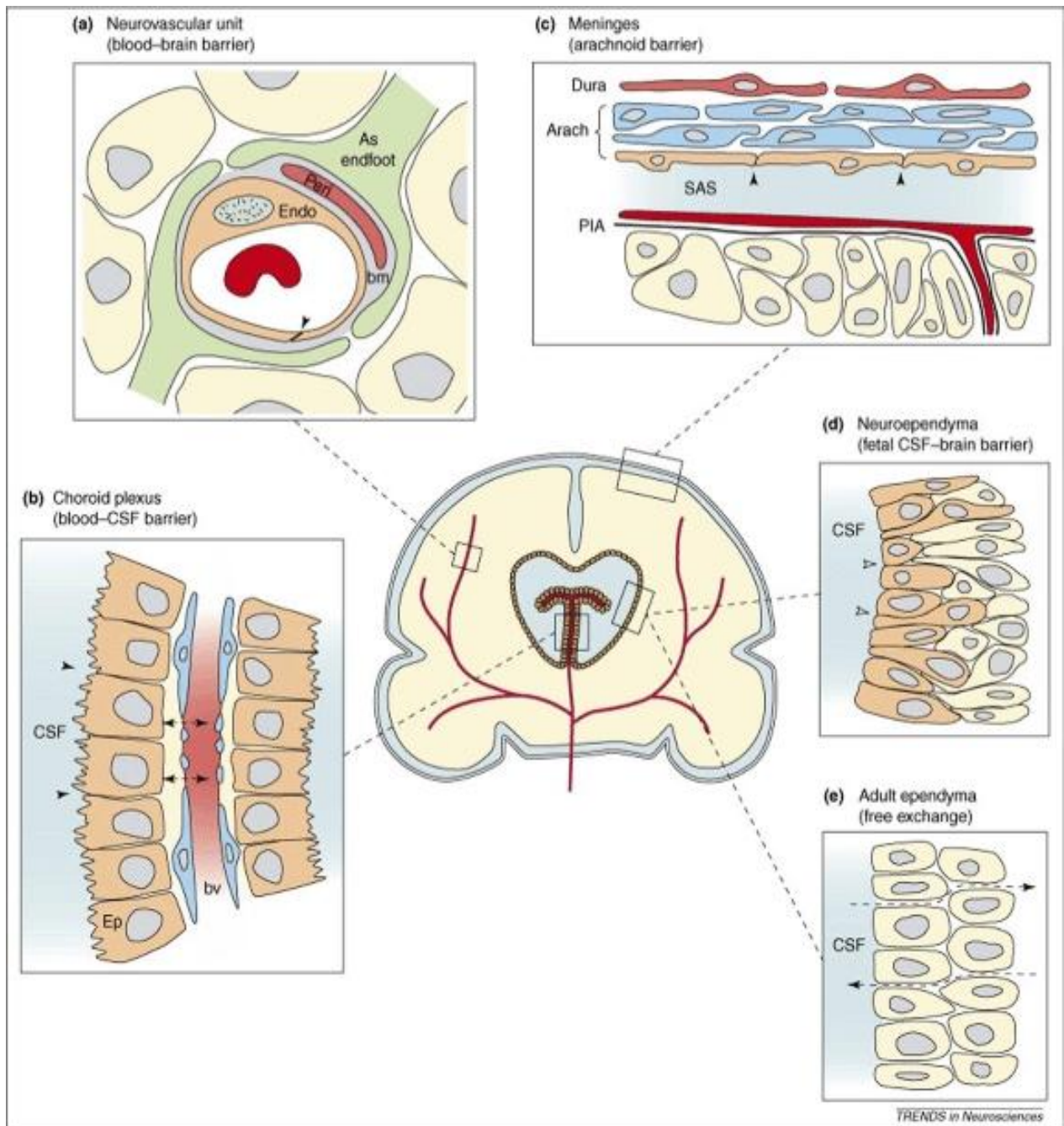
Figure 1-2-1. Schematics of the sites of the barrier interfaces (indicated in orange) in the adult and developing brain. *Saunders, N. Trends Neurosci. 2008, 31(6):279-86.*

3.0   STRUCTURE AND FUNCTION OF THE BLOOD-BRAIN BARRIER

3.1   Blood-brain barrier

The blood-brain barrier is mainly formed by the endothelial cells surrounding the brain capillaries, although other cell types, such as pericytes, astrocytes, and neuronal cells contribute to the formation and maintenance of a functional BBB in the CNS. [27,28] The endothelial cells are completely covered by a basal lamina. The pericytes are embedded within the basal lamina and this covers about 20-30% of the endothelial cells. The basal lamina is surrounded by astrocyte end-feet[29].

The total capillary length of the BBB is 650 km. Every cubic centimeter of cortex contains the amazing sum of 1 km of blood vessels and the surface area is ca. 12 m2 or 100–150 cm2/g brain[30]. The luminal diameter of brain capillaries is 3 mm (mean distance 40 mm) and the capillary volume is 1 ml or ca. 11 ml/g brain. Cerebral blood flow has a transit time through the brain of only 5s. The distance between luminal and abluminal membranes of endothelial cells is only 200 nm, this allows substances to cross the endothelial cells and enter the brain parenchyma within a short time[31,32].

The BBB endothelial cell (BCEC) differs from endothelial cells in the rest of the body by the presence of tight and adherens junctions between the cells, lack of fenestrae, low frequency of pinocytic vesicles, and increased numbers of mitochondria[33].There is also high enzymatic activity in the cells forming the BBB, which can efficiently metabolize bioactive molecules before they cross the BBB and gain access to the brain parenchyma[34]. Furthermore, BBB endothelial cells express several transporter proteins, including P-glycoprotein (P-gp), multidrug resistance associated proteins (MRPs), GluT1, LAT1, the monocarboxylic acid transporter 1 (MCT1), cationic amino acid transporter and the adenosine transporter (CNT2), which affect the transport of molecules into and out of the CNS. [35,36] Figure 1-3-1 represents the schematic illustration of BCECs and associated structures.

3.2   Pericytes

Pericytes are undifferentiated, contractile connective tissues that develop around capillary walls and share the basal membrane with brain capillary endothelial cells. There is approximately one pericyte for every three endothelial cells. [37,38] Pericytes play a regulatory role in brain angiogenesis, structural differentiation of the brain endothelial cells, and formation of endothelial tight junctions. They also contribute to the microvascular vasodynamic capacity and structural stability. [39] Additionally, cerebral pericytes express several enzymes, such as transpeptidase and aminopeptidase, therefore constituting a major component of the metabolic BBB.[40,41] It has also been suggested that cerebral pericytes have phagocytotic potential.[42]

3.3   Astrocytes

Astrocyte cells occupy approximately 99% of the abluminal surface of the brain capillary formed by the endothelial cells and are attached to a basement membrane.[43] Astrocytes are characterized by large nuclei and thick cytoplasmic appendices with cap-like structures known as endfoot. However, endfoot processes are not sealed to each other and small gaps between the astrocytes allow passage of large and hydrophilic molecules. Although astrocytes do not take part in the formation of the physical barrier of the BBB, they are important in the development and maintenance of the BBB. Astrocytes secrete a range of growth factors and cytokines that strongly contribute to the BBB phenotype of endothelial cells, leading to tighter tight-junctions, and the expression of several transporter proteins (e.g. LAT1, GluT1 and P-gp) in the brain endothelial cells. [44] Moreover, the expression of several enzymes at the BBB is induced by astrocytes. Therefore, astrocytes can play a major role in the BBB metabolism.[45]

3.4   Tight junctions

The most important factors responsible for the restriction of the paracellular diffusion across the BBB are the fused junctional complexes which are present between endothelial cells.[46] Tight junctions are large, multiprotein complexes and the structure of the tight junction in the BBB has been found to be the most complex of all such entities in the entire vasculature of the body.[47] The tight junctions between adjacent endothelial cells are 50–100 times tighter than those encountered in peripheral endothelium.[48] In addition to sealing the paracellular route across the

BBB, tight junctions are responsible for the polarization of the endothelial cells, which results in non-uniform distribution of transporters between the luminal and abluminal membranes.[49] In addition to tight junctions, brain capillary endothelial cells are joined by adherens junctions located near the basolateral side of the endothelial cells. Tight junctions and adherens junctions are both needed to form the BBB. [50]
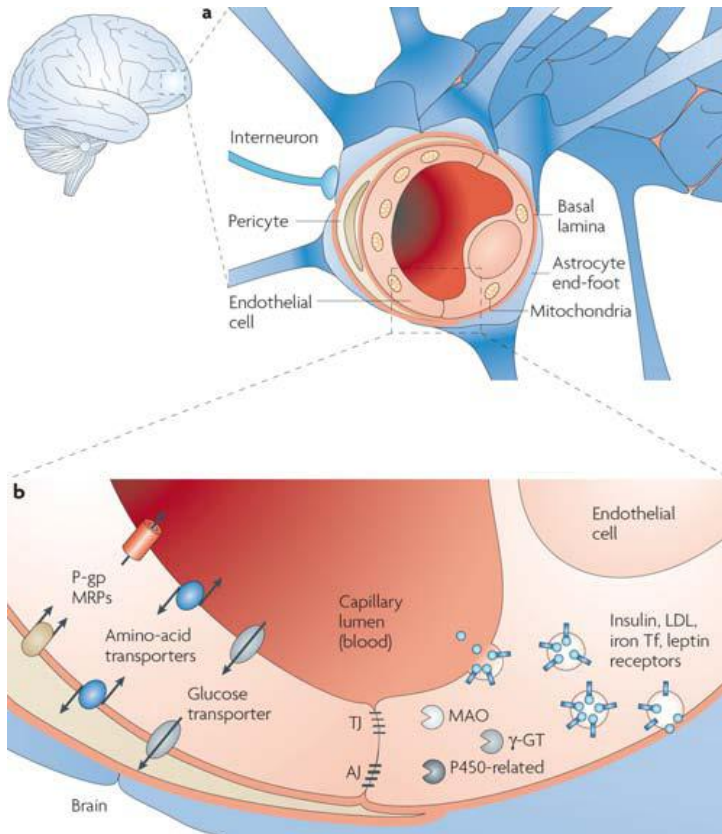
Figure 1-3-1 (a) The BBB is formed by endothelial cells of the cerebral capillaries. The endothelial cells interact with basal lamina, astrocytes, and pericytes to form a functional BBB. (b) Cerebral endothelial cells form complex tight junctions (TJ), and adherens junctions (AJ). The presence of intracellular and extracellular enzymes such as cytochrome P450 endows the BBB with metabolic activity. Specific receptors and efflux transporters are also involved in brain transport. *Cecchelli, R. Modeling of the blood-brain barrier in drug discovery and development. Nature Review Drug Discovory 2007, 650-661.*

4.0   CENTRAL NERVOUS SYSTEM DRUG DELIVERY

Despite the fact that the brain is highly perfused by capillaries, the entry of molecules from blood to brain is governed by the impervious BBB. Drug permeability of the BBB is dependent on a number of parameters such as molecular weight (MW), lipophilicity, pKa, hydrogen bonding as well as biological factors. High molecular weight and hydrophilic drugs tend to fail as CNS drugs because of their poor ability to cross BBB.[51] Paracellular transport of hydrophilic molecules is restricted by the tight junctions present between brain endothelial cells. On the other hand, lipid-soluble molecules with molecular weights below 400Da are able to cross by transcellular diffusion, provided that they are not substrates for efflux transport system. Only a few brain diseases consistently respond to small lipid-soluble molecules.[52]

4.1   Methods for overcoming poor brain uptake of drugs

Several creative methods have been used to get drugs into the brain. These involve direct injection into the brain, using nerves innervating the nasal passages, and opening of BBB tight-junctions. Other methods make use of known endogenous brain transport mechanisms. Transcellular diffusion, carrier-mediated transport, paracellular transport, adsorptive endocytosis and receptor-mediated endocytosis can transport drugs across the BBB (Figure 1-4-1). Targeting ligands, monoclonal antibody and small peptide-vectors or nanoparticles are already being used to enhance receptor-mediated transcytosis of drugs into brain. These methods have limitations which will be discussed below. As such, new brain delivery strategies are needed.[53]

4.1.1   Modifying physicochemical properties of CNS drugs

Passive diffusion across the BBB is believed to be the most common mechanism of CNS drug uptake. However, the importance of transporter mediated brain uptake may be underestimated. [54] Passive diffusion can occur either between the cells (paracellular) or through the cells (transcellular), depending on the physicochemical properties of the solutes. Tight

junctions restrict paracellular transport across the BBB, therefore passive diffusion is restricted to a few molecules which have optimal physicochemical properties.

A simple approach to increase the CNS entry of a polar molecule involves masking the polar functionalities. In practice, lipidization through lipophilic drug analogues often results in diminished therapeutic effect, due to decreased activity or increased toxicity of analogues. [55] However, lipidization through prodrugs (the so-called chemical drug delivery system) offers the possibility for a more efficient CNS delivery of polar drugs without compromising their pharmacological effect or safety. Prodrugs, being more lipophilic than the parent drug, enter the CNS more readily, and are then converted back to the parent drug within the CNS. However, lipophilic prodrugs share some problems with lipophilic drug analogues which limit the utility of this approach. Lipophilic modifications can lead to an increase in molecular weight of the drug, thereby reducing the diffusion through biological membranes. Prodrug lipidization increases permeation across all other biological membranes in the body, leading to marginal increase in brain uptake of the drug, even though the BBB permeability is greatly enhanced.[56] Additionally, high BBB permeability due to increasing lipid solubility is offset by a correspondingly high plasma protein binding which reduces the free fraction of drug needed to provide the driving force across the BBB. Non-specific binding in the brain also exaggerates the distribution volume of drugs in the brain parenchyma, which sustains the blood to brain concentration gradient.[57] However, as only the free fraction of the drug is effective, the high brain uptake due to the non-specific brain tissue binding is futile.

4.1.2   Invasive delivery methods

Invasive delivery circumvents the BBB, resulting in high drug concentrations and half-life in the brain. This approach reduces systemic drug concentrations and side effects, but inevitably requires extremely invasive surgical procedures. Intracerebroventricular (icv) injection, intracerebral (ic) injection, direct implantation of biodegradable vehicles inside brain parenchyma and the use of permeability enhancers to disrupt tight-junctions are the main types of invasive delivery methods.[58] During icv injection, the drug is injected into the CSF. The drug has to diffuse from the CSF to the brain parenchyma via the ependymal barrier. Because of the rapid turnover of the CSF and the slow diffusion rate of drugs, generally only a small amount of

the drug reaches the brain parenchyma. However, icv injection can be effective when local administration of drugs is needed (e.g. treatment of brain tumors) or when the target receptor lies in close proximity to the ependymal surface.[59]

Another invasive injection method is ic injection. Here drugs are injected directly into the brain parenchyma using convection-enhanced delivery (CED). CED relies on a continuous infusion to drive the drug throughout a larger region of tissue at a sufficiently high rate to achieve an additional convective transport of drug. Injectable poly(lactic-co-glycolic acid) (PLGA) and polylactic acid (PLA) microspheres have been widely used to achieve sustained release of drugs at the desired site of the brain. The microspheres are delivered by minimally invasion stereotaxic injection technique.[60] Brain implants of 1,3-bis(2-chloroethyl)-1-nitrosourea-loaded biodegradable polymer wafers (Gliadel®) has demonstrated a novel approach to circumvent the BBB and been tested in Phase III clinical trials, leading to an extensive research interest in this area.[61] Overall, ic injections and drug-releasing implants have turned out to be ineffective because the steady turnover of brain extracellular fluid carries the drug away from the injection site.[62]

Osmotic disturbance of tight-junctions allows drugs to be delivered to the brain by manipulating the BBB tight-junctions. This is achieved by infusion of a hypertonic agent (e.g. mannitol 25%), bradykinin or other cytokines (e.g. histamine) into the carotid artery. The BBB opens for about 30 minutes, presumably by shrinking the endothelial cells and disrupting the tight junctions, allowing the drug to freely diffuse into the brain.[63] However, opening of the BBB makes it possible for harmful substances such as neurotransmitters and circulating toxins to enter the brain as well.[64] Therefore, tight-junction disturbance is restricted mostly for use in terminally ill patients with brain tumors.

4.1.3 Intranasal delivery

Intranasal drug delivery bypasses systemic circulation and the BBB by providing direct access to the brain via the olfactory and trigeminal nerves innervating the nasal passages.[65] Intranasal delivery has been successfully explored for the delivery of small lipophilic molecules like cocaine and morphine. It provides a noninvasive alternative to CNS delivery. The exact mechanism of brain entry via the nasal route remains unclear, but the main technical concern is

increasing the residence time in the nasal cavity for optimal nasal drug absorption. Bioadhesive formulations with active targeting to the olfactory region, as well as controlled release preparations have been investigated extensively for this purpose. Bioadhesive polymer formulations (prepared by low esterified pectins) have the requisite gelling and viscosity properties, and are being used in controlled-release vehicles for intranasal delivery.[66]

4.1.4 Active transport

Active targeting of the BBB represents a promising non-invasive strategy for improving drug delivery to brain. It involves various influx transport systems expressed within the cerebral endothelium. These transport systems include carrier-mediated transport, receptor-mediated endocytosis and adsorptive-mediated endocytosis.

4.1.5 Receptor-mediated transport

Large molecules and particles such as antibodies, lipoproteins, insulin, transferrin, leptin or nanoparticles can be transported into the brain via receptor-mediated transport (RMT).[67] Receptor-mediated drug delivery takes advantage of endogenous transport systems by directly coupling a targeting ligand to the drug. Examples include L-DOPA and gabapentin (using amino acid transporter, LAT), mepyramine and lidocaine (using the organic cation transporter, OCT) and glycosylated morphine (using the glucose transporter, GLUT-1).[68]

One widely characterized BBB receptor is the insulin receptor. Unfortunately, high doses of insulin are required for efficacy, making it an unsafe targeting ligand. Such high doses of insulin have the potential to result in hypoglycemia. Therefore, antibodies including the murine 83-14 monoclonal antibody are being studied for targeting.[69] Other receptors are low density lipoprotein receptor (LDLR) and LDLR-related protein (LRP). These receptors can bind multiple ligands, including low-density lipoprotein (LDL), lactoferrin and apolipoproteins.

The most studied receptor used for BBB targeting is the transferrin receptor (TfR). In contrast to apo-transferrin, the natural TfR ligand (holo-transferrin) has much higher affinity. However, the application is limited because endogenous levels of transferrin are high, resulting in nearly saturated transferrin receptors.[70] A strategy to circumvent endogenous competition of transferrin is to use antibodies directed against the TfR. The most studied TfR-targeted antibody

is the mouse anti-rat monoclonal antibody OX26, which binds to an epitope of the TfR rather than to the transferrin binding site. The monoclonal antibodies (MAbs) serve as a "molecular Trojan horses" to ferry drugs across the BBB.[71]

4.1.6   Adsorptive-mediated endocytosis

Large molecules such as antibodies, proteins, and structures such as nanoparticles can be transported into the brain by adsorptive-mediated endocytosis.[72,73] Adsorptive-mediated endocytosis is initiated by non-specific electrostatic interactions between polycationic substances and negatively charged endothelial cell membranes. Conversely, RMT systems are selective for BBB transport and require initial binding of ligand to receptor on the BBB endothelium.[74]

Adsorptive-mediated endocytosis is rarely used for drug targeting to the brain, because this process also occurs to a large extent in other organs of the body (e.g. liver, kidneys), thereby decreasing brain specificity.[75] Furthermore, the cationic charge may lead to aggregate formation in circulation. However, significant brain targeting using adsorptive-mediated endocytosis has been accomplished using cationized human serum albumin(cHSA) as a transport vector coupled to 3H-biotin.[76]

4.1.7   Carrier-mediated transport

Carrier-mediated transporters facilitate the delivery of hydrophilic molecules and nutrients such as glucose, amino acids, and purine bases to the brain.[77,78] Since carrier-mediated transport systems are typically small and stereospecific, they are not particularly amenable to the transport of large-molecule therapeutics. Carrier-mediated transport relies on molecular carriers present at both the apical (blood) and basolateral (brain) membranes of the BBB. Drugs may be modified such that they closely mimic the endogenous carrier substrates and can be taken up and transported into the brain. Making chemical modifications in such a way that the drug can be recognized by specific transporters, but still maintain therapeutic efficacy, has proven to be very challenging.[79] Furthermore in carrier-mediated transport, the drug has to compete with endogenous substrates for the carriers. Finally the efficiency of receptor-mediated delivery is generally quite low, as the use of a vector in this manner results in only one molecule being delivered per transferrin receptor.[80]

4.1.8 Active efflux transport

The transcellular brain uptake of some small lipophilic solutes is lower than expected given their lipophilicity. The low brain uptake of lipophilic solutes is often due to active efflux proteins, such as P-glycoprotein (P-gp), ABC transporters, Multidrug Resistance-Associated Protein (MRP), organic anion transporter (OAT) and others that remove solutes from endothelial cells. [81,82] The impact of efflux proteins on the brain uptake of CNS drugs is significant since these transporters have a broad range of substrates. Encoded by the multidrug resistance protein 1 (MDR1), P-gp is localized to the luminal membrane of endothelial cells and pumps amphipathic organic cations or neutral compounds out into the capillaries. MRP and OAT pump anions out of the CNS as efflux proteins. [83,84] Transport across the BBB may therefore be increased by inhibiting certain efflux transporters. Inhibition of the Pgp-dependent multidrug resistance functions could improve brain permeability and maintain CNS drug concentrations. P-gp is one of the most studied active efflux transporters.
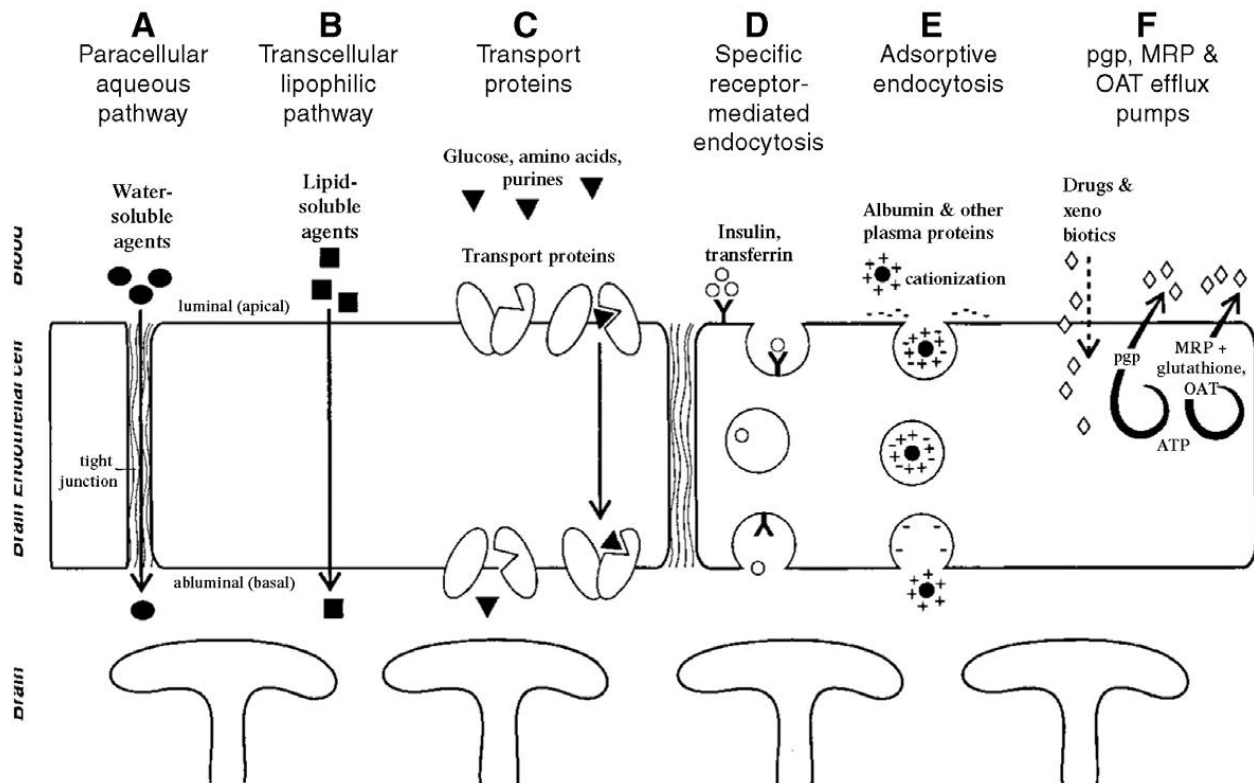
Figure 1-4-1. Transport mechanisms at the BBB. *Abbott, N.J.; Romero, I.A. Transporting therapeutics across the blood-brain barrier. Mol Med Today 1996, 2,106–113.*

5.0   NANOMEDICINE

5.1   Definition and general description

Nanotechnology describes materials and devices that have a functional organization in at least one dimension on the nanometer scale, ranging from a few to about 100 nanometers (figure 1-5-1). [85] The reason for the tremendous potential of nanotechnology in biology and medicine stems from their ability to interact with cells at the molecular level because of their size. [86] Furthermore, nanoscaled materials exhibit interesting bulk mesoscale chemical, biological and physical properties that are not possessed by the molecules alone. Additionally the small size and large surface area of nanocarriers allow them to deliver more drug molecules to disease targets than traditional methods.

The past twenty years have seen a convergence of nanoengineering and biomedical research, giving rise to many new technologies and ideas in medicine. Nanotechnology is poised to drive significant improvements in disease diagnosis and treatment. Various research teams have demonstrated use of nanomaterials for accurate, sensitive, rapid, and often multiplexed detection of disease markers. [87,88] As well, genome and proteome knowledge gained from disease biology has been combined with micro- and nanotechnology in an attempt to discover accurate methods for diagnosis and surveillance.[89] Nanotechnology will also allow new therapeutics to be developed. [90,91] Therapeutic biomolecules may be engineered onto a nanoparticle surface to alter a disease's molecular target. [92] Liposomes, solid lipid nanoparticles, nanogels, dendrimers, albumin nanoparticles, iron-oxide particles, and polymeric nanoparticles have been extensively studied for CNS drug-delivery and diagnostics. [93] Figure 1-5-2 summarizes the different types of nanoparticles used in drug delivery.

5.2   Nanotechnology brain delivery

Interventional methods that open the BBB to deliver drugs to the brain have their drawbacks. Non-specific opening of BBB by chemical agents also allows the entry of toxins and

unwanted molecules.[94] Similarly, invasive techniques such as the use of intracerebral injections require intrusive neurosurgery. Additionally, significant diffusion of the drug away from the injection site occurs, rendering the therapy ineffective.

Nanoparticle mediated drug delivery provides a superior alternative to surgery or altering BBB physiology. Nanoparticles remain intact as they cross the BBB and do not alter the BBB integrity. Also nanoparticle properties such as composition, surface charge, and particle size can be fine-tuned. Furthermore, targeting ligands, native carriers and receptors expressed at the BBB can be used for targeted delivery. For nanoparticle delivery, the drug is directly conjugated to a brain targeting ligand or adsorbed on the particle's surface through electrostatic interaction. The drug can also be encapsulated into nanoparticles which may then be coupled to a ligand on the outside of the particle, enabling BBB-impermeable compounds to enter the brain. [95, 96]

5.2.1 Advances in nanoparticles CNS delivery

In 2009 researchers demonstrated that iron oxide nanoparticles, when coated with polyethylene glycol-grafted chitosan and conjugated to chlorotoxin, crossed the BBB to target brain tumors in a genetically engineered mouse model. The researchers used magnetic resonance, biophotonic imaging and histologic analyses to show sustained retention of chlorotoxin in the tumors. Drug-conjugated iron oxide for diagnosis and treatment of a variety of tumor types in brain continues to gain attention.[97]

Similarly, Gil et al. reported successful delivery of doxorubicin (DOX) across the BBB after intraveneous administration of novel quaternary ammonium beta-cyclodextrin (QAbetaCD) NPs. They showed that the 65-88 nm DOX-QAbetaCD NPs kill U87 cells as effectively as DOX alone, without destroying Bovine Brain Endothelial Cells. As a result, it has been suggested that QAbetaCD NPs are safe and effective brain delivery systems. [98]

Work carried out in the laboratory of Tosi (Modena, Italy) convincingly showed that poly-lactide-co-glycolide (PLGA) NPs engineered with glycopeptide (g7) was effectively delivered to the brain parenchyma of rats after i.v. administration.[99] A dual-targeting drug carrier (PAMAM-PEG-WGA-Tf) was also recently developed based on the PEGylated fourth generation PAMAM dendrimer with Tf and wheat germ agglutinin (WGA) on the periphery, and DOX loaded in the interior. The 20 nm particles PAMAM-PEG-WGA-Tf efficiently inhibited

the growth rate of the C6 glioma cells, while minimizing cytotoxicity of DOX to the normal cells.[100]

Over the last decade, there has been significant development involving receptor-targeted brain delivery with nanoparticles. Endogenous ligands like low-density lipoprotein (LDL), insulin, transferrin (Tf) and folic acid among others have been widely studied[101]. Nanoparticles with covalently bound apolipoprotein E (apo E) or adsorbed apolipoprotein A-I (apo A-I) were reported to enhance brain penetration. Tubocurarine, doxorubicin and amitriptyline when adsorbed onto polybutylcyano-acrylate nanoparticles coated with polysorbate-80, led to a 10-fold increase in its levels in brain. It is postulated that apolipoprotein-E (apo-E) adsorbs onto nanoparticles coated with polysorbates thereby causing endocytosis at the BBB. When the nanoparticles were not coated with surfactants, the particles remained in the blood vessels. [102,103]

Despite these results, a number of weaknesses in these studies have been pointed out. Specifically PBCA is fairly toxic and it is well known that polysorbate-80 will cause BBB disturbance at intravenous doses as low as 3mg/kg.[104] This may in fact explain the increase in brain drug concentration and the effect may be further enhanced when the nanoparticles are coated with polysorbate 80. Furthermore, the authors did not show that the integrity of BBB is maintained during treatment with the polysorbate 80-coated nanoparticles.

Transferrin coupled to nanoparticles has also shown a significant increase in BBB uptake via the trasferrin receptor.[105] However, the potential of OX26 (the monoclonal antibody against trasferrin) in crossing BBB has been presented by the Pardridge group in 1991.[106] Monoclonal antibody known as OX26 recognizes an extracellular domain on the transferrin receptor that is distinct from the transferrin binding site, and does not interfere with endogenous transferrin binding. However, use of antibodies such as OX26 appears to be limited by several factors, including receptor saturation, low dissociation rate of the antibody, recycling of the receptor back to the blood, and hypersensitivity resulting in hyperimmunity against the foreign monoclonal antibody conjugated nanocarrier.[107]

5.3 Gold Nanoparticles

5.3.1 Applications and general description

Gold nanoparticles have a long history of being used in biomedical research. Perhaps owing to centuries-old fascination or to the variety of potential applications that can be imagined, gold nanoparticles have become one of the most common scientifically used nanomaterials. Gold nanoparticles can be synthesized by different protocols to have a variety of shapes and sizes. These include spheroids[108,109], nanorods[110], and many others.[111] This matters because the properties of gold nanoparticles, that make them interesting and scientifically useful, result from their surface-to-volume ratio, their conductance band electron properties (surface plasmon), as well as interaction with their dielectric environment. All of these properties are determined by their size and shape. In this regard, an interesting use of gold particles is molecular sensing based on Raman spectroscopy, and enhancement of Raman signatures by nanoparticle surface plasmons.[112,113] The striking and intense visible range absorbance resulting from their surface plasmon has been used in a variety of diagnostic and therapeutic applications.

Finally, gold nanoparticles make an excellent model system for testing a wide variety of biological hypotheses. This is because they are chemically stable, biocompatible and easy to synthesize and modify. [114,115] As well, the breadth of sizes and shapes that can be synthesized for a single material make it possible to test how these design parameters impact the interaction of nanomaterials and biological systems.

5.3.2 Relevant research

Acute toxicity studies in mice injected with 2.7g/kg of 1.9nm AuNPs showed no signs of adverse events (LD50 was 3200mg/kg) after a year.[116] Biodistribution studies using different sizes of AuNPs show that 4 nm AuNPs accumulate in brain, kidney, liver, spleen and lungs after oral administration to mice.[117] In one study the 10 nm AuNPs were found in liver, spleen, kidney, testis, thymus, heart, lung and brain of rats following an i.v. injection, the 50 and 250 nm particles were only present in liver and spleen.[118] Another study reported extensive biodistribution of 15nm AuNPs compared to the 50, 100 and 200nm particles.[119]

Direct comparison of these studies is difficult because of differences in the experimental designs. However it appears that there is a trend toward high biodistribution for smaller (4–15nm) particles compared to their larger (>50 nm) counterparts. Interestingly, using Cysteine coated (CdSe)ZnS quantum dots(QDs), Choi et al. have also reported that hydrodynamic diameters less than 5.5 nm provide optimal renal excretion of QDs (Figure 1-5-3).[120] The authors also reported that zwitterion (cysteine) or neutral (polyethylene glycol) coatings prevented liver uptake unlike charged particles. These findings suggest that hydrophilic, near-neutral particles of less than 5.5 nm represent the optimal characteristics to guanrantee minimal RES uptake and high renal clearance of non-biodegradable nanoparticles. This work also establishes that particle size, rather than charge and surface chemistry most influenced the clearance of nanoparticles.

Interestingly in addition to BBB permeation limitation, brain microvasculature endothelia also present an electrostatic barrier at physiologic pH. The negative electrostatic charge is created by surface expression and adhesion of the glycocalyx residues: proteoglycans, sulfated mucopolysaccharides, and sulfated and sialic acid-containing glycoproteins and glycolipids.[121] The anionic nature of the endothelium repels anionic molecules, and cationic molecules have been shown to occupy anionic areas at the BBB endothelium. Increasing BBB permeability, presumably by adsorptive transport or tight junction disruption by cationic molecules has been described.[122] Cationized NPs have been shown to increase distribution to the cerebral parenchyma compared to anionic and neutral NPs, owing to this interaction.[123]

In vitro experiments conducted by Podsiadlo et al. found that 5nm AuNPs bearing 6-mercaptopurine riboside (6-MPR) significantly reduced the growth of K562 leukemia cells compared to free 6-MPR(Figure 1-5-4a). Using laser confocal microscopy, the authors also found that when cells were incubated at 37ºC (Figure 1-5-4b) with fluorescein isothiocyanate (FITC)-6MPR-AuNPs, there was a gradual increase in fluorescence inside the cells which was not observed for cells incubated at 4ºC (Figure 1-5-4c).[124] This result points to active transport or endocytosis of AuNPs into cells.
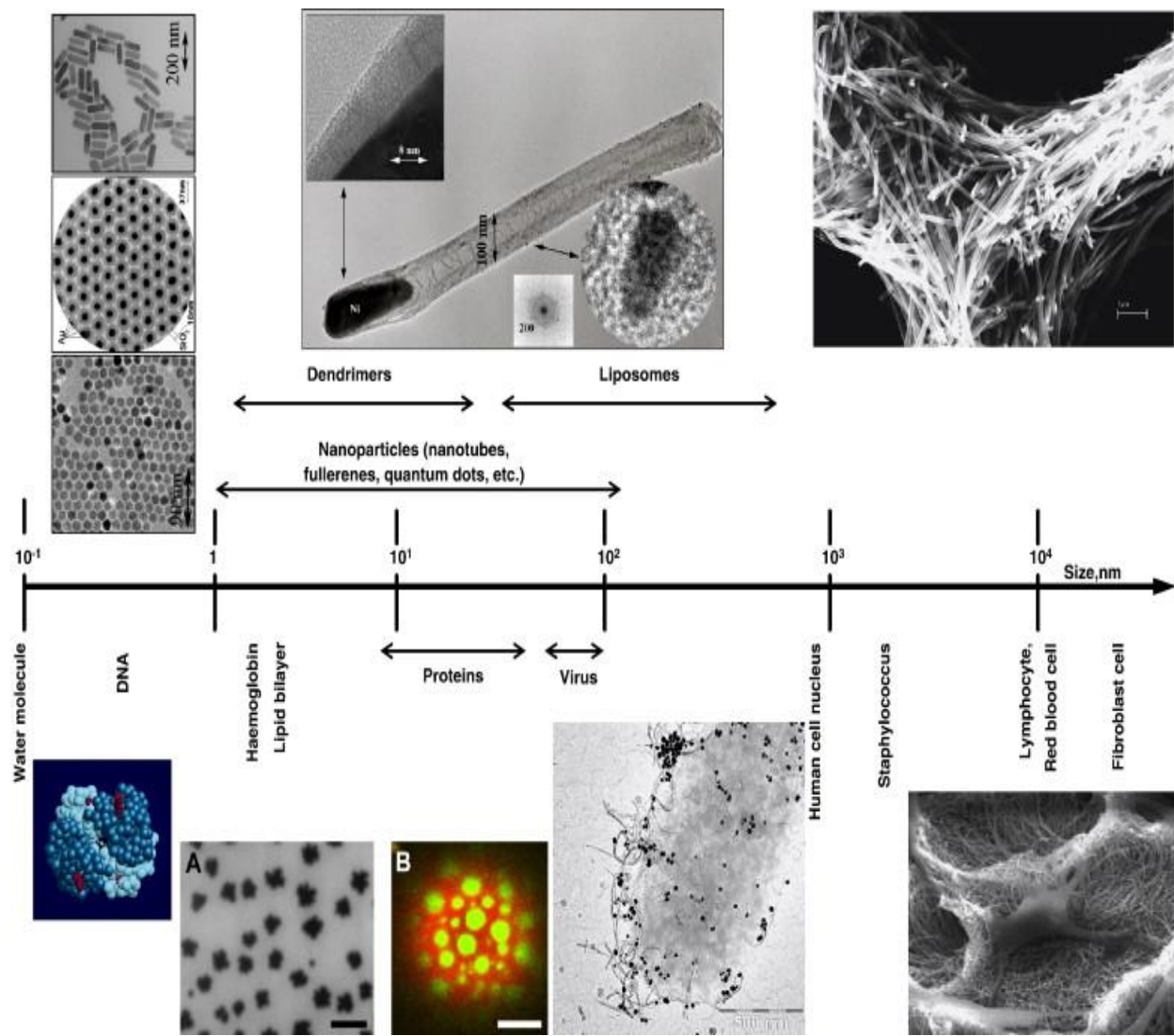
Figure 1-5-1. Structures on the nanoscale and relative scale of nanotechnology. Nanoscale overlaps with that of biomedically relevant classes of biomolecules, viruses and small cells. *www.nih.gov*
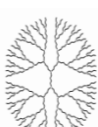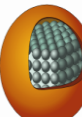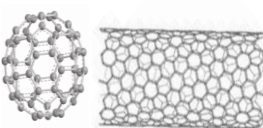
Type	Definition	Schematic
Liposomes	Liposomes are vesicles composed of one or more bilayers of amphiphatic lipid molecules enclosing one or more aqueous compartments.	
Micelles	Micelles are self-assembling nanosized colloidal particles with a hydrophobic core and hydrophilic shell currently used for the solubilization of various poorly soluble pharmaceuticals.	
Nanoemulsion	Nanoemulsions are emulsions with droplet size in the nanometer scale. Emulsion is a thermodynamically unstable system consisting of at least two immiscible liquid phases, one of which is dispersed as globules, in the other liquid phase, stabilized by the presence of an emulsifying agent.	
Dendrimers	Dendrimer is a polymer in which the atoms are arranged in many branches and sub-branches along a central backbone of carbon atoms.	
Metal colloids	Metal colloids refers to a state of subdivision, that the molecules or polymolecular particles dispersed in a medium have at least in one direction a dimension between 1 nm and 1μm, i.e. silver, gold, and iron oxide.	
Quantum dots	Nanoparticle that exhibits size-dependent electronic and optical properties due to quantum confinement.	
Fullerenes, Carbon nanotubes	Fullerene: Closed cage structure having more than 20 carbon atoms consisting of three-coordinate carbon atoms. Carbon nanotube refer to a seamless tube constructed from graphene than can be either a single-wall or multi-wall carbon nanotube compromising multiple concentric tubes .	

Figure 1-5-2. Drug Delivery Nanoparticles *(courtesy of Sadrieh, N. Office of Pharmaceutical Science, CDER/FDA)*
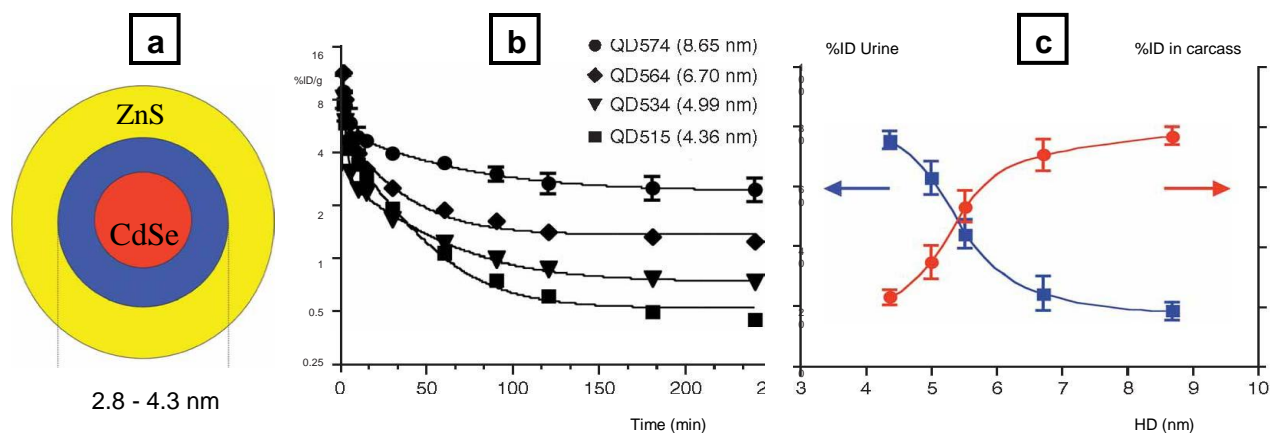
Figure 1-5-3. (a) Compositions of CdSe/ZnS quantum dots with DHLA (anionic), cysteamine (cationic), cysteine (zwitterionic) and DHLA-PEG (neutral) coatings. (b) Plasma concentration (%ID/g) of different sizes of 99mTc-labeled quantum dots after intravenous injection into CD-1 mice. (c) Renal clearance (blue curve) and carcass retention (red curve) of 99mTc-QDs of various hydrodynamic diameters 4 h after intravenous injection into CD-1 mice (*Choi, H.S.; Liu W. Renal clearance of quantum dots, Nat Biotechnol. 2007, 25(10), 1165-70*)
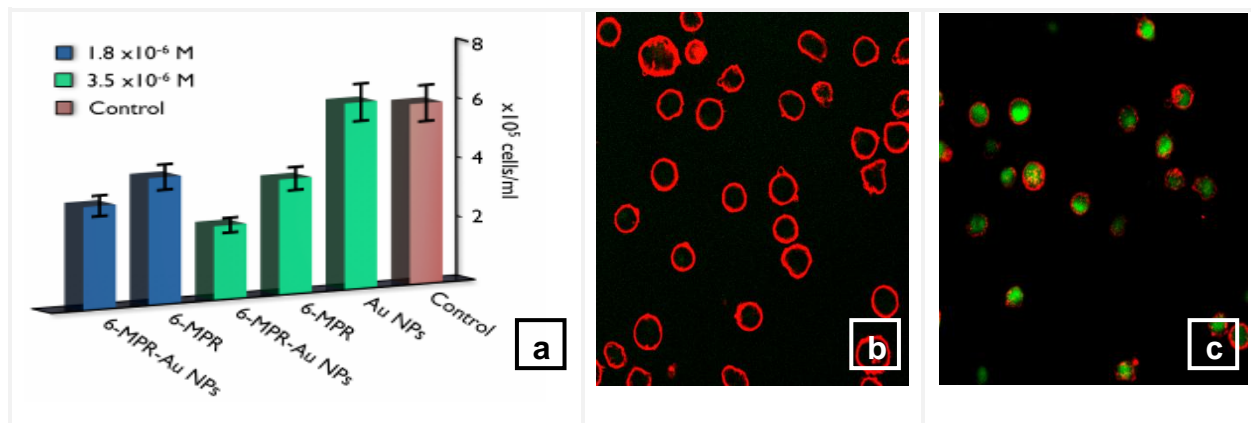
Figure 1-5-4. (a) Cell count of K562 leukemia cells after 72h of incubation with 6MPR (a) Laser scanning confocal micrograph of K-562 cells following incubation at 37 °C with FITC-labeled 6-MPR/Cys-Au NPs for (b) 0 hours, (c)16 hours (FITC: green, FM 4-64 membrane dye: red) (*Podsiadlo, P. Langmuir 2008, 24, 568-574*)

6.0 PROBLEM STATEMENT, OBJECTIVES AND SCOPE OF THESIS

6.1 Problem Statement

In recent years drug development has focused on optimizing drug-target protein interactions. This has lead to the development of large molecules that cannot cross the BBB. More than 98% of all potential new CNS drugs fail because they cannot cross the BBB to gain access to disease targets. [125] Therefore achieving BBB penetration remains a significant hurdle to successfully prosecuting CNS targets.

As described in earlier sections of this thesis, several CNS delivery strategies have been attempted. However an effective brain delivery system is still lacking. The most effective method to-date involves direct injection of drug into the brain. Owing to the risks associated with surgery or altering BBB physiology, nanoparticle mediated-targeting is gaining enormous interest as an effective alternative to delivering drugs to the brain.

Nanoparticle drug delivery systems typically involve direct coupling or coating of targeted BBB receptor ligands to nanoparticles. However the majority of targeted receptors are not only expressed on brain endothelial cells, but elsewhere in the body. As a result, it is difficult for high quantities of nanoparticles and their payload to reach the brain. Additionally, carrier transporters are stereospecific and few. Therefore, only a limited number of substances can potentially be delivered via carrier transporters. New targeting carriers are urgently needed to efficiently deliver drugs to the brain. In this thesis we describe preparation, characterization and multimodal testing of novel, non-toxic, excretable small gold nanoparticles that can traffic drug molecules across the BBB into the brain parenchyma, without the need for BBB-receptor ligands. The approach relies on the unique properties of small gold nanoparticles to cross the BBB and interact with cells.

6.2 Objectives and scope

The primary objective of this thesis is to develop and evaluate the novel use of gold nanoparticles as a drug vector for effective delivery of drugs into the brain. However, BBB

penetration of drug molecules alone does not guarantee optimum brain delivery. The optimum CNS drug delivery system is nearly always the best compromise among competing physicochemical and physiological factors. Therefore, the second objective of this thesis is to evaluate the effect of gold nanoparticles on drug pharmacokinetics such as half-life, clearance, and plasma concentrations. These parameters are important to the development of proper CNS drug therapy. Finally in this thesis we address the central question of whether or not gold nanoparticles conjugated to a drug molecule will exhibit inferior receptor binding and potency, compared to the naive drug molecule. Additionally, this research provides a drug-delivery tool for testing future CNS drug candidates that otherwise could not be evaluated due to lack of BBB permeability. The research provides critical conceptual data for more advanced testing of AuNPs.

6.2.1   Model compounds

6-Mercaptopurine riboside is an antineoplastic agent used in the treatment of lymphoblastic leukemia (ALL), Inflammatory Bowel Disease (IBD) and other diseases.[126] 6-Mercaptopurine riboside was however chosen as a model compound for this study because it has poor brain penetration. In addition, 6-MPR has the added complication of being rapidly metabolized by the liver enzyme xanthine oxidase. 6-MPR is however easy to detect by UV-detector or mass spectrometry and its thiol functional group makes it easy to conjugate to gold nanoparticles. Finally, 6-mercaptopurine is a well established therapy for ALL. Therefore, enabling brain uptake of 6-MPR has the potential of advancing novel therapeutic uses in the treatment of brain cancer and leukemic meningitis.[127]

Dopamine is a neurotransmitter that helps control the brain's reward and pleasure centers. Dopamine also regulates movement, emotional responses, and a number of other important physiological functions. Dopamine was chosen as a model compound for the receptor binding experiments in this thesis, because of its poor BBB penetration and for the crucial role dopamine plays in many CNS disease mechanisms.[128] Dopamine has been implicated in the mediation of schizophrenia, depression, Parkinson's disease and others. Furthermore, the existence of dopamine-receptor binding is well understood and allows for quantitation of receptor binding.

REFERENCES

1   Kessler, R.; Angermeyer, M.; Anthony, J.; De Graaf, R. Lifetime prevalence and age-of-onset distributions of mental disorders in the World Health Organization's World Mental Health Survey Initiative. World Psychiatry. 2007, 6(3), 168–176.

2   Demyttenaere, K.; Bruffaerts, R.; Posada-Villa, J.; Gasquet, I.; Kovess, V.; Lepine, J.P. Prevalence, severity, and unmet need for treatment of mental disorders in the World Health Organization World Mental Health Surveys. JAMA 2004, 291(21), 2581-90.

3   GBI Research, RXUSA, ZenRx, MedScape, Company Annual Reports, FDA, Pharmaceuticals and Medical Devices Agency (PMDA), European Medicines Agency (EMEA), Orange book, JAPIC.

4   Riggs, J.E. Age specific rates of neurological disease. In: Hof PR, Mobbs CV, editors. Functional Neurobiology of Aging. San Diego: CA Press: Academic Press 2001.

5   Alzheimer's Association, 2012 Alzheimer's Disease Facts and Figures, Alzheimer's & Dementia, Volume 8, Issue 2.

6   Hy, L.X.; Keller, D.M. Prevalence of AD among whites: a summary by levels of severity. Neurology 2000, 55, 198-204.

7   Campion, D.; Dumanchin, C.; Hannequin, D. Early-onset autosomal dominant Alzheimer disease: prevalence, genetic heterogeneity, and mutation spectrum. Am J Hum Genet 1999, 65, 664-670.

8   Frantz, S. Therapeutic area influences drug development costs. Nature Reviews Drug Discovery 2004, 3, 466.

9   Gomez-Mancilla, B.; Marrer, E.; Kehren, J.; Kinnunen, A.; Imbert, G.; Hillebrand, R.; Bergström, M.; Schmidt, M.E. Central Nervous System Drug Development: An Integrative Biomarker Approach toward Individualized Medicine. NeuroRx 2005, 2(4), 683–695.

10   Jeffrey, P.; Summerfield, S. Assessment of the blood-brain barrier in CNS drug discovery. Neurobiol Dis. 2010, 37(1), 33-37.

11   Palmer, A.M.; Stephenson, F.A. CNS drug discovery: challenges and solutions. Drug News Perspect 2005, 18(1), 51-57.

12   Pardridge, W.M. Why is the global CNS pharmaceutical market so under-penetrated? Drug Discov Today. 2002, 7, 5–7.

13   Reichel, A. Addressing central nervous system (CNS) penetration in drug discovery: basics and implications of the evolving new concept. Chem Biodivers. 2009, 6(11):2030-49.

14   Liu, X.; Chen, C. Strategies to optimize brain penetration in drug discovery. Curr Opin Drug Discov Devel. 2005, 8(4), 505-12.

15   Greig, N.H.; Brossi, A.; Pei, X.F.; Ingram, D.K.; Soncrant, T.T. Designing drugs for optimal nervous system activity. In New Concepts of a Blood-brain Barrier. Edited by Greenwood J, Begley DJ, Segal MB. New York: Plenum Press. 1995, 251-264.

16   Abbott, N.J.; Patabendige, A.A.; Dolman, D.E; Yusof, S.R.; Begley, D.J. Structure and function of the blood-brain barrier. Neurobiol Dis. 2010, 37(1), 13-25.

17   Ballabh, P.; Braun, A.; Nedergaard, M. The blood-brain barrier: an overview: structure, regulation, and clinical implications. Neurobiol Dis. 2004, 16(1), 1-13.

18   Begley, D. J. ABC transporters and the blood-brain barrier. Curr Pharm Des, 2004b. 10, 1295–1312.

19   De Boer, A.G.; Gaillard, P.J. Drug targeting to the brain. Annu Rev Pharmacol Toxicol. 2007, 47: 323-355.

20 Malhotra, M.; Prakash, S.; Targeted Drug Delivery Across Blood-Brain-Barrier Using Cell
    Penetrating Peptides Tagged Nanoparticles, Current Nanoscience. 2011, 7(13) 81-93.

21 Rubin, L.L.; Staddon, J.M. The cell biology of the blood-brain barrier. Ann. Rev. Neurosci. 1999, 22,
    11-28.

22 Begley, D.J. Delivery of therapeutic agents to the central nervous system: the problems and the
    possibilities. Pharmacol Ther. 2007, 104, 29-45.

23 Dohgu, S.; Takata, F.; Matsumoto, J.; Oda, M.; Harada, E.; Watanabe, T.; Autocrine and paracrine
    up-regulation of blood–brain barrier function by plasminogen activator inhibitor-1. Microvascular
    Research 2011, 81, 103–107

24 Davson, H. The Blood–Brain Barrier, The Structure and Function of Nervous Tissue. 1972, 321-445.

25 Jain, K.K. Drug Delivery in Central Nervous System Diseases - technologies, markets and
    companies. PharmaBiotech Report 2013, 1-349.

26 Jain, K.K. Strategies and technologies for drug delivery systems. Trends in Pharmacological Sciences
    1998, 19, 155-157.

27 Saunders, N.R.; Ek, C.J.; Habgood, M.D.; Dziegielewska, K.M. Barriers in the brain: a renaissance.
    Trends Neurosci. 2008, 31(6), 279-86.

28 Brightman, M.W.; Reese, T.S. Junctions between intimately apposed cell membranes in the
    vertebrate brain. J Cell Biol. 1969, 40(3), 648-77.

29 El-Khoury, N.; Braun, A.; Hu, F.; Pandey, M.; Nedergaard, M.; Lagamma, E.F.; Ballabh, P.
    Astrocyte end-feet in germinal matrix, cerebral cortex, and white matter in developing infants. Pediatr
    Res. 2006, 59(5), 673-679.

30 Friedemann, U. Blood-brain barrier. Physiol Rev 1942, 22, 125–145.

31 Pardridge W.M. The blood-brain barrier: bottleneck in brain drug development. NeuroRx 2005; 2:
    3–14.

32 Cornford, E. M.; Shigeyo, H. Localization of Brain Endothelial Luminal and Abluminal Transporters
    with Immunogold Electron Microscopy NeuroRx. 2005 2(1): 27–43

33 Kaur, C.; Ling, E.A. Blood brain barrier in hypoxic-ischemic conditions. Curr Neurovasc Res. 2008,
    5(1),71-81.

34 Schulze, C., Firth, J.A. Immunohistochemical localization of adherens junction components in blood-
    brain barrier microvessels of the rat. J Cell Sci. 1993,104(3), 773-782.

35 Gynther, M.; Laine, K.; Ropponen, J.; Leppanen, J.; Mannila, A.; Nevalainen, T. Large neutral
    amino acid transporter enables brain drug delivery via prodrugs. J.Med.Chem. 2008, 51, 932-936.

36 R.A., Hawkins ; J. R.,Viña; Darryl, R. Peterson, D. R.; O'Kane, R.; Mokashi, A.; Ian, A. Simpson, I.
    Amino acid transport across each side of the blood-brain barrier in Amino Acids in Nutrition and
    Health (J.P.F. D'Mello ed), CABI, Oxford, 2011,191-214.

37 Allt, G.; Lawrenson, J.G. Pericytes:cell biology and pathology. Cells Tissues Organs 2001, 169, 1-11.

38 Kim, J.A.; Tran, N.D.; Li, Z.; Yang, F.; Zhou, W.; Fisher, M.J. Brain endothelial hemostasis
    regulation by pericytes. J. Cereb. Blood Flow Metab. 2006, 26, 209–217.

39 Al Ahmad, A.; Gassmann, M.; Ogunshola, O.O. Maintaining blood–brain barrier integrity: pericytes
    perform better than astrocytes during prolonged oxygen deprivation. J. Cell. Physiol. 2009, 218, 612–
    622.

40 Ramsauer, M.; Kunz, J.; Krause, D.; Dermietzel, R. Regulation of a Blood-Brain Barrier-Specific
    Enzyme Expressed by Cerebral Pericytes (Pericytic Aminopeptidase N/pAPN) Under Cell Culture
    Conditions. J. Cerebral Blood Flow & Metabolism 1998, 18, 1270–1281.

41 Risau W.; Dingler, A.; Albrecht, U.; Dehouck, M-P.; Cecchelli, R. Blood-brain barrier pericytes are the main source of glutamyltranspeptidase activity in brain capillaries. J Neurochem 1992,58, 667-672.

42 Dore-Duffy, P.; Katychev, A.; Wang, X.; Van Buren, E. CNS microvascular pericytes exhibit multipotential stem cell activity. J Cereb Blood Flow Metab. 2006,26(5), 613-24.

43 Bernoud, N., Fenart, L., Benistant, C., Pageaux, J.F., Dehouck, M.P., Moliere, P., Lagarde, M., Cecchelli, R., Lecerf, J. Astrocytes are mainly responsible for the polyunsaturated fatty acid enrichment in blood–brain barrier endothelial cells in vitro. J. Lipid Res.1998, 39, 1816–1824.

44 Jarkko, R.; Krista, L.; Mikko, G.; Jouko, S. Prodrug Approaches for CNS Delivery. AAPS J. 2008 10(1), 92–102.

45 Sidoryk-Wegrzynowicz, M.;Wegrzynowicz, M.; Lee, E.; Bowman, A.; Aschner, M. Role of Astrocytes in Brain Function and Disease. Toxicol Pathol January 2011, 39, 115-123.

46 Farquhar, M.G.; Palade, G.E. Junctional complexes in various epithelia. J Cell Biol 1963,17, 375-412.

47 Schneeberger, E.E.; Lynch, R.D. The tight junction: a multifunctional complex. Am J Physiol Cell Physiol 2004, 286, 6, 1213-1228.

48 Bernacki, J.; Dobrowolska, A.; Nierwinska, K.; Malecki, A. Physiology and pharmacological role of the blood-brain barrier, Pharmacol.Rep. 2008, 60, 600-622.

49 Nag, S. Morphology and molecular properties of cellular components of normal cerebral vessels, in: Nag S (Ed.). The Blood-Brain Barrier: Biology and Research Protocols, first edition, Humana Press, Totowa, New Jersey, 2003, 3-36.

50 Huber, J.D.; Egleton, R.D.; Davis, T.P. Molecular physiology and pathophysiology of tight junctions in the blood-brain barrier, Trends Neurosci. 2001, 24, 719-725.

51   Banks, W. A. Characteristics of compounds that cross the blood-brain barrier. BMC Neurology 2009, 9, (Suppl 1), S3

52 Pardridge, W.M. CNS drug design based on principles of blood-brain barrier transport, J.Neurochem. 1998, 70, 1781-1792.

53 De Boer, A.G.; Gaillard, P.J. Strategies to improve drug delivery across the blood-brain barrier. Clin Pharmacokinet. 2007, 46(7), 553-576.

54 Pardridge, W.M. Blood-brain barrier delivery, Drug Discovery Today. 2007, 12, 54-61.

55 Rautio, J.; Laine, K.; Gynther, M.; Savolainen, J. Prodrug approaches for CNS delivery. AAPS J. 2008, 10(1), 92-102.

56 Rautio, J.; Kumpulainen, H.; Heimbach, T.; Oliyai R.; Oh, D.; Järvinen, T.; Savolainen, J. Prodrugs: design and clinical applications. Nat. Rev. Drug Discov. 2008, 7, 255-270.

57 Vertuani, S. Progress in drug delivery to the central nervous system by the prodrug approach. Molecules 2008, 13, 1035-1065.

58 Gabathuler, R. Approaches to transport therapeutic drugs across the blood–brain barrier to treat brain diseases. Neurobiology of Disease 2010, 37, 48–57.

59 Pardridge, W.M. Drug targeting to the brain. Pharma. Res. 2007, 24, 1733–1744.

60 Garbayo, E.; Montero-Menei, C.N; Ansorena, E.; Lanciego, J. L.; Aymerich, M.S.; Blanco-Prieto, M.J. Effective GDNF brain delivery using microspheres-A promising strategy for Parkinson's disease 2009,135, 119-126.

61 Bobo, R.H.; Douglas, W.; Akbasak, A.; Morrison, P.F.; Dedrick, R.L.; Oldfield, E.H. Convection-enhanced delivery of macromolecules in the brain. Proc. Natl. Acad. Sci. 1994, 91, 2076–2080.

62 Vandergrift, W.A.; Patel, S.J.; Nicholas, J.S.; Varma, A.K. Convection-enhanced delivery of immunotoxins and radioisotopes for treatment of malignant gliomas. Neurosurg. 2006, 20 (4), E13.

63 Kroll, R.A.; Neuwelt, E.A.; Outwitting the blood–brain barrier for therapeutic purposes: osmotic opening and other means. Congr. Neurol. Sur. 1998, 42, 1083–1099.

64 Fortin, D.; Gendron, C.; Boudrias, M.; Garant, M.P. Enhanced chemotherapy delivery by intraarterial infusion and blood–brain barrier disruption in the treatment of cerebral metastasis. Cancer 2007, 109, 751–760.

65 Dhuria, S.V.; Hanson, L.R.; Frey W.H. Intranasal delivery to the central nervous system: mechanisms and experimental considerations, J.Pharm.Sci. 2010, 99, 1654-1673.

66 Ali, J.; Ali, M.; Baboota, S.; Sahani, J.K.; Ramassamy, C.; Dao, L. Potential of nanoparticulate drug delivery systems by intranasal administration, Curr.Pharm.Des. 2010, 16, 1644-1653.

67 Jones, E.S. Blood–Brain Barrier Transport of Therapeutics via Receptor-Mediation, Pharmaceutical Research. 2007, 24, 1759-1771.

68 Pardridge, W.M. Drug and gene targeting to the brain via blood–brain barrier receptor-mediated transport systems, Int. Cong. Ser. 2005, 49, 49–62.

69 Lee, H.J.; Engelhardt, B.; Lesley, J.; Bickel, U.; Pardridge, W.M. Targeting Rat Anti-Mouse Transferrin Receptor Monoclonal Antibodies through Blood-Brain Barrier in Mouse, J Pharmacol Exp Ther. 2000, 292, 1048-1052.

70 Ulbrich, K.; Hekmatara, T.; Herbert, E.; Kreuter, J. Transferrin- and transferrin-receptor antibody modified nanoparticles enable drug delivery across the blood-brain barrier (BBB). European Journal of Pharmaceutics and Biopharmaceutics 2009, 71, 251-256.

71 Kissel, K.; Hamm, S.; Schulz, M.; Vecchi, A.; Garlanda, C.; Engelhardt, B. Immunohistochemical localization of the murine transferrin receptor (TfR) on blood-tissue barriers using a novel anti-TfR monoclonal antibody, Histochem.Cell Biol. 1998, 110, 63-72.

72 Rooy, I. ; Cakir-Tascioglu, S.; Hennink, W.; Storm, G.; Schiffelers, R.; Mastrobattista, E. In Vivo Methods to Study Uptake of Nanoparticles into the Brain. Pharm Res. 2011, 28(3), 456–471.

73 Brightman, M.W.; Reese, T.S. Junctions between intimately apposed cell membranes in the vertebrate brain. J Cell Biol. 1969, 40(3), 648-677.

74 Bickel, U.; Yoshikawa, T.; Pardridge, W.M. Review Delivery of peptides and proteins through the blood-brain barrier. Adv Drug Deliv Rev. 2001, 46(3) 247-79.

75 Kumagai, A.K.; Eisenberg, J. B.; Pardridge, W.M. Absorptive-mediated endocytosis of cationized albumin and a beta-endorphin-cationized albumin chimeric peptide by isolated brain capillaries. Model system of blood-brain barrier transport. J Biol Chem. 1987, 262(31), 15214-9.

76 Muckerheide, A.; Apple R.J.; Pesce, A.J., Michael, J.G. Cationization of protein antigens. I. Alteration of immunogenic properties. J Immunol. 1987, 138(3), 833.

77 Tsuji, A.; Tamai, I. I. Carrier-mediated or specialized transport of drugs across theblood-brain barrier. Adv Drug Deliv Rev. 1999, 36 (3), 277-290.

78 Ohtsuki, S.; Terasaki, T. Contribution of carrier-mediated transport systems to the blood-brain barrier as a supporting and protecting interface for the brain; importance for CNS drug discovery and development. Pharm.Res. 2007, 24, 1745-1758.

79 Kannan, R.; Kuhlenkamp, J.F.; Jeandidier, E.; Trinh, H.; Ookhtens, M.; Kaplowitz, N. Evidence for carrier mediated transport of glutathione across the blood-brain barrier in the rat. J.Clin.Invest. 1990, 85, 2009-2013.

80 Garcia-Garcia, E.; Andrieux, K.; Gil, S.; Couvreur, P.; Colloidal carriers and blood-brain barrier (BBB) translocation: A way to deliver drugs to the brain. International Journal of Pharmaceutics. 2005, 298, 274-292.

81 Jeffrey, P.; Summerfield, S.G. Challenges for blood-brain barrier (BBB) screening. Xenobiotica. 2007, 37(10), 1135-51.

82 Begley, D. J. Efflux mechanisms in the central nervous system: a powerful influence on drug distribution within the brain. In Sharma, H. S.; Westman, J. Blood-spinal Cord and Brain Barriers in Health and Disease. 2004, 83–97.

83 Lamprecht, A.; Benoit, J.P.; Etoposide nanocarriers suppress glioma cell growth by intracellular drug delivery and simultaneous P-glycoprotein inhibiltion. 2006, 112, 208-213.

84 Estella-Hermoso de Mendoza, , A.E.; Préatb,V.; Mollinedoc, F.; M.J, Blanco-Prieto. In vitro and in vivo efficacy of edelfosine-loaded lipid nanoparticles against glioma. 2011, 156 ,421-426.

85 Guzman, C.A.; Feuerstein, G.; Role of nanobiotechnology in drug discovery. Pharmaceutical Biotechnology. Landes Press, Austin, Texas, 2009. or Adv Exp Med Biol 2009, 655, 37-43.

86 Pardridge, W.M. Recent advances in blood-brain barrier transport. Annu Rev Pharmacol Toxicol 1988, 28, 25–39.

87 Ghazani, A.A.; Lee, J.A.; Klostranec, J.; Xiang, Q.; Dacosta RS, Wilson BC, Tsao MS, Chan WC. High throughput quantification of protein expression of cancer antigens in tissue microarray using quantum dot nanocrystals. Nano Lett. 2006 Dec;6(12):2881-6.

88 Klostranec, J.M.; Xiang, Q.; Farcas, G.A.; Lee, J.A.; Rhee, A.; Lafferty, E.I.; Perrault, S.D.; Kain, K.C.; Chan, W.C..Convergence of quantum dot barcodes with microfluidics and signal processing for multiplexed high-throughput infectious disease diagnostics. Nano Lett. 2007, 7(9), 2812-2818.

89 Heath, J.R.; Davis, M.E. Nanotechnology and cancer. Annu Rev Med. 2008, 59, 251-65.

90 Hatakeyama, H.; Akita, H.; Ishida, E.; Hashimoto, K.; Kobayashi, H.; Aoki, T.; Yasuda, J., Obata, K.; Kikuchi, H.; Ishida, T., Kiwada, H.; Harashima, H. Tumor targeting of doxorubicin by anti-MT1-MMP antibody-modified PEG liposomes. Int J Pharm. 2007, 5, 342(1), 194-200.

91 Li, X.; Ding, L.; Xu, Y.; Wang, Y.; Ping, Q. Targeted delivery of doxorubicin using stealth liposomes modified with transferrin. Int J Pharm. 2009 , 21;373(1),116-123.

92 Wen, J.; Kim, B.Y.; Rutka, J.T.; Chan, W.C.W. Nanoparticle-mediated cellular response is size-dependent Nature Nanotechnology 2008, 3, 145 – 150.

93 Ying, X.;Wen, H.; Lu, W.L; Du, J.; Guo, J.; Tian, W.; Men, Y.; Zhang, Y.; Li, R.J.; Yang, T.Y.; Shang, D.W.; Lou, J.N. ; Zhang, L.R.; Zhang, Q. Dual-targeting daunorubicin liposomes improve the therapeutic efficacy of brain glioma in animals. 2010, 141, 183-192.

94 Pasha, S.; Gupta, K. Various drug delivery approaches to the central nervous system, Expert Opin.Drug Deliv. 2010, 7, 113-135.

95 Gaillard, P.J.; Visser, C.C.; De Boer, A.G. Targeted delivery across the blood-brain barrier. Exp Opin Drug Deliv. 2005, 2(2), 299-309.

96 Pardridge, W. M. Drug targeting, drug discovery, and brain drug development. In Brain drug targeting - The future of brain drug development. University Press, Cambridge 2001, 1-12.

97 Veiseh, O; Sun, C.; Fang, C. Specific Targeting of Brain Tumors with an Optical/Magnetic Resonance Imaging Nanoprobe across the Blood-Brain Barrier. Cancer Res. 2009, 69, 6200.

98 Gil, E.S.; Li, J.; Xiao, H.; Lowe, T.L. Quaternary ammonium beta-cyclodextrin nanoparticles for enhancing doxorubicin permeability across the in vitro blood-brain barrier. Biomacromolecules. 2009, 10(3), 505-516.

99 Tosi, G.; Vergoni, A.V.; Ruozi, B.; Bondioli, L.; Badiali, L.; Rivasi, F.; Costantino, L.; Forni, F.; Vandelli, M.A. Sialic acid and glycopeptides conjugated PLGA nanoparticles for central nervous system targeting: In vivo pharmacological evidence and biodistribution. J. Control Release 2010, 145, 49-57.

100 He, H.; Li, Y.; Jia, X.R.; Du, J.; Ying, X.; Lu, W.L.; Lou, J.N. ;Wei, Y. PEGylated Poly(amidoamine) dendrimer-based dual-targeting carrier for treating brain tumors. Biomaterials, 2011, 32, 2, 478-487.

101 Qian, Z. M.; Li, H.; Sun, H.; Ho, K. Targeted drug delivery via the transferrin receptor mediated endocytosis pathway. Pharmacol Rev. 2002, 54 (4), 561-587.

102 Kreuter, J.; Alyautdin, R.N.; Kharkevich, D.A.; Ivanov, A.A. Passage of peptides through the blood-brain barrier with colloidal polymer particles. Brain Research 1995, 674, 171-174.]

103 Kreuter, J. Nanoparticulate systems for brain delivery of drugs. Advances in Drug Delivery Reviews. 2001, 47, 65- 81.

104 Olivier, J. Drug transport to brain with targeted nanoparticles. NeuroRx. 2005, 2(1), 108–119.

105 Hatakeyama, H.; Akita, H.; Maruyama, K.; Suhara, T.; Harashima, H. Factors governing the in vivo tissue uptake of transferrin-coupled polyethylene glycol liposomes in vivo. Int J Pharm. 2004, 20,281(2), 25-33.

106 Pardridge, W.M.; Buciak, J.L.; Friden, P.M. Selective transport of anti-transferrin receptor antibody through the blood-brain barrier in vivo. J Pharmacol Exp Ther. 1991, 259, 66–70.

107 Gosk, S.; Vermehren, C.; Storm, G.; Moos, T. Targeting Anti–Transferrin Receptor Antibody (OX26) and OX26-Conjugated Liposomes to Brain Capillary Endothelial Cells Using In Situ Perfusion. Journal of Cerebral Blood Flow & Metabolism. 2004, 24, 1193–1204.

108 Grzelczak, M.; Pérez-Juste, J.; Mulvaney, P.; Liz-Marzán, L.M. Shape control in gold nanoparticle synthesis, Chem. Soc. Rev. 2008, 37, 1783–1791.

109 Jadzinsky, P.D.; Calero, G.; Ackerson, C.J.; Bushnell, D.A.; Kornberg, R.D. Structure of a thiol monolayer-protected gold nanoparticle at 1.1 Å resolution, Science. 2007, 318, 430–433.

110 Huang, X.H.; Neretina, S.; El-Sayed, M.A.; Gold nanorods: from synthesis and properties to biological and biomedical applications, Adv.Mater. 2009, 21, 4880–4910.

111 Daniel, M.C. Gold nanoparticles: assembly, supramolecular chemistry, quantum-size-related properties, and applications toward biology, catalysis, and nanotechnology, Chem. Rev. 2003, 104 293–346.

112 Nehl, C.L.; Hafner, J.H.; Shape-dependent plasmon resonances of gold nanoparticles, J. Mater. Chem. 2008, 18 , 2415–2419.

113 Jain, P.K.; Huang, X.; El-Sayed, I.H. ; El-Sayad, M.A. Review of some interesting surface plasmon resonance-enhanced properties of noble metal nanoparticles and their applications to biosystems, Plasmonics. 2007, 2, 107–118.

114 Bansal, V.; Basu, A.; Bhonde, R. R.; Sastry, M.; Shakula, R. Biocompatability of Gold Nanoparticles and their Endocytotic Fate Inside the Cellular Compartment: A Microscopic Overview. Langmuir 2005, 21, 10644-10654.

115 Han, G.; Ghosh, P.; Rotello, V. M. Functionalized Gold Nanoparticles for Drug Delivery. Nanomedicine 2007, 2, 113–123.

116 Hillyer J.F.; Albrecht R.M. Gastrointestinal persorption and tissue distribution of differently sized colloidal gold nanoparticles. J Pharm Sci. 2001, 90, 1927-1936.

117 Hillyer, J.F.; Albrecht, R.M. Correlative instrumental neutron activation analysis, light microscopy, transmission electron microscopy, and Xray microanalysis for qualitative and quantitative detection of colloidal gold spheres in biological specimens. Microsc Microanal.1999, 4, 481-490.

118 Hainfeld, J.F.; Slatkin, D.N.; Focella, T.M.; Smilowitz, H.M. Gold nanoparticles: a new X-ray contrast agent. Brit. J. Radiol. 2006, 79, 248–253.

119 De Jong, W.H.; Hagens, W.I.; Krystek, P.; Burger, M.C.; Sips, A. Geertsma, R. Particle size-dependent organ distribution of gold nanoparticles after intravenous administration. Biomaterials 2008, 29, 1912-1919.

120 Choi, H.S.; Liu, W.; Misra, P.; Tanaka, E.; Zimmer, J.P.; Ipe, B.; Bawendi, M.G.; Frangioni , J.V. Renal clearance of quantum dots. Nat Biotechnol. 2007, 25, 10, 1165-70.

121 Poduslo, J.F.; Curran, G.L. Polyamine modification increases the permeability of proteins at the blood–nerve and blood–brain barriers, Journal of Neurochemistry, 1996, 66, 1599–1609.

122 Hardebo, J.E.; Kahrstrom, J. Endothelial negative surface charge areas and blood-brain barrier function. Acta Physiol Scand. 1985, 125, 495- 499.

123 Fenart, L.; Casanova, A.; Dehouck, B.; Duhem, C.; Slupek, S.; Cecchelli, R.; Betbeder, D. J Pharmacol Evaluation of effect of charge and lipid coating on ability of 60-nm nanoparticles to cross an in vitro model of the blood-brain barrier. Exp Ther. 1999, 291, 3, 1017-22.

124 Podsiadlo, P.; Sinani, V.A.; Bahng, J. H.; Shi Kam, N.W.; Lee, J.; Kotov, N.A. Gold Nanoparticles Enhance the Anti-Leukemia Action of a 6-Mercaptopurine Chemotherapeutic Agent. Langmuir 2008, 24, 568-574.

125 Targeting Drug Delivery to the Brain via Transferrin Anchored Nanoparticles Nanomedicine and the Nervous System, Edited by Ross J . Hunter Science Publishers 2012, 250–263.

126 Nelson, J.A.; Cserr, H.F.; Shih, H.; Chu, S.H. Distribution of 6-Mercaptopurine Ribonucleoside and Other Purine Analogs to Brain. Cancer Research 1974, 34, 1889-1891.

127 Adamson, P.C.; Balis, F.M.; Arndt, C.A.; Holcenberg, J.S.; Narang, P.K.; Murphy, R.F.; Gillespie, A.J.; Poplack, D.G. Intrathecal 6-Mercaptopurine: Preclinical Pharmacology, Phase I/II Trial, and Pharmacokinetic Study, Cancer Research 1991, 51, 6079-6083.

128 Oldendorf, W.H. Blood-Brain Barrier Permeability to Drugs, Annual Review of Pharmacology. 1974, 14, 239-248.

CHAPTER 2

GOLD NANOPARTICLES DRASTICALLY DECREASE CLEARANCE AND INCREASE THE HALF-LIFE OF CHEMOTHERAPEUTIC AGENT, 6-MERCAPTOPURINE RIBONUCLEOSIDE

2.0   INTRODUCTION

Innovations in cell and molecular biology, high throughput techniques and combinatorial chemistry have resulted in an explosive growth in the number of new drug candidates in discovery pipelines. Despite these advances, the increasing molecular complexity of drugs and biological targets have not resulted in a corresponding increase in the number of new drug applications. Recent breakthroughs in nanotechnology have provided new opportunities to deliver new chemical entities (NCEs) to inaccessible drug targets.[1]

Polymeric nanoparticles (NPs)[2–4] and other nanoscale organic colloids, such as liposomes[5], micelles[6,7] and dendrimers[8,9] can increase the solubility of hydrophobic molecules, alter release and biodistribution of drugs, enable targeting and increase drug therapeutic indices.[10,11]

Much of the research, to date, has focused on organic nanoparticles. However similar to organic NPs, AuNPs can potentially benefit from the interactions of inorganic NPs with cells[12,13] and proteins.[14,15] While knowledge exists that the inorganic core of NPs can extensively change protein conformation,[16,17] these effects are still novel in the drug delivery field. These properties may affect many aspects of drug delivery, but it would be particularly interesting to see their

effect on the *in vivo* pharmacokinetics of drug-conjugated inorganic NPs, which until now has not been undertaken.

Considering the dramatic effects of inorganic NPs on enzyme activity,[18] AuNPs influence on pharmacokinetics could be equally dramatic. Gold nanoparticles (AuNPs) have attracted considerable attention as a promising drug delivery and diagnostic platform. This is because AuNPs are chemically stable, biocompatible, easy to functionalize for specific targeting, and have special plasmonic properties.[19-22] Work has also been done on better understanding the toxicity [23] and biodistribution of AuNPs.[24-26]

Antimetabolites, 6-MP and 6-MPR (Figures 2-1-1a and 2-1-1b) are widely used in the clinical treatment of acute lymphoblastic leukemia (ALL) and related diseases. The mechanism of action of purine antimetabolites essentially involves the conversion of mercaptopurine into cytotoxic 6-thioguanine nucleotide (6-TGN). 6-TGN is subsequently incorporated into the DNA or RNA of nucleated cells by hypoxanthine-guanine phosphoribosyl transferase (HGPRT) instead of the naturally occurring purine bases (Figure 2-1-2). [27] These events ultimately lead to cell death and are thought to be the source of the antineoplastic effects of mercaptopurines.

Conventional therapies with mercaptopurines are however susceptible to enzymatic inactivation by hepatic xanthine oxidase (XO), resulting in short plasma half-life and large variability in cytotoxic efficacy.[28] Inactivation involves methyltansferase catalysis of mercaptopurine to 6-methylmercaptopurine, and XO conversion to 6-thiouric acid.[29] The importance of optimizing 6-MP therapy to maintain high systemic exposure is therefore critical to effective clinical management of ALL.

In this paper we decided to gain a better understanding of the potential effects of gold NP on the pharmacokinetics of 6-MP and 6-MPR. Using 2D and 3D cell cultures, liver

homogenate, and animal studies, we demonstrate that AuNP carriers drastically alter the pharmacokinetics of 6-MPR by inhibiting hepatic xanthine oxidase (XO) activity, which has not been observed for other nanoscale carriers of this drug. [30,31] This study proposes a new and more effective paradigm for delivering 6-MPR using AuNPs (Figures 2-1-1c). To our knowledge, this is the first time such a delivery strategy to deliver 6-MPR has been proposed and evaluated.
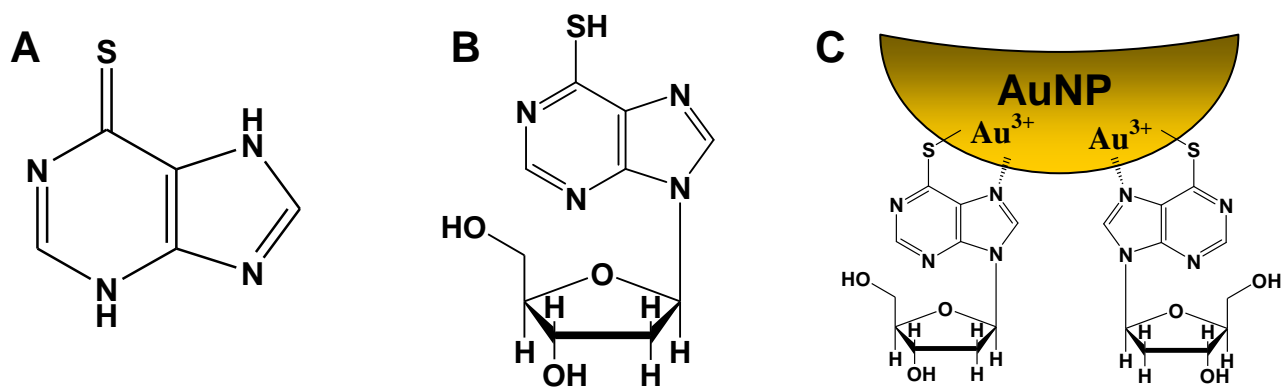
Figure 2-1-1. Chemical structure of (A) 6-Mercaptopurine (B) 6-Mercaptopurine riboside (C) Schematic representation of 6-MPR-Au NP
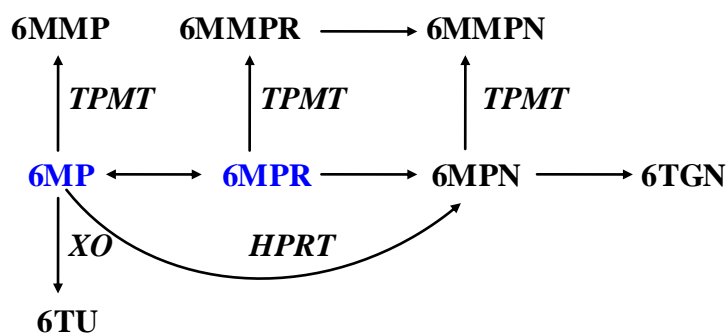
Figure 2-1-2. Schematic of the metabolism of 6-mercaptopurine (6MP) and 6-mercaptopurine riboside (6MPR). 6-mercaptopurine nucleotides (6MPN); 6-thioguanine nucleotides(6TGN); 6-methyl mercaptopurine (6MMP); 6-methylmercaptopurine riboside (6MMPR); 6-methylmercaptopurine nucleotides (6MMPN); 6-thiouric acid (6TU); thiopurine methyltransferase (TPMT); hypoxanthine phosphoribosyltransferase (HPRT); xanthine oxidase (XO).

2.1 METHODS

2.1.1 Materials

6-Mercaptopurine riboside, 6-Mercaptopurine, trisodium citrate dihydrate, tetrachloroauric (III) acid trihydrate, sodium borohydride, L-cysteine and fluorescein isothiocyanate isomer I (FITC) were purchased from Sigma-Aldrich and utilized without further purification. Ultrapure water (Barnstead) with 18.2 MΩ-cm was used for all experiments.

2.1.2 AuNPs synthesis

Citrate stabilized gold nanoparticles were freshly prepared and used immediately for the synthesis of 6-MPR-AuNPs. Gold sol was prepared by sodium borohydride reduction of tetrachloroauric (III) acid solutions following previously reported methods[32−34] with some modifications. Briefly, 5 mL of 1 w/w% tetrachloroauric (III) acid solution was diluted in 50 mL of ultrapure water and stirred for one minute. Next 2.5 mL of 3.4mM sodium citrate was added and the resulting solution was stirred for one minute. 5 mL of 0.075 wt% sodium borohydride was then added to the gold solution.

2.1.3 6-MPR-AuNPs synthesis

To prepare 6-MPR-AuNPs, 50 mL aqueous solution containing 12.5mg of 6-MPR was added to the reaction vessel containing gold sol, 30 secs after the sodium borohydride was added. Finally the solution containing 6-MPR-AuNPs was purified by centrifugation at 45000 rpm (190000 *gr max*) for 45 minutes. Following removal of the supernatant, the nanoparticles were

redispersed and the purification step repeated. The final precipitate was redispersed in 50 mL of sterile water for injection and stored at 4 °C until further use.

2.1.4 Nanoparticle Characterization

Transmission electron microscopy (FEI Tecnai, G2 Sphera) imaging was performed on 6-MPR-AuNP solutions at 100,000 times magnification. Mean surface area and diameter of the particles were then determined using Image-Pro Plus software (Media Cybernetics). To prepare samples for TEM, 2-5 µL aliquots of the sample were placed onto carbon-coated formvar covered support grids and air-dried overnight in a protective environment. Representative images from samples at 100,000x were used to acquire sufficient (greater than 100) nanoparticle objects for image analysis. Images were processed to optimize particle segmentation. Statistics and frequency histograms were generated. The zeta potential of 6-MPR-AuNP was measured using Zetasizer Nano ZS, Malvern Instruments. Finally, High Pressure Liquid Chromatography (Agilent HPLC System) was used to determine the concentration of 6-MPR immobilized on the surface of AuNPs by digesting the gold colloids with potassium cyanide.

2.1.5 Animal Studies

Male Sprague-Dawley rats weighing on average 250-300 grams with surgically implanted vascular cannulas in the carotid artery and jugular vein were purchased from Charles River Laboratories (Willmington, MA). Rats were housed, one per cage, in an American Animal Association Laboratory Animal Care accredited facility and maintained under standard conditions of temperature (22 ± 2 ºC), relative humidity (50%) and light and dark cycles (12 hours/12 hours). Rats were allowed to acclimate to their environment for one week. Rats had access to food and water *ad libitum* throughout the study. Experiments were conducted according

to procedures approved by the Pfizer Global Research and Development Animal Care and Use Committee and complied with the NIH Guide for the Care and Use of Laboratory Animals.

2.1.5.1 Pharmacokinetics Study

Three male SD rats were each dosed with 6-MPR-AuNPs (5 mg/kg active) over 3 minutes. As control, three male SD rats were each dosed with 5 mg/kg 6-MPR solution. All rats were dosed successfully via jugular vein cannulation (JVC) and no clinical observations were noted after treatment. At 0.083, 0.167, 0.25, 0.33, 0.5, 0.75, 1, 2, 3 and 4 hours post-dose, rats were anesthetized and 0.25 mL whole blood was drawn via carotid artery cannula (CAC) into heparinized tubes (with EDTA) followed by complete exsanguination. After each blood draw, rats were injected with 0.25 mL normal saline (0.9% sodium chloride, USP) to maintain a constant blood volume. Plasma was immediately separated by centrifugation at 13000*gr-max* for 5 minutes, and transferred to glass culture tubes. Samples were frozen at -20°C until analysis.

2.1.5.2 Sample Preparation

Standard curves and quality control samples (n=3 for each concentration) were prepared in control rat plasma. For plasma samples, a 50 µL aliquot of sample was precipitated with 200 µL of acetonitrile containing internal standard using a VWR Multi-Tube Vortexer (VWR, Bridgeport, NJ). For brain samples, 50 µL of blank plasma was added to 50 µL of homogenized (4-fold dilution in 60/40 Isoproponal/Water) sample. For brain standards and blanks, 50 µL of control rat brain homogenate was added to 50 µL of plasma. The resulting 100 µL of sample was precipitated with 300 µL of acetonitrile containing internal standard using a VWR Multi-Tube Vortexer. All samples were then centrifuged at 3000 rpm for 10 minutes with a standard

laboratory centrifuge (Eppendorf, Westbury, NY). The supernatant was collected in a clean 96-well collection plate and 5 µL was injected onto the HPLC for LC/MS/MS analysis.

2.1.5.3   6-MPR and 6-MP Bioanalysis

LC/MS/MS analysis was performed for 6-MPR and 6-MP using a high-performance liquid chromatography system with CTC PAL autosampler (Leap Technologies, Carrboro, NC) interfaced to an API 4000 LC/MS/MS quadrupole tandem mass spectrometer (Applied Biosystems/ MDS Sciex Inc., Ontario, Canada). 6-MPR, 6-MP and the internal standard (CP-628374) were separated on a Waters Atlantsi HILIC column (50 x 2.1 mm, 5µm) by isocratic elution.[35] Mobile phase A consisted of 95% Acetonitrile and 5% 200 mM ammonium formate in water, pH 3.0. Mobile phase B, which was used as a 0.5 minute wash step, consisted of 50% Acetonitrile, 45% HPLC Grade Water, and 5% 200 mM ammonium formate in water, pH 3.0. A flow rate of 650 µL/min was used.

The mass spectrometer was operated in negative ion ESI mode for the detection of 6-MPR and the Internal Standard (CP-628374). Multiple reaction monitoring was performed with the transitions m/z 283.2 $\rightarrow$ 151.1 for 6-MPR, m/z 685.3 $\rightarrow$ 366.1 for CP-628374 (internal standard). The mass spectrometer was operated in positive ESI mode for the detection of 6-MPR and the Internal Standard (CP-628374). Multiple reaction monitoring was performed with the transitions m/z 153.1 $\rightarrow$ 119 for 6-MP, m/z 687.3 $\rightarrow$ 319.7 for CP-628374 (internal standard). All raw data was processed using Analyst Software v.1.4.2 (Applied Biosystems/ MDS Sciex Inc., Ontario, Canada). The lower limits of quantification (LLOQ) for 6-MPR and 6-MP were 2.44 and 9.76 ng/mL, respectively. The upper limit of quantification (ULOQ) was 1250 ng/mL.

2.1.5.4 Pharmacokinetic Analysis

Mean concentrations of 6-MPR and 6-MP were used in the analysis. Paired student's t-test was used to determine statistical significance and was assessed at the 5% level ($p < 0.05$). Pharmacokinetic analysis was performed using standard noncompartmental methods as implemented in Watson Kinetica™ Version 5.0 Software (Thermo Scientific, Waltham, MA). Linear-up/log-down method of estimation was used to calculate area under the concentration-time curve (AUC). Total body clearance (CL) was calculated as dose divided by AUC and adjusted for body surface area .The steady state volume of distribution (V_{dss}) was calculated as the ratio of CL to the slope of the terminal log-linear phase – the elimination rate constant (k_e). The terminal half-life (t½) was calculated as ln2 divided by k_e. Initial concentration (C_o) and percentage of AUC extrapolated ($AUC\%_{extra}$) are obtained by extrapolating the first and last concentrations, respectively.

2.1.6 In Vitro Experiment – 6-MPR metabolism in rat liver homogenate

2.1.6.1 Liver homogenate preparation

Liver homogenates were prepared using livers obtained from male Sprague-Dawley rats (200-250 grams). The livers obtained were either used fresh or stored at -70°C until use. The liver was perfused with saline, removed and rinsed in phosphate buffer (pH 7.4). Liver, weighing roughly 10 grams, was homogenized in 5mL of 0.01M Tris-HCL buffer (pH 8.0), containing 1mM EDTA for 5 minutes in a potter glass homogenizer equipped with a Teflon pestle. The homogenate was rapidly heated to 55°C for 5 minutes and then cooled quickly to below 10°C in an ice bath. The animals used in this study were those that were sacrificed as part of other

experiments approved by the Pfizer Global Research and Development Animal Care and Use Committee and complied with the NIH Guide for the Care and Use of Laboratory Animals.

2.1.6.2 Incubation of liver homogenate with 6-MPR-AuNPs

200 μL of 6-MPR (with and without AuNPs), 6-MPR-AuNPs (with and without AuNPs), and 6-MPR-AuNPs plus 6-MPR were each incubated in 3mL of liver homogenate at 37°C with continuous shaking (60 RPM). 6-MPR was also added to the liver homogenate in the presence of 5mM allopurinol (xanthine oxidase inhibitor). To ensure that 6-MPR did not decompose in the assay buffer (Tris-HCL containing EDTA), a solution of 6-MPR in the buffer was tested under conditions similar to homogenate assay. As a control, a portion of rat liver homogenate was pre-treated with citrate-stabilized AuNPs for 24 hours prior to incubation with 6-MPR. The concentration of 6-MPR or AuNPs in the test formulations was maintained at 0.9mM.

100 μL aliquots were collected at 5, 30, 60, 120 and 180 minutes after incubation, and each aliquot was added to 75 μL of ice-cold 50% (w/v) trichloroacetic acid to quench any reaction. The mixture was centrifuged for 10 min at 1500*g* and filtered through Acrodisc LC13 0.2 μm filters (Gelman Sciences). The resulting samples were kept at 0 - 4°C until analyzed. Samples collected were assayed for 6-MPR and 6-MP by LC-MS/MS as described below.

2.1.7 In Vitro Experiment – 6-MPR metabolism in HepG2 cell culture

2.1.7.1 Inverted colloidal crystal hydrogel scaffold preparation

Inverted colloidal crystal (ICC) hydrogel scaffolds were prepared following a previously described method.[36] Briefly, cylindrical shape colloidal crystal templates (diameter 6 mm, height 1 mm) were constructed with size-controlled glass beads (diameter 173 ±17μm).

Acrylamide hydrogel precursor solution composed of 30% w/w acrylamide, 5% w/w N,N-methylenebisacrylamide and 0.1% v/v N,N,N,N tetramethylethylenediamine in nitrogen purged deionized water was infiltrated into colloidal crystals via centrifugation and radically polymerized upon addition of 1% w/w potassium peroxide solution. Once polymerization was completed, the hydrogel matrix exterior of the colloidal crystals was trimmed down and the glass beads were dissolved in 5% w/w hydrogen fluoride solution. The leftover 3-D hydrogel matrix retained an inverted structure of colloidal crystal template. ICC hydrogel scaffolds were subsequently washed with acidic solution (pH 2), deionized water and phosphate-buffered saline solution. Finally, ICC hydrogel scaffolds were freeze-dried and preserved in a -70℃ freezer until used.

2.1.7.2 HepG2 spheroid cell culture

Rehydrated ICC hydrogel scaffolds were sterilized in 70% ethanol for 15min under UV light and subsequently washed with PBS solution three times. HepG2 (HB-8065, ATCC) human hepatocarcinoma cells were expanded with William's E Medium supplemented with 10% fetal bovine serum and 1% penicillin-streptomycin in a 37℃ incubator with 5% carbon dioxide. The cells were harvested from flasks using 2.5% Trypsin-ethylenediaminetetraacetic aicd (EDTA) solution, once 70-80% confluence was reached. Final cell concentration was adjusted to 25×10^6 cells/ml. 20µl of cell suspension, containing approximately 0.5×10^6 cells was dropped on top of a slightly dehydrated ICC hydrogel scaffold. After 20-30 min, the cell-loaded scaffolds were transferred to a 48-well plate containing 1.5ml of culture medium. HepG2 cells formed homogenous spherical clusters within the scaffold after 5 days. [37,38]

2.1.7.3 Microscope imaging

Morphology of colloidal crystals, ICC hydrogel scaffolds and HepG2 spheroids were characterized under scanning electron microscope (FEI Nova Nanolab). Cell spheroids were fixed with 2.5% glutaldehyde and then serially dehydrated with 50, 70, 90, 95 and 100% ethanol solutions. Before imaging, completely dried samples were coated with Au (Desktop2, Venton Vacuume Inc.). Diffusion of a cell tracker dye molecule between 2-D flat and 3-D spheroid culture was characterized under laser scanning confocal microscope (Leica SP2). HepG2 cells in both 2-D and 3-D cultures were incubated in 5µM carboxyfluorescein diacetate succinmidyl ester (CFDA-SE, Invitrogen) solution for 20min and subsequently washed three times with PBS solution. Fluorescent signal was detected using 490-550nm emission bands with a 457nm excitation laser.

2.1.7.4 Treatment of HepG2 spheroid culture with 6-MPR-AuNPs

Homogenous hepatic spheroids formed within ICC scaffolds placed in 48-well and 24-well plates were used as a 3-D and 2-D culture formats, respectively. In order to directly compare drug effects, total cell mass and culture volume were maintained as 0.5×10^6 cells and 1.5mL, respectively. Half the volume of media was changed daily for 5 days. On day 6, 2-D and 3-D culture media were each replaced with 1.5mL of 0.25mg/mL 6-MPR, 0.25mg/mL 6-MPR conjugated AuNPs, or 1:1 v/v of 0.25mg/mL 6-MPR and 0.25mg/mL allopurinol. The 6-MPR and 6-MPR-AuNPs used in these experiments were identical to those used in the animal studies. 200µl of supernatant was collected at 15, 30, 45, 60, 90, 120 and 240 minutes after incubation for analysis. Triplicate samples were pulled per time-point. Collected samples were stored at -70°C freezer until analyzed. After sample collection, the cultures were exposed to a Trypsin-

EDTA solution to detach cells either for 2-D culture or 3-D aggregation. Total DNA contents in 3-D and 2-D culture were measured using PicoGreen dsDNA quantification kit (Invitrogen), which was used to normalize the results. Cell-scaffolds were mechanically destroyed using forceps and sonicated to make a cell lysate solution. Supernatant was collected from the three test groups for analysis.

We calculated the area under the curve (AUC) of 6-MPR concentration-time curve to determine the effect of AuNPs on 6-MPR in the HepG2 cell culture. Statistical analyses were done by using SPSS for Windows (version 16.0; SPSS, Inc., Chicago, Illinois, USA). A *P*-value <0.05 was considered statistically significant.

2.1.8 Sample Preparation

Standard curves were prepared in control cell culture media. 50 μL aliquot of sample was precipitated with 200 μL of acetonitrile containing internal standard using a VWR Multi-Tube Vortexer (VWR, Bridgeport, NJ). All samples were then centrifuged at 3000 rpm for 10 minutes with a standard laboratory centrifuge (Eppendorf, Westbury, NY). The supernatant was collected in a clean 96-well collection plate and 5 μL was injected onto the HPLC for LC/MS/MS analysis.

2.1.9 6-MPR and 6-MP Analysis

LC/MS/MS analysis was performed for 6-MPR and 6-MP using a HPLC system with CTC PAL autosampler (Leap Technologies, Carrboro, NC) interfaced to an API 4000 LC/MS/MS quadrupole tandem mass spectrometer (Applied Biosystems/MDS Sciex Inc., Ontario, Canada). 6-MPR, 6-MP and the internal standard (CP-628374) were separated on a Waters Atlantsi HILIC column (50 x 2.1 mm, 5μm) by isocratic elution. The reader is advised to

refer to previous sections on the bioanalysis of brain, CSF and plasma samples for the detailed

analytical method used to analyze 6-MPR and 6-MP samples. All data were processed using

Analyst Software v.1.4.2 (Applied Biosystems/ MDS Sciex Inc., Ontario, Canada). The lower

limits of quantification (LLOQ) for 6-MPR and 6-MP were 2.44 and 9.76 ng/mL, respectively.

The upper limit of quantification (ULOQ) was 425ug/mL.

2.2   RESULTS AND DISCUSSION

2.2.1   Gold Nanoparticles

Drug-loaded AuNPs were synthesized taking advantage of the ability of 6-MPR to bind to gold via the thiol end of the molecule. Reduction of Au(3+) by borohydride in the presence of 6-MPR (see Method) yielded 5.12 nm ± 0.3 (Figures 2-2-3a and 2-2-3b). The electrokinetic potential (ξ) and surface area of 6-MPR-AuNPs were +7.2 mV and 30.59μm^2 respectively. The concentration of bound 6-MPR in the resulting NP dispersion was 0.25 mg/mL. Similarly, the concentration of 6-MPR and allopurinol solutions used in the experiments was each 0.25mg/mL.
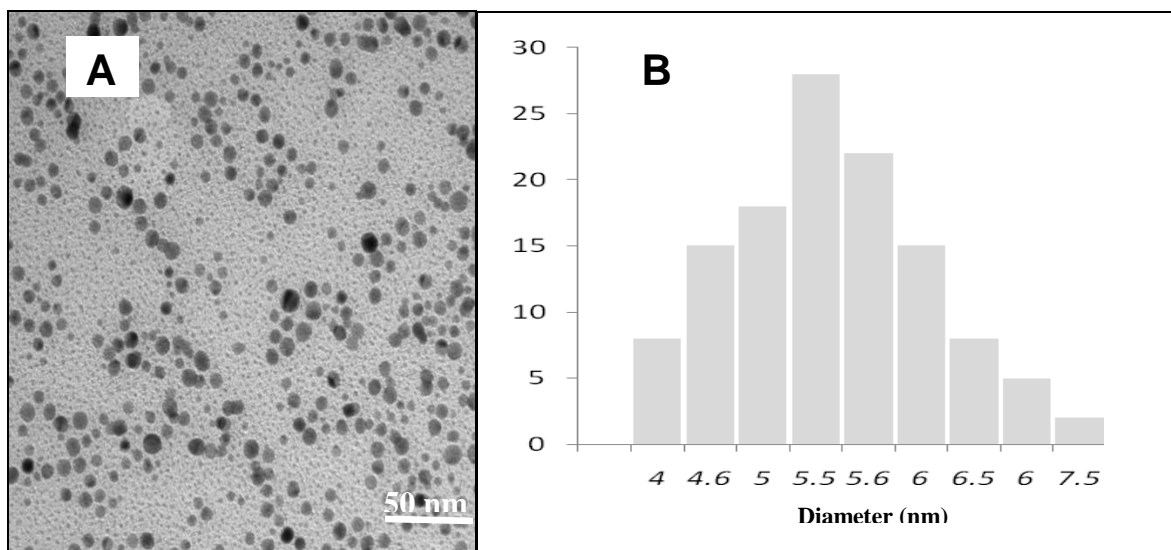
Figure 2-2-3. Gold nanoparticle characterization: (A) Transmission electron micrograph of 6-MPR-AuNPs with mean size of ca.5.12 nm ± 0.30 (mean ± S.D.). (B) 6-MPR-AuNPs particle size histogram.

2.2.2 Pharmacokinetics

Male Sprague-Dawley (SD) rats received 5 mg/kg intravenous injections of 6-MPR-AuNPs and 6-MPR solution, as control. The resulting mean plasma concentration-time profiles are shown in Figure 2-2-4, and the pharmacokinetic parameters are provided in Table 2-1. As expected, markedly different pharmacokinetic profiles were observed for the two groups. The rats treated with the control formulation experienced a precipitous drop in systemic 6-MPR and 6-MP levels compared to the rats treated with 6-MPR-AuNPs.

The 6-MP plasma concentration for rats administered 6-MPR alone was well below the 9.76 ng/mL lower limit of quantification. The initial drug concentration (C_0) and area under the curve (AUC) of 6-MPR for rats treated with 6-MPR-AuNPs were 11,440±3860 and 3,695 ±315 ng/mL·h, respectively. This is compared to 50.75±1.45 and 12.45±1.25 ng/mL·h for rats given 6-MPR alone. This represents a 297-fold increase in 6-MPR exposure compared to rats treated with 6-MPR. Correspondingly, the nanoparticles increased the half-life of 6-MPR from 13.8±5.94 to 44.16±1.98 minutes.

The steady-state volume of distribution (V_{dss}) of 6-MPR decreased from 25.55±13.05 L/kg (control group) to 0.554±0.10 L/kg for rats dosed with 6-MPR-AuNPs. This decrease in volume of distribution could be due to the localization of nanoparticles in the systemic circulation and reduced tissue binding, compared to the unconjugated 6-MPR.

The intrinsic clearance of 6-MPR and 6-MP were also significantly lower after receiving 6-MPR-AuNPs, averaging 22.45±1.95 and 68.7±3.01 mL/min/kg, respectively. The clearance of the control group was 6,190±810 mL/min/kg. Since the glomerular filtration rate alone cannot totally account for the observed clearance and no active carrier-mediated secretory process has been suggested in the urinary excretion of thiopurines,[39-41] extensive extrarenal clearance can be

inferred. Rather, these results are consistent with the dramatic decrease of total clearance (276-fold), which has a more profound effect on half-life than volume of distribution. That is because the volume of distribution is dependent on free plasma drug, whereas both free and bound drug are available for clearance. The high clearance observed in this study for free drug is consistent with widely-reported hepatic metabolism of 6-MPR *in vivo*.[42]

We hypothesize that conjugation of 6-MPR to AuNPs may have inhibited the metabolic inactivation of 6-MPR by XO. Alternatively, one may suggest that 6-MPR-AuNPs could avoid metabolism of 6-MPR by preventing diffusion of 6-MPR into intracellular spaces of liver cells where XO-catalyzed metabolism occurs. In order to test these hypotheses, we carried out metabolic studies using different *in-vitro* models such as rat liver homogenate, spheroid 3D cell culture of hepatocytes in specially designed scaffolds, and 2D liver cell cultures. Systematic study of 6-MPR in the free and NP-conjugated form, at various levels of cellular complexity allowed us to comprehensively test these hypotheses.
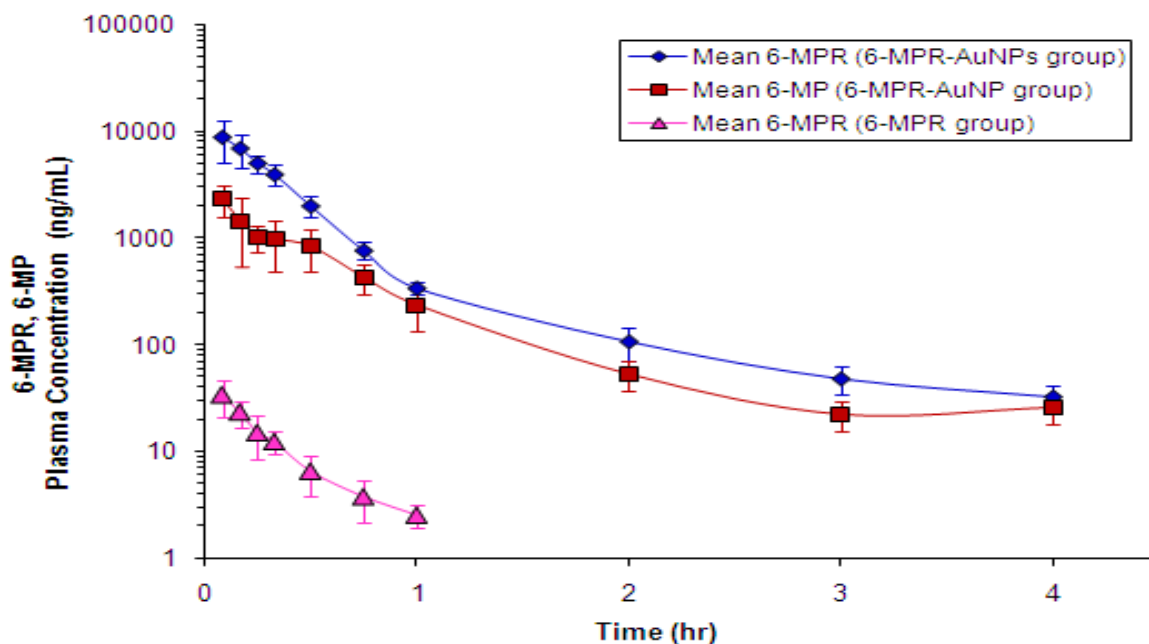
Figure 2-2-4. Mean concentration-time profiles of 6-MPR and 6-MP in Sprague Dawley rats following intravenous administration (5 mg/kg 6-MPR) of 5 nm 6-MPR-AuNPs or unconjugated 6-MPR. Each point and bar represents the mean ± S.D. (n = 3).

Table 2-1. Pharmacokinetic parameters of 6-MPR and 6-MP in Sprague Dawley rats after intravenous administration (5 mg/kg 6-MPR) of 5nm 6-MPR-AuNPs or unconjugated 6-MPR. Data represents the mean ± S.D. (n = 3).

Parameters		6-MPR-AuNP group Mean ±SD (n=3)	6-MPR group Mean ±SD (n=3)
AUC (ng/mL•h)	6-MPR	3695 ± 315	12.45 ± 1.25
	6-MP	1195 ± 55	BLQ*
% AUC Extrap (%)	6-MPR	0.937 ± 0.184	8.68 ± 2.82
	6-MP	2.05 ± 0.1	BLQ
Co (ng/mL)	6-MPR	11440 ± 3860	50.75 ± 1.45
	6-MP	4410 ± 2170	BLQ*
$t_{1/2}$ (hours)	6-MPR	0.736 ± 0.033	0.23 ± 0.10
	6-MP	0.466 ± 0.091	BLQ*
CL (mL/min/kg)	6-MPR	22.45 ± 1.95	6190 ± 810
	6-MP	68.70 ± 3.10	BLQ*
V_{dss} (mL/kg)	6-MPR	554 ± 102	25550 ± 13050
	6-MP	2035 ± 75	BLQ*

*Value below 9.76ng/mL

2.2.3 Metabolism of 6-MPR-AuNPs in rat liver homogenate

Free 6-MPR, 6-MPR-AuNPs and other combinations of NPs and 6-MPR were incubated in rat liver homogenate. Samples were collected for up to 180 min after incubation and analyzed for 6-MPR. Statistical significance (p-value <0.01) was achieved. The results showed that the concentration of 6-MPR declined precipitously within the initial 5 minutes of incubation, and fell below analytical detection limits within 120 minutes of incubation (Figure 2-2-5). On the contrary, 6-MPR-AuNPs increased the amount of 6-MPR by about 30-fold in the first 60 minutes. We added citrate-stabilized AuNPs to the homogenate containing 6-MPR-AuNPs and found no change in 6-MPR concentration. Moreover, when 6-MPR was added to samples pre-incubated with 6-MPR-AuNPs, we observed an almost exact increase in the amount of 6-MPR as was added to homogenate. Interestingly, when 6-MPR was not conjugated to NPs and instead admixed with free 6-MPR, a fair amount of inhibitory effect was still observed. This could be because some of the 6-MPR gets adsorbed to the surface of the NPs effectively forming 6-MPR-AuNPs.

To confirm the effect of XO and the effects of NPs on XO, we investigated the metabolism of 6-MPR in the homogenate after incubation with allopurinol (a XO inhibitor). The result shows that the effect of 6-MPR-AuNPs is comparable to that of allopurinol. Moreover, when rat liver homogenate was pre-treated with stabilized AuNPs for 24 hours prior to incubation with 6-MPR, metabolism of 6-MPR occurred as previously noted. This eliminates the possibility for XO poisoning or deactivation by the AuNPs. Similarly, albeit to a lesser extent, we observe rapid decline in 6-MPR after incubation with mixture of 6-MPR and AuNP, further confirming that AuNPs do not poison XO. Chemical decomposition of 6-MPR in buffer

was also evaluated and the drug was found to be stable. These results, including the fact that adding excess 6-MPR or AuNPs did not change the 6-MPR in liver homogenate, confirm that 6-MPR-AuNPs directly inhibit XO and thereby prolong the half-life of 6-MPR.

By AuNPs inhibiting the oxidation of 6-MPR to 6TU, 6-MPR can be converted to the active metabolite 6-thioguanine (6TGN). The presence of 6TGN as was confirmed in rat plasma samples provides further evidence that AuNPs play an important role in preventing the metabolism 6-MPR. This also confirms that the biological properties of 6-MPR is conserved after conjugation to AuNPs and after subsequent interaction with XO. Podsiadlo and Kotov previously demonstrated that AuNPs do not diminish 6-MPR activity, instead they enhance the antitumor properties of 6-MPR.[32] Based on the results here, we propose that the AuNPs does in fact prevent metabolic degradation of 6-MPR from occurring by inhibiting XO, while still allowing the phosphorylation necessary for the cytotoxic effects of 6-MPR to take place at the riboside end.
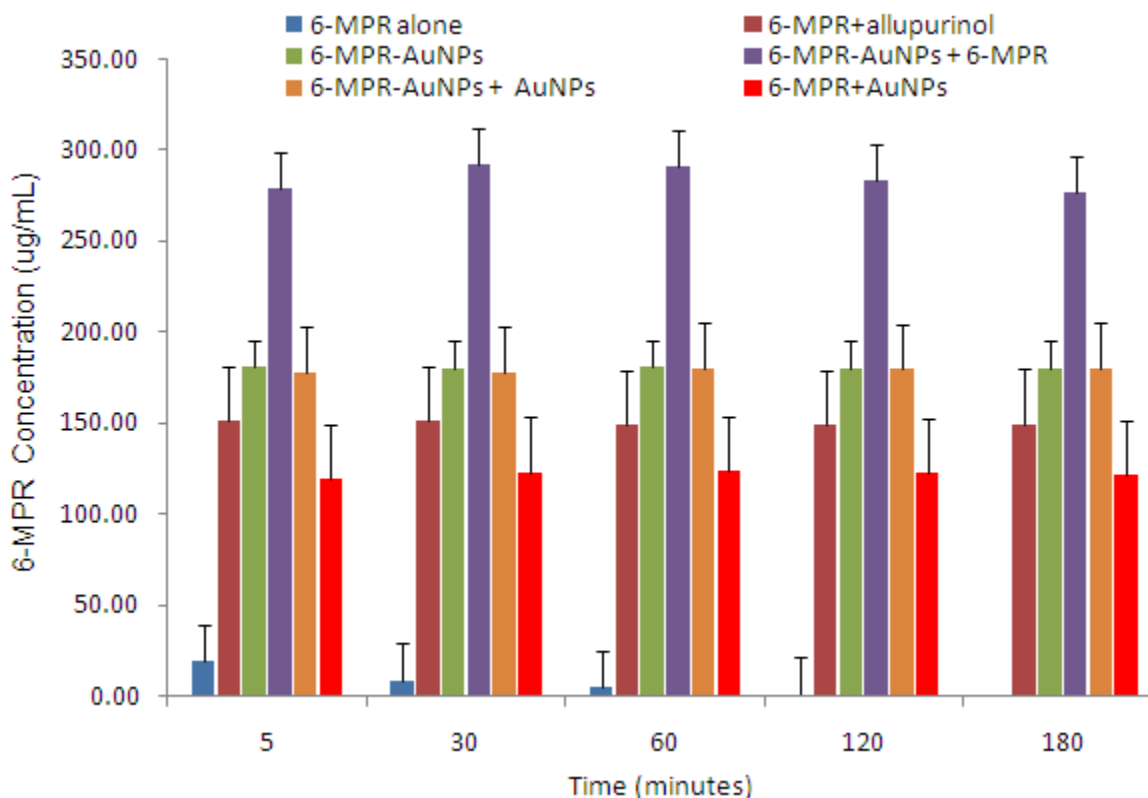
Figure 2-2-5. Metabolic stability of 6-MPR in rat liver homogenate monitored post-incubation. 6-MPR concentration (Mean ± S.D; n=6) of six test groups at different time points, after incubation in liver homogenates obtained from male Sprague-Dawley rats.

2.2.4   Characterization of HepG2 spheroid culture

Standardized and functional *in vitro* tissue culture model is important for achieving faithful and reproducible drug testing results.[43] The pore size distribution of ICC hydrogel scaffolds (D=173 ±17µm) made with a cell-repulsive synthetic hydrogel matrix effectively induces multicellular aggregate formation of HepG2 cells having narrow size distribution (D=99.9 ±14µm). This is important for controlled and reproducible testing results (Figure 2-2-6.). Established 3-D hepatic spheroid culture replicates tissue-like morphology and functions, as well as physiological processes such as diffusional delivery of nutrients and oxygen.

In order to characterize delivery of drug or small molecules, we expose 2-D flat and 3-D spheroid culture to a cell tracker dye molecule and then used confocal microscopy to determine their distribution. As shown in Figure 2-2-7, morphological differences between 2-D flat and 3-D spheroid culture result in significantly different staining profiles. For example, in 2-D culture, all cells are homogenously stained. On the other hand, in 3-D culture, only cells located on the surface are fully stained and the inner cells are exposed to less dye molecules due to diffusion via cellular layer. This feature closely resembles molecular delivery in tissue cells. It is highly conceivable that the drug molecules or nanoparticles undergo similar transport processes in the body. Such diffusion limitation in 3-D spheroid culture is one of the reasons for reduced drug effect compared to 2-D culture.

Figure 2-2-6. SEM images of ICC hydrogel scaffolds and 3D hepatic spheroid culture models. (A) Colloidal crystal templates prepared with 180-220 μm microspheres (Left) and inverted structure made of polyacrylamide hydrogel matrix (Right). The structure of a tightly packed narrow size distribution of microspheres was transferred to 3D homogenous spherical pore arrays. (B) HepG2 spheroid formation after 5 days of culture (Left) and HepG2 spheroid under high magnification (Right). Cell repulsive nature of polyacrylamide hydrogel matrix rapidly induces cellular aggregation.

Figure 2-2-7. Comparison of cell tracker dye molecule diffusion between 2-D and 3-D HepG2 cell cultures under confocal microscope. Left panel is a fluorescent image and right panel is a fluorescent-transmission overlay image. (A) In conventional 2D flat culture, entire cells were homogenously stained with a dye molecule. (B) In 3D spheroid culture, only exterior regional cells were stained with a dye molecule due to the diffusion limit.

2.2.5 Metabolism of 6-MPR-AuNPs in HepG2 spheroid assay

Using standardized liver spheroid culture model we studied the potential effect of AuNPs on the metabolism of 6-MPR by liver XO. We measured the concentration of 6-MPR and 6-MP in the 2-D and 3-D HepG2 cell culture media over the course of 4 hours after incubation with 6-MPR, a mixture of allopurinol and 6-MPR, and AuNP-6-MPR. The results show that in the presence of gold nanoparticles, metabolism of 6-MPR and 6-MP was significantly reduced (Figure 2-2-8 and Table 2-2). The 6-MP and 6-MPR concentrations in the cell cultures were respectively 3 and 4-fold lower than reference, when cells were exposed to free drug alone. However, when cells were incubated with 6-MPR-AuNPS, the concentrations of 6-MP and 6-MPR remained unchanged. Similarly, cell cultures incubated with a mixture of 6-MPR and

allopurinol showed little or no change in the initial concentrations of 6-MPR and 6-MP. In this case the 6-MPR-AuNPs performed comparably to the mixture of 6-MPR and allopurinol.

When cells were treated with AuNPs, the 6-MPR concentration was comparable to cells treated with a mixture of 6-MPR and allopurinol. These results are consistent with previous in vivo observations. However, analysis of cell lysate revealed that 2D cells treated with 6-MPR-AuNPs contained the same amount of 6-MPR as cells incubated with free 6-MPR (Table 2-3). Interestingly, 3D cell lysate for the 6-MPR-AuNPs group had lower amounts of 6-MPR compared to other treatment groups. One possible explanation for this is that the extraction of 6-MPR-AuNPs from the cell-scaffolds matrix was incomplete, rendering the lysate assay sub-potent. This is the so-called matrix effect and presents distinct challenges to molecular analysis of biological matrices.[44-46]

Though the effect of AuNPs on 6-MPR was similar in 2D and 3D liver culture models, the normalized AUCs of 6-MP and 6-MPR in 3D culture were significantly lower than in 2D culture (roughly two orders of magnitude). This reflects the large number of cells present in the 3D scaffold (701,158 ±57991 per scaffold), compared to the same culture volume of 2D well plate (10,832 ±1745 cells per well). Further unlike 2D cell culture models, 3D hepatic cells produced concentration profiles with elimination processes that are characteristic of *in vivo* models. In the 3D culture, 6-MP and 6-MPR concentrations seem to decline exponentially with time.

Though in some cases they can provide useful information, *in vitro* 2D cell cultures often do not accurately predict complex physiological processes such as would be encountered in drug metabolism. Cellular processes are strongly dependent on 3D organization and limit the ability of 2D cell models to reproduce *in vivo* responses.[47] 3D culture restores tissue-like morphology and phenotypes that, in turn, significantly improve prediction of drug response compared to

conventional 2D flat culture. The use of liver spheroid culture model to evaluate hepatic

clearance of drugs has significant implications on the development of drugs.

Several human liver *in vitro* assays have been developed in the past few decades. These,

include supersomes, microsomes, cytosol, S9 fraction, cell lines, transgenic cell lines, primary

hepatocytes, liver slices, and perfused liver. However, *in vitro* cell culture models have been

primarily based on two-dimensional (2-D) monolayer of cells, which despite providing valuable

information do not accurately predict tissue morphology and functions. This may be because key

physiological processes are absent from cell assays.

These limitations have prompted the development of three-dimensional (3-D) cell culture

models. Compared to the 2-D culture of cell monolayers, 3-D models can provide a cellular

microenvironment that more closely mimics the conditions observed in native tissues. [48,49]

This is critical for drug testing since environmental cues can have profound effects on the

properties, behaviors, and functions of cells. These, in turn, affect cellular responses to drugs.

Factors such as matrix composition, cell type, cell health, cell seeding densities, and time of

culture can influence the success of 3-D cultures.
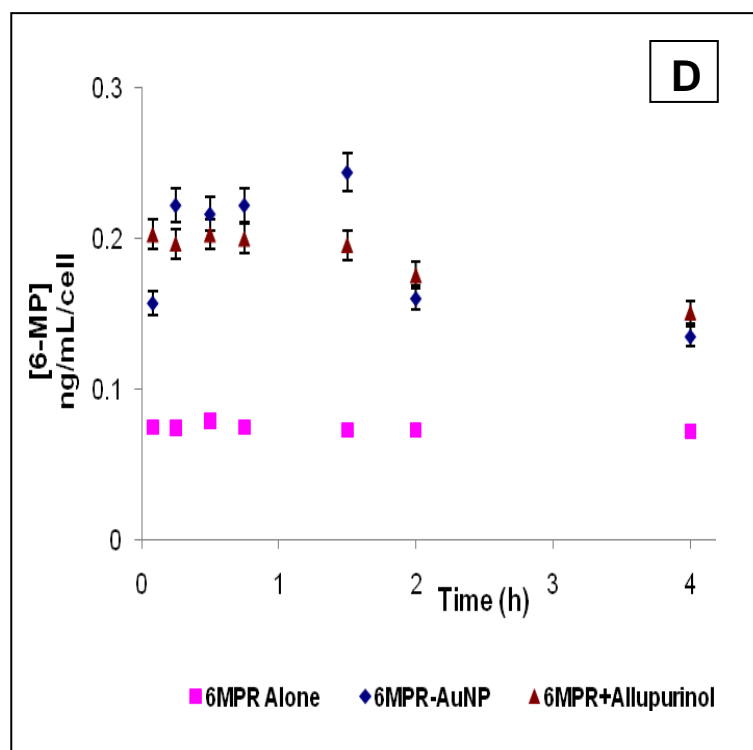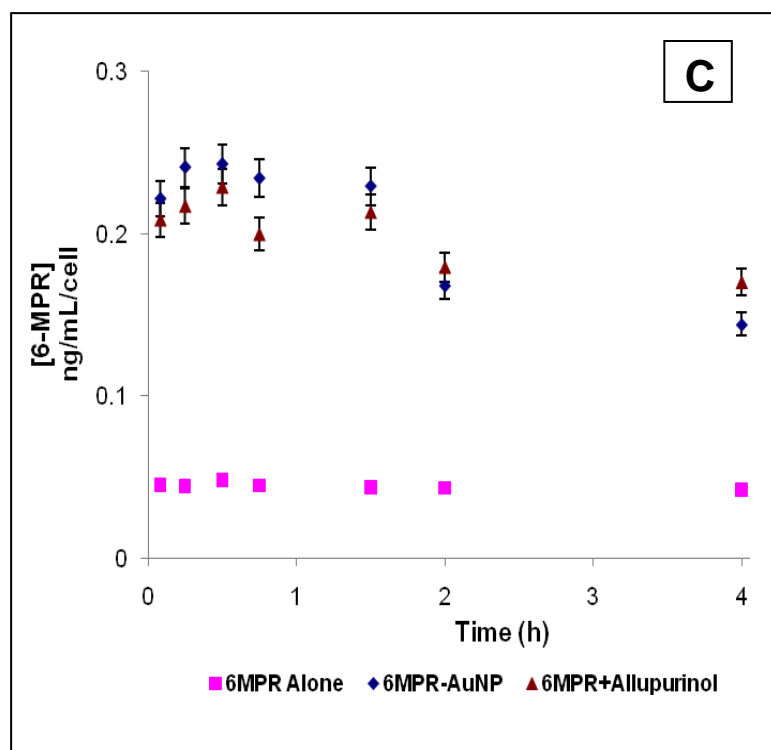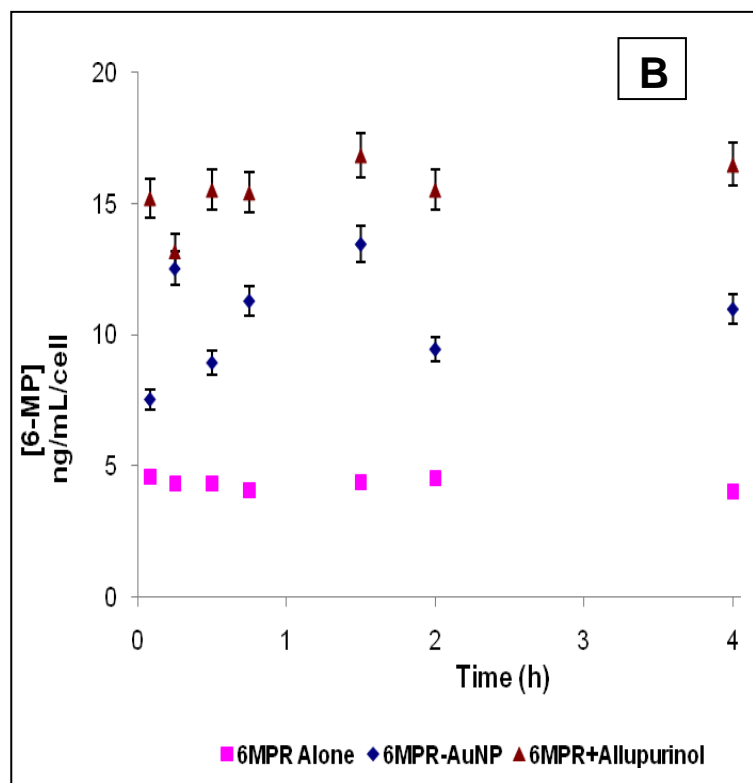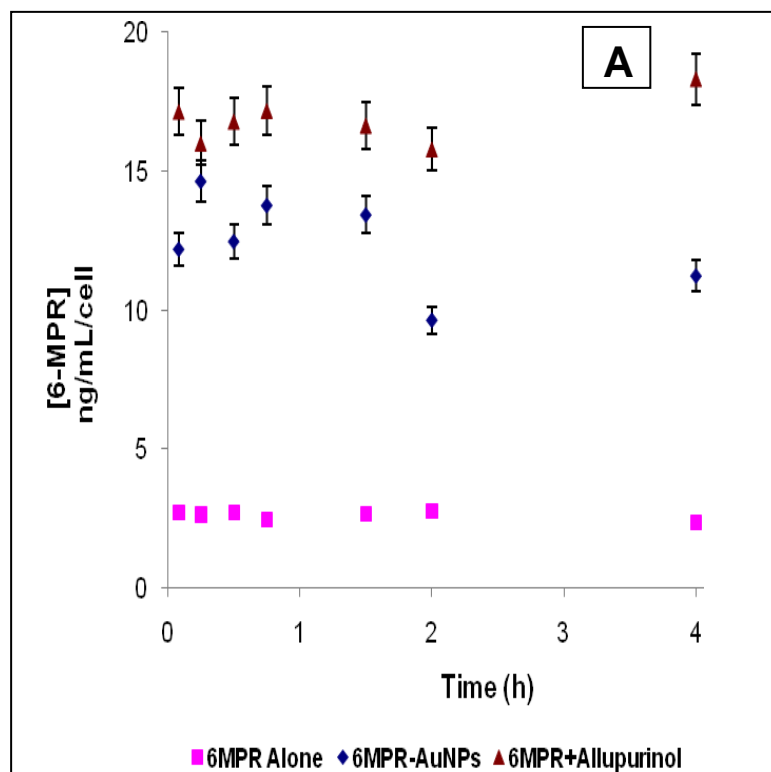
Figure 2-2-8. Normalized drug concentration-time profiles of three formulations of 6-MPR in 2-D and 3-D HepG2 spheroid culture. (A) 6-MPR in 2-D culture, (B) 6-MP in 2-D culture, (C) 6-MPR in 3-D culture, (D) 6-MP in 3-D culture. Mean ± S.D. (n = 6).

Table 2-2. Normalized area under concentration-time curve of 6-MPR and 6-MP in 2D and 3D HepG2 culture

Formulation	6-MPR (ng/mL/cell•h) Mean ±SD (n=6)		6-MP (ng/mL/cell•h) Mean ±SD (n=6)	
	2-D culture	3-D culture	2D culture	3D culture
6-MPR	10.132 ±0.9	0.172 ±0.06	16.837 ±1.1	0.286 ±0.1
6-MPR+ allopurinol	66.012 ±2.1	0.747 ±0.1	61.959 ±1.5	0.700 ±0.2
6-MPR-AuNP	45.716 ±1.4	0.744 ±0.3	42.316 ±1.3	0.712 ±0.3

Table 2-3: Normalized mean concentrations of 6-MPR and 6-MP in 2D and 3D HepG2 culture lysate

Formulation	6-MPR (ng/mL/cell) Mean ±SD (n=6)		6-MP (ng/mL/cell) Mean ±SD (n=6)	
	2-D culture	3-D culture	2-D culture	3-D culture
6-MPR	0.071 ±0.03	0.045 ±0.01	0.087 ±0.02	0.046 ±0.02
6-MPR + allopurinol	0.075 ±0.09	0.015 ±0.01	0.078 ±0.03	0.016 ±0.01
6-MPR-AuNP	0.072 ±0.06	0.001 ±0.02	0.080 ±0.02	0.002 ±0.002

2.3   CONCLUSIONS

The BBB penetration of drug molecules alone does not guarantee optimum brain delivery. Therefore optimizing drug pharmacokinetics is critical to the development of drug therapies and particularly CNS therapies. Here, we used in vitro and in vivo pharmacokinetics studies to demonstrate that AuNP carriers can dramatically increase the plasma half-life of 6-MPR, by directly inhibiting liver xanthine oxidase (XO) activity. To our knowledge, this phenomenon has not been previously observed for other nanoscale carriers of 6-MPR.

These results have several important clinical implications. 6-mercaptopurine is a well established antineoplastic agent. Optimizing 6-MPR therapy to maintain high systemic exposure is critical to effective clinical management of inflammatory diseases and malignancies, including potentially brain tumors. In addition, lower dose requirements and increase drug therapeutic index will result.

REFERENCES

1   Vasir, J.; Reddy, M.; Labhasetwar, V. Nanosystems in Drug Targeting: Opportunities and Challenges Current Nanoscience 2005, 1, 47-64.
2   Rafferty, D.E.; Elfaki, M.G.; Montgomery, P.C. Preparation and characterization of a biodegradable microparticle antigen/cytokine delivery system. Vaccine 1996, 14, 532–538.
3   Ogawa, Y. Injectable microcapsules prepared with biodegradable poly(α-hydroxy) acids for prolonged release of drugs. J. Biomater. Sci. Polymer Edn. 1997, 8, 391–409.
4   Jain, R.; Shah, N.H.; Malick, A.W.; Rhodes, C.T. Controlled drug delivery by biodegradable poly(ester) devices: different preparative approaches. Drug Dev. Indust. Pharm. 1998, 24, 703–727.
5   Maruyama, K.; Ishida, O.; Takizawa, T.; Moribe, K. Possibility of active targeting to tumor tissues with liposomes. Ad. Drug Delivery Rev. 1999, 40, 89–102.
6   Farokhzad, O.C.; Cheng, J.; Teply, B.A.; Sherifi, I.; Jon, S.; Kantoff, P.W.; Richie, J.P.; Langer, R. Targeted anoparticle-aptamer bioconjugates for cancer chemotherapy in vivo. Proc. Natl. Acad. Sci. 2006, 103, 6315-6320.
7   Menger, F. M.; Zhang, H.; de Joannis, J.; Kindt, J. T. Solubilization of Paclitaxel (Taxol) by Peptoad Self-Assemblies. Langmuir   2007, 23, 2308-2310.
8   Ooya, T.; Lee, J.; Park, K. Hydrotropic dendrimers of generations 4 and 5: Synthesis, characterization, and hydrotropic solubilization of paclitaxel. Bioconjugate Chem. 2004, 15, 1221-1229.
9   Lee, C. C.; Yoshida, M.; Frechet, J. M. J.; Dy, E. E.; Szoka, F. C. In Vitro and in Vivo Evaluation of Hydrophilic Dendronized Linear Polymers. Bioconjugate Chem. 2005, 16, 535-541.
10   Nie, S.; Xing, Y.; Kim, G. J.; Simons, J. W. Nanotechnology applications in cancer. Annu. Rev. Biomed. Eng. 2007, 9, 257–88.
11   Jin, S.; Ye, K. NP-Mediated Drug Delivery and Gene Therapy. Biotechnol. Prog. 2006, 23, 32–41.
12   Xua, Z.P.; Zengb, Q. H. ; Lua, G.Q. ; BingYub, A. Inorganic nanoparticles as carriers for efficient cellular delivery. Chemical Engineering Sci 2006, 61, 1027 – 1040.
13   Berry, C.C. Possible exploitation of magnetic nanoparticle–cell interaction for biomedical applications. Mater. Chem 2005, 15, 543-547.
14   Burt J.L.; Gutiérrez-Wing, C.; Miki-Yoshida M. José-Yacamán, M. Noble-metal nanoparticles directly conjugated to globular proteins. Langmuir 2004, 26, 11778-11783.
15   Elechiguerra, J. L.; Burt, J.L.; Morones, J.R.; Camacho-Bragado, A.; Gao, X., Lara, H.H.; Yacaman, M.J. Interaction of silver nanoparticles with HIV-1. Nanobiotechnology 2005, 3, 6–15.
16   Fei, L.; Perrett, S. Effect of Nanoparticles on Protein Folding and Fibrillogenesis. Int. J. Mol. Sci. 2009, 10, 646-655.
17   Wu, X.; Narsimhan, G. Effect of surface concentration on secondary and tertiary conformational changes of lysozyme adsorbed on silica nanoparticles. Biochim. Biophys. Acta 2008, 1784, 1694-1701.
18   Vertegel, A.A.; Siegel, R.W.; Dordick, J.S. Silica nanoparticle size influences the structure and enzymatic activity of adsorbed lysozyme. Langmuir 2004, 20, 6800-6807.
19   Ghosh, P.; Han, G.; De, M.; Kim, C. K.; Rotello, V. M. Gold NPs in Delivery Applications. Adv Drug Del. Rev. 2008, 60, 1307-1315.

20 Han, G.; Ghosh, P.; Rotello, V. M. Functionalized Gold NPs for Drug Delivery. Nanomedicine 2007, 2,113–123.

21 Paciotti, G.F.; Myer, L.; Weinreich, D.; Goia, D.; Pavel, N.; McLaughlin, R.E.; Tamarkin, L. Colloidal Gold: A Novel NP Vector for TumorDirected Drug Delivery. Drug Deliver 2004, 11,169-183.

22 Peelle, B. R.; Krauland, E. M.; Wittrup, K. D.; Belcher, A. M. Design Criteria for Engineering Inorganic Material-Specific Peptides. Langmuir 2005, 21, 6929-6933.

23 Hillyer J.F.; Albrecht R.M. Gastrointestinal persorption and tissue distribution of differently sized colloidal gold NPs. J Pharm Sci. 2001, 90, 1927-1936.

24 Hillyer, J.F.; Albrecht, R.M. Correlative instrumental neutron activation analysis, light microscopy, transmission electron microscopy, and Xray microanalysis for qualitative and quantitative detection of colloidal gold spheres in biological specimens. Microsc Microanal. 1999, 4, 481-490.

25 Albrecht R.M.; Simmons S.R.; Pawley J.B. Correlative video-enhanced light microscopy, high voltage transmission electron microscopy, and field emission scanning electron microscopy for the localization of colloidal gold labels. New York: Oxford University Press, 1993, 151–176.

26 Hainfeld, J.F.; Slatkin, D.N.; Focella, T.M.; Smilowitz, H.M. Gold NPs: a new X-ray contrast agent. Brit. J. Radiol 2006, 79, 248–253.

27 Shi, R.Z.; Lyons, S.D.; Christopherson, R.I. Metabolic effects of thiopurine derivatives against human CCRF-CEM leukaemia cells. Int J Biochem Cell Biol. 1998, 30, 885-895.

28 Burchenal J.H.; Murphy M.L.; Ellison R.R.; Sykes M.P.; Tan T.C.; Leone L.A.; Karnofsky D.A.; Craver L.F.; Dargeon H.W.; Rhoads C.P. Clinical evaluation of a new antimetabolite, 6-mercaptopurine, in the treatment of leukemia and allied diseases. Blood 1953, 8, 965-999.

29 Bergmann, F.; Kwietny, H.; Levin, G.; Brown, D.J. The action of mammalian xanthine oxidase on N-methylated purines. J. Am. Chem. Soc. 1960, 82, 598-605.

30 Pacher, P.; Nivorozhkin, A.; Szabó, C. Therapeutic Effects of Xanthine Oxidase Inhibitors: Renaissance Half a Century after the Discovery of Allopurinol. Pharmacol Rev, 2006, 58, 87-114.

31 Borges, F.; Fernandes, E.; Roleira, F. Progress towards the discovery of xanthine oxidase inhibitors. Curr Med Chem., 2002, 9, 195-217.

32 Podsiadlo, P.; Sinani, V.A.; Bahng, J. H.; Shi Kam, N.W.; Lee, J.; Kotov, N.A. Gold NPs Enhance the Anti-Leukemia Action of a 6-Mercaptopurine Chemotherapeutic Agent. Langmuir, 2008, 24, 568-574.

33 Viudez, A.J.; Madueño, R.; Pineda, T.; Blazquez, M. Stabilization of gold nanoparticles by 6-mercaptopurine monolayers. Effects of the solvent. J Phys Chem B 2006, 36, 17840-17847.

34 Sinani, V.A.; Podsiadlo, P.; Lee, J.; Kotov, N. A.; Kempa, K. Gold nanoparticles with stable yellow-green luminescence. Int. J. Nanotechnol. 2007, 4, 239-251.

35 Kadar, P., Wujik, C.E. Remediation of undesirable secondary interactions encountered in hydrophilic interaction chromatography during development of a quantitative LC-MS/MS assay for a dipeptidyl peptidase IV (DPP-IV) inhibitor in monkey serum. E. J. Chromatogr. B, 2009, 877, 471-476.

36 Kotov, N.A., Liu, Y., Wang, S., Cumming, C., Eghtedari, M., Vargas, G., Motamedi, M., Nichols, J., Cortiella, J., Inverted Colloidal Crystals as Three-Dimensional Cell Scaffolds. Langmuir, 2004, 20, 7887-7892.

37 Lee, J., Cuddihy, M.J., Kotov, N.A., Three-dimensional cell culture matrices: State of the art. Tissue Engineering Part B-Reviews, 2008, 14, 61-86.

38 Zhang, Y., Wang, S., Eghtedari, M., Motamedi, M., Kotov, N.A., Inverted-Colloidal-Crystal Hydrogel Matrices as Three-Dimensional Cell Scaffolds. Advanced Functional Materials, 2005. 15, 725-731.

39 Inui, K.I.; Masuda, S.; Saito, H. Cellular and molecular aspects of drug transport in the kidney. Kidney Int., 2000, 58, 944–958.

40 Berkhin, E.B.; Humphreys, M.H. Regulation of renal tubular secretion of organic compounds. Kidney Int., 2001, 59, 17–30.

41 Masereeuw, R., Russel, F.G. Mechanisms and clinical implications of renal drug excretion. Drug Metab Rev 2001, 33, 299–351.

42 Mawatari, H.; Unei, K.; Nishimura, S.; Sakura, N.; Ueda, K. Comparative pharmacokinetics of oral 6-mercaptopurine and intravenous 6-mercaptopurine riboside in children. Pediatrics International 2001, 43, 673–677.

43 Lee, J., Cuddihy, M.J., Catera, G.M., Kotov, N.A., Engineering liver tissue spheroids with inverted colloidal crystal scaffolds. Biomaterials, 2009, 30, 4687-4694.

44 Eeckhaut, A.V.; Lanckmans, K.; Sarre, S.; Smolders, I.; Michotte, Y. Validation of bioanalytical LC-MS/MS assays: evaluation of matrix effects. J. Chromatogr. B 2009, 877, 2198-2207.

45 Chiu, M. L.; Lawi, W., Snyder, S. T., Wong, P. K., Liao, J. C., Gau, V. Matrix Effects—A Challenge toward Automation of Molecular Analysis. J. Assoc. Lab. Autom 2010, 15, 233-242.

46 Marquis, B. J.; McFarland, A.D.; Braun, K.L.; Haynes, C.L. Dynamic measurement of altered chemical messenger secretion after cellular uptake of nanoparticles using carbon-fiber microelectrode amperometry. Analytical Chem., 2008, 80, 3431-3437.

47 Lee, J., Shanbhag, S., Kotov, N., Inverted colloidal crystal scaffolds as three-dimensiona microenvironments for cellular co-cultures, J. Mater. Chem., 2006, 16, 3558.

48 Abbott, A., Cell culture: biology's new dimension. Nature, 2003, 424, 6951, 870-2.

49 MA Swartz. Capturing complex 3D tissue physiology in vitro. Nature Rev. Mol. Cell Biol. 7:211-224 (2006).

CHAPTER 3

BRAIN PENETRATION, DISTRIBUTION AND PHARMACOKINETICS
OF 6-MERCAPTOPURINE RIBOSIDE CONJUGATED GOLD NANOPARTICLES

3.0   INTRODUCTION

Each year, approximately 14,000 people are stricken with brain cancer. Despite major advances in diagnostics and treatment options, the ability to treat the most aggressive and common form of malignant brain tumor, glioblastoma multiforme (GBM), has not improved since 1980.[1] GBM is the most frequent primary brain tumor type in adults, comprising about a quarter of all primary brain tumors diagnosed in the United States. The one-year survival rate for invasive central nervous system (CNS) cancers was 57.9 percent in 2002, and survival for GBM in particular was even lower.[2] Even with aggressive multimodal therapy consisting of radiotherapy, chemotherapy, and surgical excision, the median survival is only 12–17 months.[3]

One reason for this is that the majority of the potent systemic chemotherapeutic agents are excluded from the CNS by the Blood-Brain Barrier (BBB) and Blood-Cerebrospinal Fluid (BCSF) Barriers.[4] The BBB is composed of a tightly sealed layer of endothelial cells and astrocytes and plays a critical role in protecting the brain from toxic and infectious agents, while allowing the intake of nutrients, oxygen and essential molecules. Highly complex and tightly regulated, the BBB screens the biochemical, physicochemical and structural features of solutes in its periphery, thus affording barrier selectivity in the passage of molecules into the brain parenchyma.

The ability to treat neurological diseases is therefore limited by the efficient function of BBB and BCSF barrier. In addition, BBB efflux proteins such as P-glycoprotein and ABCG2 act like gate keepers to keep the chemotherapeutics out of CNS. A few compounds classified as nitrosoureas (including carmustine and lomustine) or alkylating agents (e.g. temozolomide) have

partial ability to cross the BBB and have been used clinically in the recent past.[5] However, systemic delivery of these agents appears to offer modest benefit as a supplement to radiotherapy. [6,7] In effect, the BBB and BCSF act as a bottleneck to the development of effective brain delivery systems.

The failure of conventional drug therapy for treating glioma has motivated extensive research into innovative strategies to deliver chemotherapeutics across the BBB. Over the past two decades, a variety of approaches to deliver CNS-excluded drugs through the BBB have been attempted by various research groups with mixed results. These have included hyperosmolar disruption of the BBB tight junctions and direct delivery of therapeutics into the brain by intracerebral injection into cerebral parenchyma or cerebral ventricles.[8,9] Both approaches are invasive, and have severe adverse effects with a prominent disadvantage of repeated administration of therapeutic agents.

With better understanding of the BBB, several targeting strategies are being tested for brain delivery, with some success.[10] Receptor-mediated delivery of drugs conjugated to known BBB carriers such as transferrin, apotransferrin and other ligands have been tested.[11] Liposome and nanoparticles with similar targeting moieties have also been evaluated. However despite the fact that some of these approaches have achieved increased drug delivery into the brain, the therapeutic efficacy decreases either due to chemical modifications or a poor drug penetration thus limiting their usefulness.[12] The ability to cross the BBB would enable a wider range of agents such as paclitaxel, doxorubicin, immunotoxins, and even gene therapy vectors to be evaluated for brain cancer treatment.

In order to overcome the poor permeability of the BBB as well as poor pharmaceutic properties of currently marketed chemotherapeutic agents, we have put forward a novel drug delivery strategy which involves the conjugation of 6-MPR to gold nanoparticles (6-MPR-AuNPs). The proposed research utilizes whole-body section fluorescence imaging (WBSFI) technique, as well as detailed brain, CSF and plasma PK analyses to study the brain uptake and CNS distribution of 6-MPR-AuNPs following intravenous injection of rats.

In the recent past, gold nanoparticles have attracted considerable attention for medical research. This is because AuNPs are chemically stable, biocompatible, easy to functionalize for specific targeting, and have special plasmonic properties.[13–17] The intravenous lethal dose

(LD50) of 1.9 nm AuNPs was found to be minimal (3.2 g/kg) in acute toxicity studies conducted in mice.[18] As a contrast agent, AuNPs provide a suitable tool for diagnostics and imaging. [19−21] Moreover, the luminescence of gold and its electron density allow its visualization and characterization by numerous techniques such as spectrophotometry, fluorescence microscopy, computer tomography (CT), and transmission electron microscopy (TEM). Previous experiments which reported the entry of citrate stabilized gold nanoparticles (AuNPs) into the brain after intravenous administration showed that gold nanoparticles with a diameter cut-off of 15 nm or 50 nm could pass through the BBB efficiently. [18,22] Although several studies are available on the use of gold nanoparticles for diagnostic and therapeutic applications, detailed analysis of the pharmacokinetics and brain distribution of drugs conjugated to gold nanoparticles is nonexistent or incomplete. Further investigation of the distribution and kinetics of drug conjugated AuNPs is warranted, and will help shed light on the safety and efficacy of nanotherapeutics in general.

Additionally, recent development of better fluorescent tags as well as advances in image computing, have sparked new interest in the use of optical imaging as a medical diagnostic. WBSFI is increasingly gaining popularity as a qualitative tool used in non-clinical drug research. [23,24] WBSFI is similar to QWBA, but fluorescence intensity is measured instead of radioactivity.

In WBSFI, flourophores are used to visualize disposition of tagged drug molecules in whole body section of small animals. Compared to other imaging methods, WBSFI is safe, fast, inexpensive, requires little sample preparation while maintaining high sensitivity. It was not the aim of the present publication to review in detail the performances of WBSFI and QWBA. Rather we focus on the new possibilities offered by 6MPR-AuNPs combined with WBSFI.

Purine antimetabolites, 6-mercaptopurine (6MP) and 6-mercaptopurine riboside (6MPR) are antineoplastic agents widely used in the clinical treatment of Acute Lymphoblastic Leukemia (ALL), meningeal leukemia, other malignancies, and inflammatory bowel disease (IBD).[25] Short plasma half-life due to rapid liver metabolism has limited their clinical use. Furthermore, only limited published information is available on the brain distribution of 6-MPR and other purine analogs. Available studies suggest that 6-MPR is only marginally distributed in the CNS. [25]

The mechanism of action of purine antimetabolites involves the conversion of mercaptopurine into cytotoxic 6-thioguanine nucleotide (6-TGN), which is then incorporated into the DNA or RNA of nucleated cells by hypoxanthine-guanine phosphoribosyl transferase

(HGPRT) instead of the naturally occurring purine bases (Figure 3-1-1).[26] These events ultimately lead to cell death and is thought to be the source of the antineoplastic effects of mercaptopurines. Conventional therapies with mercaptopurines are however susceptible to extensive enzymatic inactivation by hepatic xanthine oxidase, resulting in short plasma half-life and large variability in cytotoxic efficacy.[27, 28] The pathway involves conversion of mercaptopurine to 6-thiouric acid, and thiopurine methyltansferase catalysis of S-methylation to 6-methylmercaptopurine.[29] The importance of optimizing 6-MP therapy to maintain high systemic exposure is therefore critical to effective clinical management of Acute Lymphoblastic Leukemia (ALL).

In this article we present compelling animal data to show that 6-MPR-AuNPs significantly increased the concentrations of 6-MPR and 6-MP in brain, CSF and plasma. The AuNPs decreased the clearance and thereby increased the plasma half-life of 6-MPR. Finally, TEM and whole-body imaging analysis was used to confirm the brain uptake of 6-MPR-AuNPs. Considering the anatomical complexity of the blood-brain-CSF barriers and the inherent difficulty in delivering drugs to the brain, the significance of finding AuNPs in brain and cerebrospinal fluid cannot be overstated.

To our knowledge, this is the first time a pharmacological agent has been directly delivered to brain parenchymal cells using gold nanoparticles as vectors. We are also unaware of reports of transvascular delivery of the chemotherapeutics agent (6-MPR) across the blood-brain using AuNPs, combined with the potential for other novel drug delivery applications. Furthermore, to-date, there have been no reported cases of the successful use of whole-body fluorescence to investigate tissue distribution of nanoparticles in lieu of whole body autoradioluminography as we have demonstrated in this article. Finally, drug design strategies for treating brain malignancies have often emerged from empirical studies with retrospective pharmacologic explanations, rather than prospective trials involving rational design as we have done here.
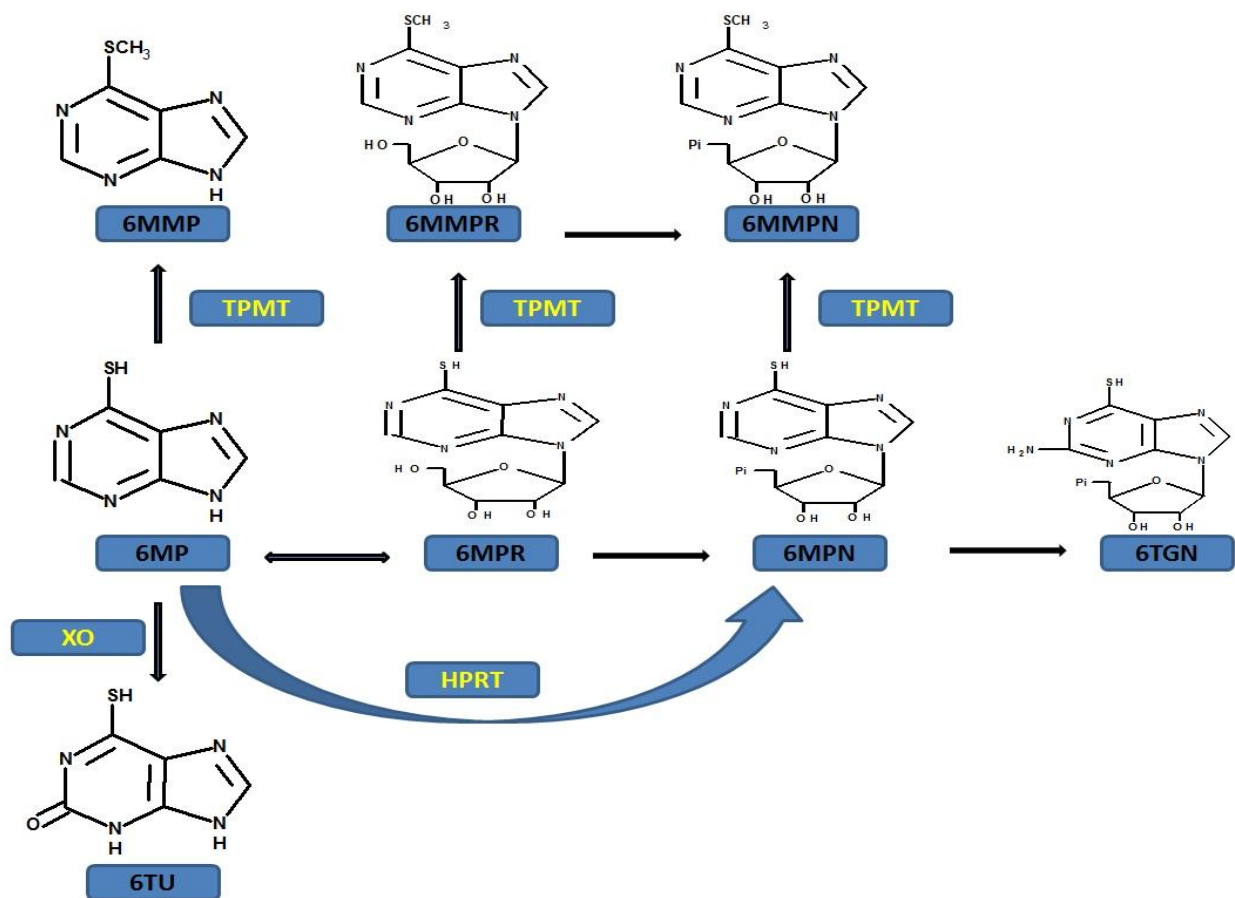
Figure 3-1-1. Schematic of the metabolism of 6-mercaptoputine (6MP) and 6-mercaptopurine riboside (6MPR). 6MPN, 6-mercaptopurine nucleotides; 6TGN, 6-thioguanine nucleotides; 6MMP, 6-methylmercaptopurine; 6MMPR, 6-methylmercaptopurine riboside; 6MMPN, 6-methylmercaptopurine nucleotides; 6TU, 6-thiouric acid; TPMT, thiopurine methyltransferase, HPRT, hypoxanthine phosphoribosyltransferase; XO, xanthine oxidase.

3.1   METHODS

3.1.1   Materials

6-Mercaptopurine riboside, 6-Mercaptopurine, trisodium citrate dihydrate, tetrachloroauric (III) acid trihydrate, sodium borohydride, L-cysteine and fluorescein isothiocyanate isomer I (FITC) were purchased from Sigma-Aldrich and utilized without further purification. Ultrapure water (Barnstead) with 18.2 MΩ-cm was used for all experiments.

3.1.2   6-MPR-AuNPs and FITC/6-MPR-AuNPs Synthesis

Citrate stabilized gold nanoparticles were freshly prepared and used immediately for the synthesis of 6-MPR-AuNPs and FITC/6-MPR-AuNPs (Figure 3-1-2). Gold sol was prepared by sodium borohydride reduction of tetrachloroauric (III) acid solutions following previously reported methods, [30−32] [42-44] with some modifications. Briefly, 5 mL of 1 w/w% tetrachloroauric (III) acid solution was diluted in 50 mL of ultrapure water and stirred for one minute. Next 2.5 mL of 3.4mM sodium citrate was added and the resulting solution was stirred for one minute. 5 mL of 0.075 wt% sodium borohydride was then added to the gold solution.

6-MPR-AuNPs were labeled with FITC via an L-cysteine linker. 50 mL aqueous solution containing a 2:1 molar ratio of 6-MPR and Cysteine were added to the reaction vessel containing gold sol 30s after sodium borohydride. The resulting solution was dialyzed against ultrapure water for 3 days and was further purified by ultracentrifugation at 45000 rpm (190000 *gr max*) to a final volume of 20mL. To the resulting dispersion, a 1mL solution containing 0.58umol of FITC was added and after adjusting the pH to 8, the mixture is allowed to stir

overnight in darkness at room temperature. Next, the solution is placed in a dialysis bag and allowed to purify against ultrapure water for approximately one week or until no more FITC was eluting. The resulting NP solution was stored in a refrigerator and protected from ambient light, until further use.
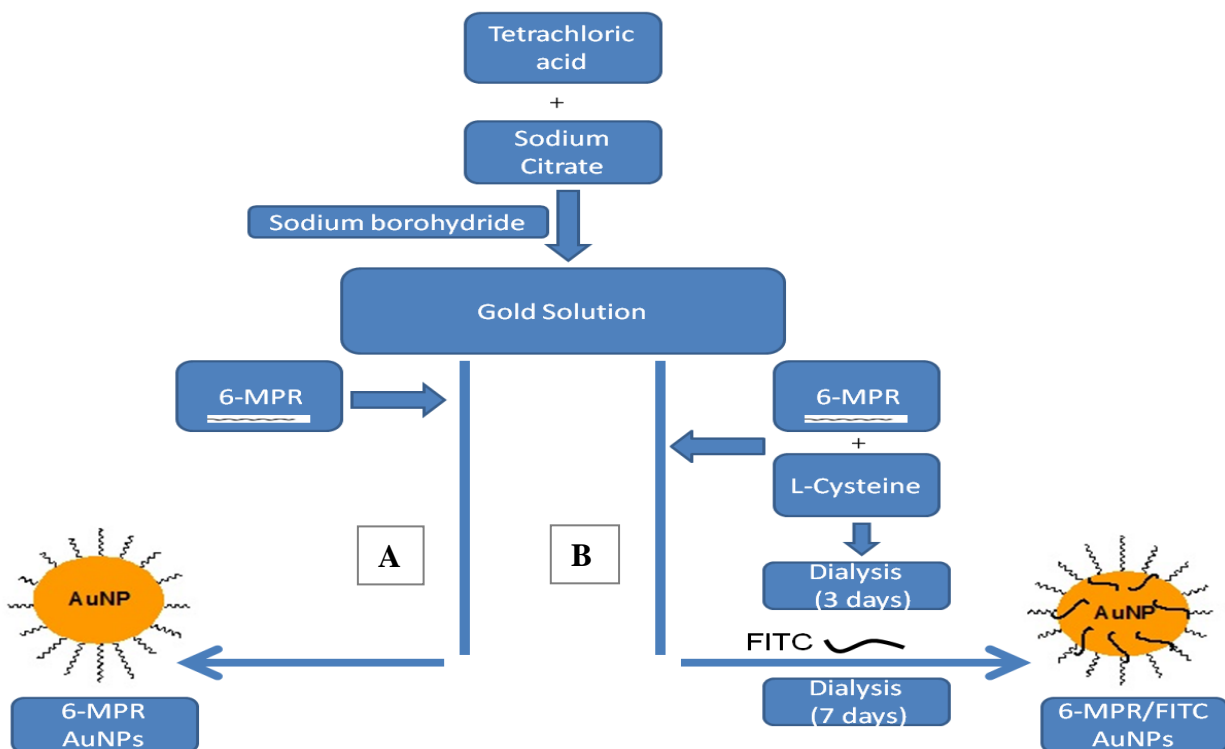
Figure 3-1-2. Flow diagram for the chemical synthesis of 6-MPR-AuNP (route A) and FITC/6-MPR-AuNPs (route B)

3.1.3 Nanoparticle Characterization

3.1.3.1 TEM Imaging

Transmission electron microscopy (FEI Tecnai, G2 Sphera) imaging was performed on FITC/6-MPR-AuNP and 6MPR-AuNP solutions at 100,000 times magnification. Mean surface area and diameter of the particles were then determined using Image-Pro Plus software (Media Cybernetics). To prepare samples for TEM, 2-5 μL aliquots of the sample were placed onto carbon-coated formvar covered support grids and air-dried overnight in a protective environment. Representative images from samples at 100,000x were used to acquire sufficient (greater than 100) nanoparticle objects for image analysis. Images were processed to optimize particle segmentation. Statistics and frequency histograms were generated. The zeta potential of 6MPR-AuNP was measured using Zetasizer Nano ZS, Malvern Instruments. Finally, High Pressure Liquid Chromatography (Agilent HPLC System) was used to determine the concentration of 6MPR immobilized on the surface of AuNPs by digesting the gold colloids with potassium cyanide.

3.1.3.2 AFM Imaging

Atomic force microscopy (AFM) imaging was performed using a Nanoscope III (Digital Instruments/ Veeco, Santa Barbara, CA) instrument. AFM images were obtained in the tapping mode with standard Si/N tips. Calibration at the nanoscale, operating in Tapping Mode (TM) was performed using standard samples. Images were recorded by working in low voltage mode. In this configuration the set point was about 1 nN, and the scan rate 2 Hz. Glass slides were cleaned by immersion in a freshly prepared solution consisting of 30% H_2O_2 and 96% H_2SO_4 in 1:2 ratio.

The glass substrates were then washed with milli-Q water and dried in a stream of high-purity nitrogen. Subsequently, the glass surface was treated with 0.3M (3-mercaptopropyl)-trimethoxysilane solution in chloroform for 3 minutes at room temperature. The slides were finally rinsed with copious chloroform and milli-Q water and dried with nitrogen gas. Gold colloids were deposited on silanized glass slides by spin coating. Spin speed and time were adjusted to ensure high density of homogeneously distributed single colloidal particles over the glass substrate.

3.1.4   Animal Studies

Male Sprague-Dawley rats weighing on average 250-300 grams with surgically implanted vascular cannulas in the carotid artery and jugular vein were purchased from Charles River Laboratories (Willmington, MA). Rats were housed one per cage in an American Animal Association Laboratory Animal Care accredited facility and maintained under standard conditions of temperature (22 ± 2 ℃), relative humidity (50%) and light and dark cycles (12 hours /12 hours). Rats were allowed to acclimate to their environment for one week. Rats had access to food and water *ad libitum* throughout the study. Experiments were conducted according to procedures approved by the Pfizer Global Research and Development Animal Care and Use Committee and complied with the NIH Guide for the Care and Use of Laboratory Animals.

3.1.4.1 Whole-Body Imaging Experiment

Rat whole-body fluorescence imaging studies were conducted following standard procedure for whole-body autoluminography. The experimental setup (Figure 3-1-3) consisted of a cryomicrotome, the imaging system, a robotic positioner and the computer control system.

A custom application program has been developed which controls the cryostat, the robotic positioner, the illuminators and the camera for a fully automated sectioning and imaging session. A total of six rats were used in the study. Three rats (treatment groups 1-3) were intravenously administered FITC/6-MPR-AuNP (5 mg/kg FITC), and the remaining three rats received either saline, FITC or FITC + 6-MPR-AuNP as control. The saline group was included to control for both the drug administration and temporary restraints used. All rats were injected via the tail vein using 20-gauge gavage-dosing needle affixed to a 3cc disposable syringe.
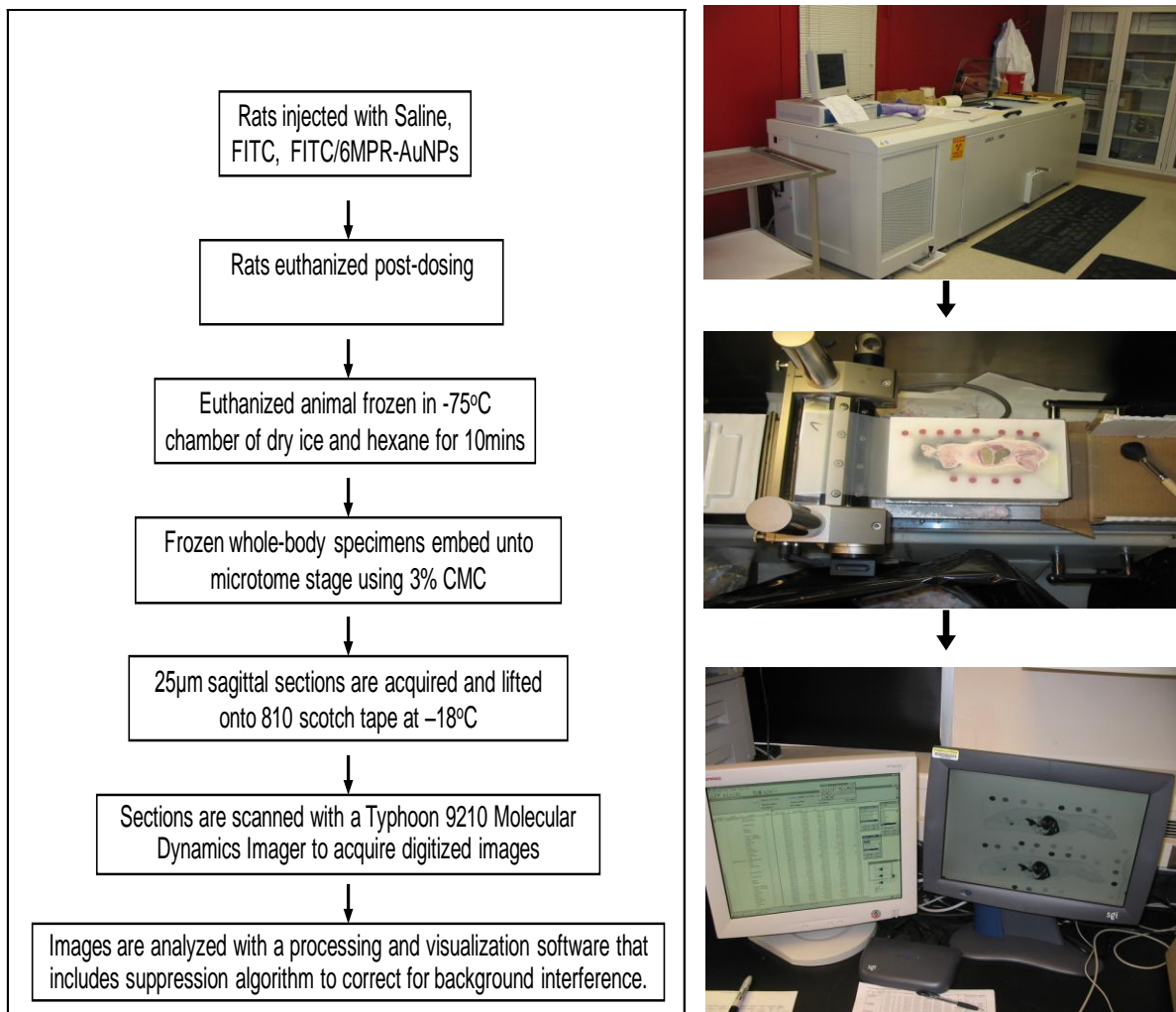
Figure 3-1-3. Procedure flow diagram of rat whole-body fluorescence experiment.

Rats were then euthanatized by CO2 asphyxiation 30 minutes following dose administration. Immediately following euthanasia, each rat was prepared by immersion into a freezing chamber (-75^oC) containing dry ice and hexanes for 10 minutes. Next the frozen whole-body specimen was embedded onto a microtome stage using 3% carboxy-methylcellulose. 25µm sagittal sections were captured on type 810 Scotch tape at -18^oC. Sections were then freeze-dried at -18^oC for a minimum of 72 hours. The cryosections were scanned with a Typhoon 9210

Molecular Dynamics Phosphor Imager to acquire computerized images optimized for detecting FITC. Tissue sections were spotted with matrix solution to generate a linear concentration–response relationship over a 1000-fold concentration range of FITC. Photographic registration was obtained by averaging fluorescence measured at different sectioning levels and from replicate cryosections obtained from the same sectioning level. The acquired images were analyzed with a processing and visualization system. Background scans acquired prior to dosing were fed into a suppression algorithm to correct for background interference.

3.1.4.2 Brain, CSF, Plasma Distribution Study

SD rats (three per timepoint) received a slow fixed bolus injection of 6MPR-AuNPs (5 mg/kg active) via JVC, with no clinical observations. 6MPR solution was administered as a control. At 0.083, 0.25, 0.5 and 0.75 hours post-injection, rats were euthanized by carbon dioxide, and plasma, cerebral spinal fluid and brain were collected for analysis. Whole blood was collected via carotid artery cannula (CAC) into heparinized tubes (with EDTA) followed by complete exsanguination. After each blood draw, rats were injected with 0.25 mL normal saline (0.9% sodium chloride, USP) to maintain a constant blood volume. Plasma was immediately separated by centrifugation at 13000 *gr-max* for 5 minutes, and transferred to glass culture tubes. Samples were stored frozen at -20°C until analysis. CSF was collected via puncture of the cisterna magna using a 23 gauge needle attached to polyethylene tubing (internal diameter of 50 mm) and syringe. Whole brains were harvested, rinsed in phosphate buffered saline and weighed.

Brain samples were homogenized in 60:40 isopropanol: water immediatley after harvesting. All samples were immediately frozen on dry ice until analysis. Sagittal sections of rat brain were obtained 15 minutes post-injection for TEM imaging. The brain was removed

immediately from the skull, fixed in chilled 2.5% glutaraldehyde solution for 2 hours and then embedded into epoxy resin. The tissues were allowed to equilibrate to room temperature for approximately one hour before sectioning. Ultra-thin (60-80nm) sagittal sections were cut using an ultramicrotome with a diamond knife. The specimen was placed onto carbon-coated formvar covered support grids. Three adjacent brain slices from the same animal were collected. After being stained with uranyl acetate and lead citrate, the specimens were observed on a TEM.

3.1.4.3 Sample Preparation

Standard curves and quality control samples (n=3 for each concentration) were prepared in control rat plasma. For plasma samples, a 50 µL aliquot of sample was precipitated with 200 µL of acetonitrile containing internal standard using a VWR Multi-Tube Vortexer (VWR, Bridgeport, NJ). For brain samples, 50 µL of blank plasma was added to 50 µL of homogenized (4-fold dilution in 60/40 Isoproponal/Water) sample. For brain standards and blanks, 50 µL of control rat brain homogenate was added to 50 µL of plasma. The resulting 100 µL of sample was precipitated with 300 µL of acetonitrile containing internal standard using a VWR Multi-Tube Vortexer. All samples were then centrifuged at 3000 rpm for 10 minutes with a standard laboratory centrifuge (Eppendorf, Westbury, NY). The supernatant was collected in a clean 96-well collection plate and 5 µL was injected onto the HPLC for LC/MS/MS analysis.

3.1.4.4 6-MPR and 6-MP Bioanalysis

LC/MS/MS analysis was performed for 6MPR and 6MP using a high-performance liquid chromatography system with CTC PAL autosampler (Leap Technologies, Carrboro, NC) interfaced to an API 4000 LC/MS/MS quadrupole tandem mass spectrometer (Applied

Biosystems/ MDS Sciex Inc., Ontario, Canada). 6MPR, 6MP and the internal standard (CP-628374) were separated on a Waters Atlantsi HILIC column[33] (50 x 2.1 mm, 5μm) by isocratic elution. Mobile phase A consisted of 95% Acetonitrile and 5% 200 mM ammonium formate in water, pH 3.0. Mobile phase B, which was used as a 0.5 minute wash step, consisted of 50% Acetonitrile, 45% HPLC Grade Water, and 5% 200 mM ammonium formate in water, pH 3.0. A flow rate of 650 μL/min was used. The mass spectrometer was operated in negative ion ESI mode for the detection of 6MPR and the Internal Standard (CP-628374). Multiple reaction monitoring was performed with the transitions m/z 283.2 → 151.1 for 6MPR, m/z 685.3 → 366.1 for CP-628374 (internal standard). The mass spectrometer was operated in positive ESI mode for the detection of 6MPR and the Internal Standard (CP-628374). Multiple reaction monitoring was performed with the transitions m/z 153.1 → 119 for 6MP, m/z 687.3 → 319.7 for CP-628374 (internal standard). All raw data was processed using Analyst Software v.1.4.2 (Applied Biosystems/ MDS Sciex Inc., Ontario, Canada). The lower limits of quantification (LLOQ) for 6MPR and 6MP were 2.44 and 9.76 ng/mL, respectively. The upper limit of quantification (ULOQ) was 1250 ng/mL.

3.1.4.5 Pharmacokinetic Analysis

Mean concentrations of 6MPR and 6MP were used in the analysis. Paired student's t-test was used to determine statistical significance and was assessed at the 5% level ($p < 0.05$). Pharmacokinetic analysis was performed using standard noncompartmental methods as implemented in Watson Kinetica™ Version 5.0 Software (Thermo Scientific, Waltham, MA). Linear-up/log-down method of estimation was used to calculate area under the concentration-time curve (AUC). Total body clearance (CL) was calculated as dose divided by AUC and

adjusted for body surface area .The steady state volume of distribution (V_{dss}) was calculated as the ratio of CL to the slope of the terminal log-linear phase – the elimination rate constant (k_e). The terminal half-life (t½) was calculated as ln2 divided by k_e. Initial concentration (C_o) is obtained by extrapolating the first measured concentrations.

3.1.4.6 Brain, CSF, and Plasma TEM Imaging

TEM (FEI Tecnai, G2 Sphera) imaging was performed on samples of brain, cerebral spinal fluid (CSF) and plasma. 2µL aliquots of CSF, plasma, brain homogenate, or rat brain sagittal samples were placed onto carbon-coated formvar covered support grids and air-dried overnight in a protective environment. Due to variation in the viscosity of CSF, plasma and brain homogenate samples, as well as issues with electron beam penetration, additional aliquots of samples diluted with nuclease-free water were examined in order to facilitate visualization in the electron microscope. Imaging was performed on sample preparations at a 10,000 – 200,000x magnifications with accelerating voltages between 50 and 120kV.

3.2   RESULTS AND DISCUSSION

In preliminary experiments conducted in our laboratory, 5nm 6-MPR-AuNPs labeled

with fluorescein isothiocyanate (FITC) was intravenously administered into male Sprague-

Dawley (SD) rats. Imaging analyses of rat sagittal sections revealed strong fluorescence

responses in several tissues, including cerebrum, cerebellum and spinal cord. Based on these

results, we further conducted detailed brain distribution and pharmacokinetics studies using the 5

nm 6MPR-AuNPs.

3.2.1   Nanoparticles

3.2.1.1 Transmission electron microscopy

Transmission electron microscopy (TEM) imaging analysis of the FITC/6-MPR-AuNPs

revealed mean particle size and surface area of ca.5.57 nm and 30.22 μm^2, respectively. The

electrokinetic potential of FITC-6-MPR-AuNPs was +8.1 mV. Similarly the particle size of

6-MPR-AuNPs was 5.12 nm, surface area was 30.59 μm^2 and the zeta potential was +7.4 mV. In

contrast to FITC/6-MPR-AuNPs, 6-MPR-AuNPs had a slightly less positive surface charge.

TEM micrographs are shown in Figure 3-2-1a and Figure 3-2-1d. Histogram (Figure 3-2-1c and

Figure 3-2-1f) based on TEM analysis of over 125 particles revealed a monodisperse particle-

size distribution. Finally, the concentration of 6-MPR on the surface of the AuNPs was

determined to be 0.25 mg/mL.

3.2.1.2 Atomic force microscopy

Tapping mode (TM)-AFM was carried out on the glass substrates. However, before TM-AFM analysis, samples were first tested by CM-AFM. Except for the presence of occasional 2 nm deep holes, the surface was quite flat, exhibiting a RMS roughness ranging between 0.3 to 0.5 nm over a 500 x 500 nm^2 area. Single colloids appear stably bound to the MPTMS glass substrate, and display homogeneous lateral and vertical dimension, with no evidence of aggregates. Micrographs of colloids are shown in Figure 3-2-1b and Figure 3-2-1e.

The particles had mean value of 5.3 nm with a standard deviation of 0.53 nm. The minimum and maximum measured heights are 4.5 and 7.2 nm, respectively. The 5.5 nm mean value of nanoparticle height, which provides an estimate of colloid diameter, is in agreement with values obtained from TEM and by the TM-AFM imaging characterization. This clearly indicates the absence of height artifacts. The lateral size (evaluated as the full width at half maximum (FWHM) of the nanoparticle cross section profile) is monodispersed and significantly broadened because of the well known tip convolution effect.
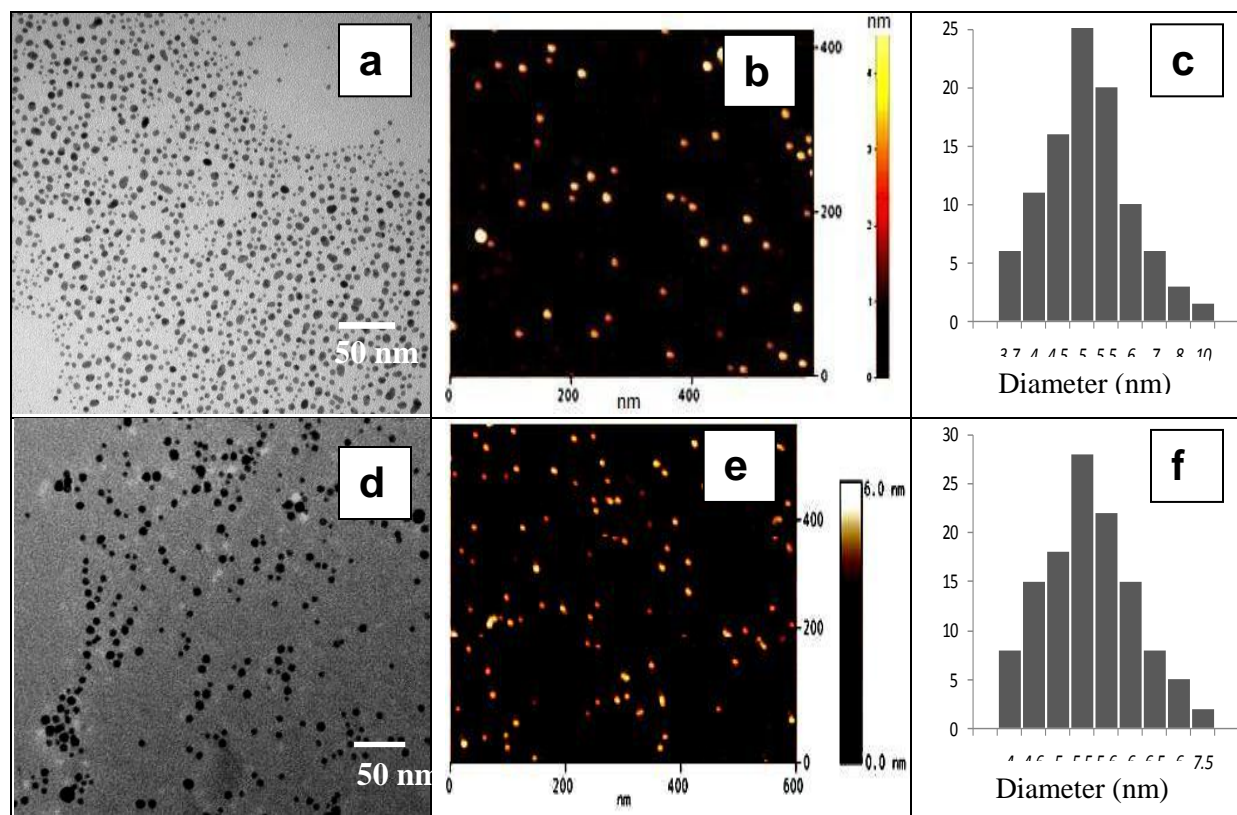
Figure 3-2-1 (a) Transmission electron micrograph of FITC/6-MPR-AuNPs (b) TM-AFM topographic image of of FITC/ 6-MPR-AuNPs deposited on MPTMS treated glass (c) Particle size histogram of FITC/6-MPR-AuNPs based on TEM analysis of 100 different nanoparticles (d) Transmission electron micrograph of 6-MPR-AuNPs (e) TM-AFM topographic image of of 6-MPR-AuNPs deposited on MPTMS treated glass (f) Particle size histogram of 6-MPR-AuNPs based on TEM analysis of 100 different nanoparticles.

3.2.1.3 Whole-Body Fluorescence Imaging

The biodistribution of 5 nm FITC/6-MPR-AuNPs following intravenous administration to Sprague-Dawley (SD) rats was investigated using whole-body cryosectioning combined with fluoroluminography (Figure 3-1-3). Across treatment groups analyzed (N=17 organs per group), widespread organ distribution was detected in several tissues (Figure 3-2-2) including bone marrow, cerebellum, cerebrum, myocardium, skeletal muscle, spinal cord, testis, salivary gland and liver, within 30 minutes of intravenous administration.

Compared to the control group, the fluorescence intensity for rats injected with FITC/6-MPR-AuNPs was highest in cerebrum, cerebellum, and cerebrospinal fluid followed by kidney, liver, spleen, lungs, bone marrow and brown adipose tissue (Table 3-1 and Figure 3-2-3). Image analysis suggests that substantial CNS uptake of FITC/6MPR-AuNPs (treatment groups 1-3) occurred. Fluorescence intensity in the brain and the inner regions are high, suggesting penetration of the blood-brain barrier by gold nanoparticles. On the other hand, rats given saline, FITC, or mixture of FITC and 6-MPR-AuNPs as a control, exhibited no or poor overall spatial distribution with no signs of uptake into brain or CSF. This suggests poor penetration of the blood-brain-CSF barriers by FITC, which has been previously reported. [34]

Extensive fluorescence in liver, kidney, bladder and lungs of rats administered FITC/6MPR-AuNP reflects the pivotal role of these organs in the clearance of nanoparticles after intravenous injection**.** Urinalysis was not performed, but the urine voided during the first 45 minutes after injection was clearly green to yellow in color, confirming urinary excretion of the test substance. The accumulation in bone marrow is especially interesting, since it is the main site of cytotoxic action of 6MPR in leukemia. One way ANOVA followed by Student-Newman-Keuls post-hoc analysis showed statistically significant difference between FITC/6-MPR-AuNPs compared to the vehicle treated group ($p < 0.05$).

Though some untreated tissues exhibited autofluorescence, whole blood produced fluorescence well above background levels. This observation was expected as hemoglobin is known to quench fluorescence of fluorophores. [35] To reduce the effect of autofluorescence, images were processed by fitting background-corrected fluorescence intensity. Using subtraction processing algorithm, interference from tissue components was substantially reduced. However,

in the interpretation of fluorescence images, one must bear in mind that the autofluorescence of tissues especially in the intestines, liver and bile cannot be completely eliminated.

The present paper describes a novel application of whole-body section fluorescence imaging (WBSFI) combined with FITC-6MPR-AuNPs for fast evaluation of systemic and central distribution of a drug candidate. Compared to other techniques, fluorescence imaging is inexpensive, less laborious and presents minimal safety concerns. WBSFI also has the advantage of having most organs available on the same section, thus permitting comparison of the test article in organs.

A major improvement of the presented approach is the use of a novel read-out technology, which overcomes the conventional time-consuming and potentially hazardous nature of autoradiographic film. Due to the high sensitivity and the rapidity of fluoroluminography, the protocol has the potential to be used for general screening of centrally active compounds, as exemplified here using 6MPR-AuNPs. However, the use of fluorescent labels for bioimaging presents certain challenges, including photobleaching, light scattering, autofluorescence by tissues, and unintended release of fluorescent tag. Also densitometric analysis such as WBSFI is quasi-quantitative.

Despite these limitations, WBSFI has proven to be a powerful tool for understanding drug disposition in early drug research. Finally, as mentioned previously, a significant finding of this study is the increase in fluorescence in the CNS after injection with FITC/6MPR-AuNPs compared to the control. The mere possibility that FITC/6MPR-AuNPs penetrated the CNS within 30 minutes of injection presents exciting possibilities and warrants further investigation. In light of these findings, detailed brain distribution and pharmacokinetic studies were also undertaken and the results are presented below.
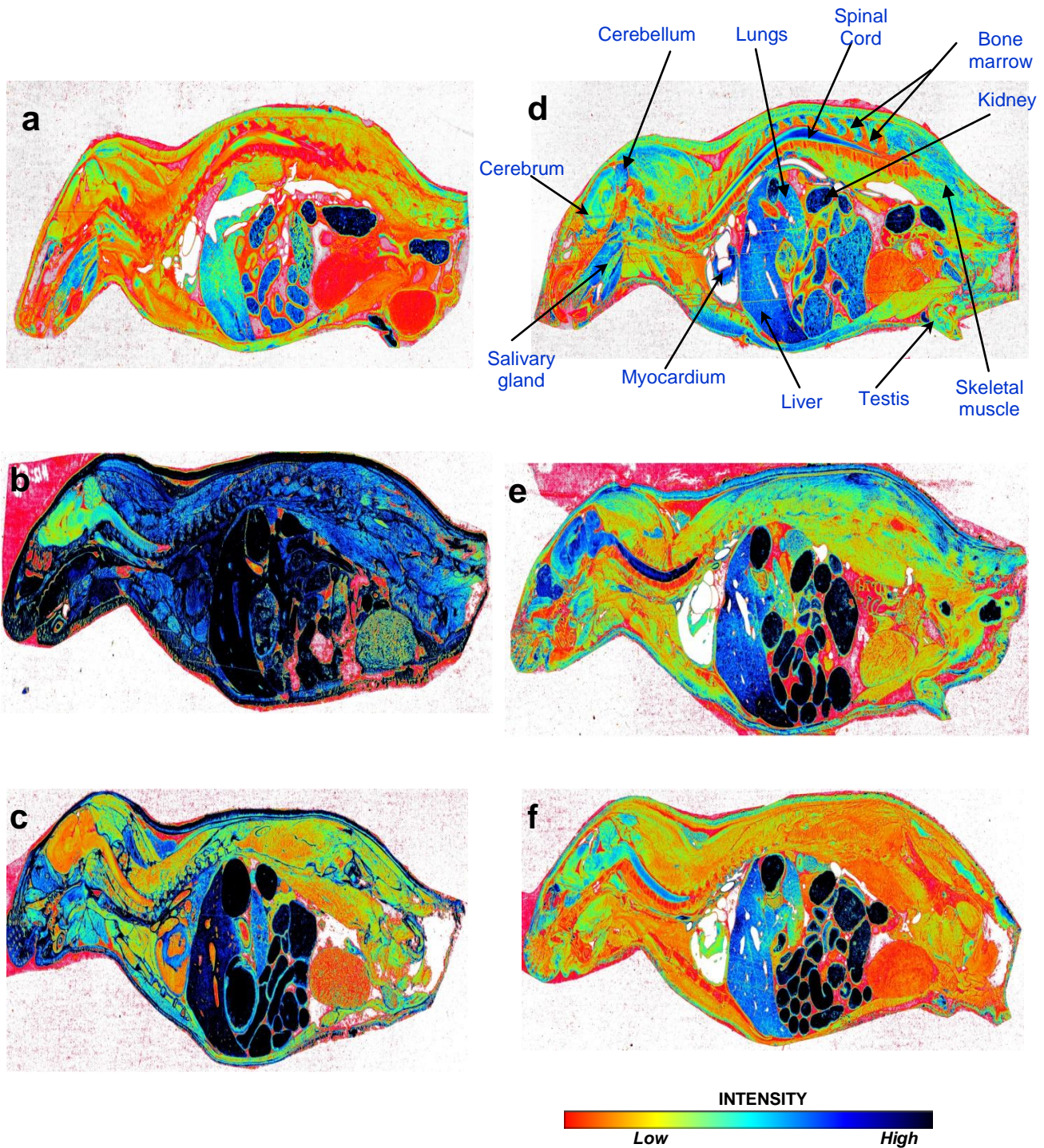
Figure 3-2-2. Whole-body fluorograms of rats administered (a) saline solution (b) 5 mg/kg FITC (c) 5 mg/kg (FITC + 6-MPR-AuNPs) (d-f) 5 mg/kg FITC/6-MPR-AuNPs. Images represent average fluorescence intensity measured from replicate cryosections of Sprague-Dawley rats sacrificed 30 minutes after intravenous injection. The intrinsic autofluorescence measured in the control rats are subtracted to get the fluorescence intensity map. Intensity of color corresponds to increasing fluorescence *(red<orange<yellow < green< blue< black)*.

Table 3-1. Fluorescence response of tissues in whole-body sections of Sprague Dawley rats following administration of vehicle control and Cys-FITC/6-MPR-AuNP

Tissue\Matrix	Control: FITC+6MPR-AuNP MDC/mm^2	Treatment group A MDC/mm^2	Treatment group B MDC/mm^2	Treatment group C MDC/mm^2
Adrenal Gland	45238312 ±114	1569566 ± 170	1669696 ± 124	1506502 ± 113
Blood	----	----	----	----
Bone Marrow	5084673 ± 201	44770476 ± 189	51841127 ± 169	52061329 ± 194
Brown Adipose	26536103 ± 214	1173443 ± 217	1473486 ± 224	1575091 ± 202
Cerebellum	491023 ± 229	24788491 ± 211	26964974 ± 246	24244603 ± 251
Cerebrum	702038 ± 671	23705402 ± 401	25939686 ± 241	26126285 ± 356
Gastric Contents	4826859 ± 167	5693628 ± 219	6137381 ± 312	5366603 ± 210
Intestinal Conten	6964151 ± 193	7286975 ± 146	6467393 ± 162	6819425 ± 211
Kidney	894972 ± 123	12343706 ± 176	14952639 ± 182	11980845 ± 213
Liver	6842549 ± 183	8461729 ± 146	7815999 ± 143	8526023 ± 312
Lung	802003 ± 132	5110253 ± 146	4786501 ± 162	5450291 ± 124
Myocardium	14671000 ± 189	404344 ± 156	449367 ± 172	490341 ± 231
Skeletal muscle	18940032 ± 102	1613146 ± 121	2167256 ± 181	1534071 ± 123
Spinal Cord	442786 ± 157	24297416 ± 181	20523301 ± 146	22778001 ± 231
Spleen	1956425 ± 144	9018464 ± 152	9534925 ± 183	8898953 ± 164
Testis	15626887 ± 119	7993181 ± 122	8290970 ± 128	8876797 ± 102
Thymus	6108133 ± 124	548771 ± 131	520040 ± 153	610119 ± 136
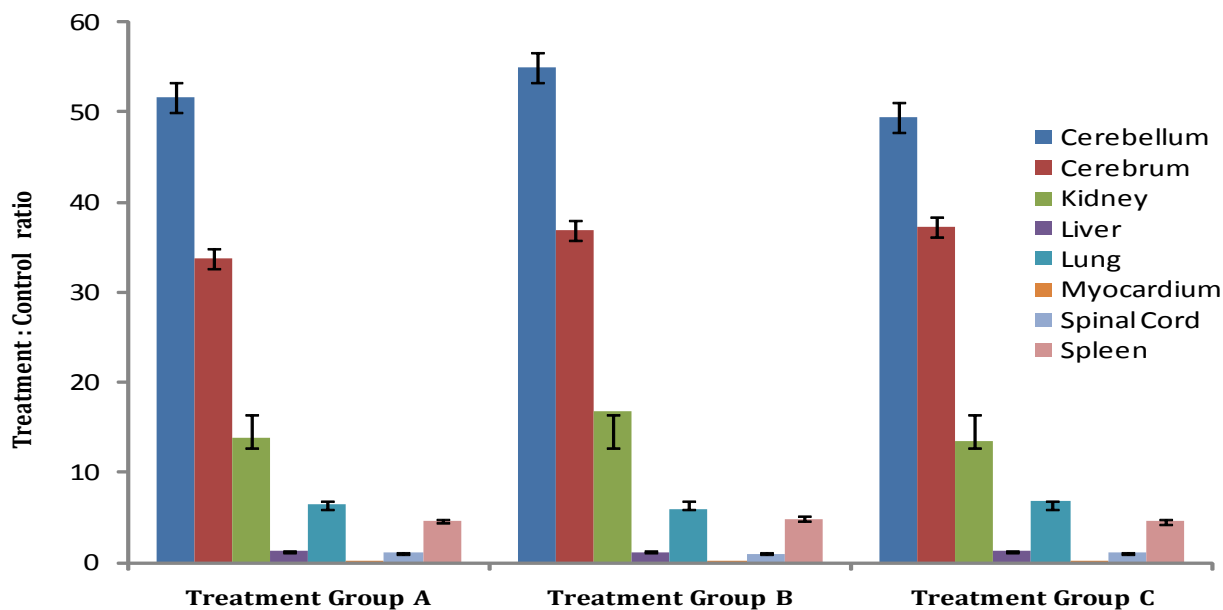
Figure 3-2-3. Treatment to control fluorescence concentration ratios (Mean ± SEM) in select tissues of Sprague Dawley rats. Each bar represents n=10 replicates per group.

3.2.1.4 Brain, CSF, Plasma Distribution

Mean brain, CSF and plasma concentrations are presented in Tables 3-2 and 3-3. Also the pharmacokinetic profiles of 6-MPR-AuNPs and unconjugated 6-MPR (control) are presented in Figure 3-2-4. The calculated pharmacokinetic parameters are summarized in Table 3-4. The difference in CSF and plasma 6-MPR concentrations for the control group was not statistically significant ($p > 0.05$) and lower than levels found in the brain. Similarly for rats treated with 6-MPR-AuNPs, the difference between brain and plasma 6-MP was not statistically significant ($p > 0.05$). For this group, the AUC of plasma 6-MPR was higher than the corresponding plasma 6-MP. The opposite was observed when unconjugated 6-MPR was administered. Overall these results revealed that brain, CSF and plasma levels of 6-MPR and 6-MP were higher in rats treated with AuNPs compared to the control group.

Specifically, the 6-MPR $AUC_{0.083-0.75\,h}$ of brain, CSF and plasma were respectively 3, 2.3 and 145 fold higher in the rats administered with 6-MPR-AuNPs compared to rats treated with 6MPR alone. Similarly, the 6-MP AUC for rats dosed with 6-MPR-AuNPs was higher relative to the control group. The slow conversion of 6MPR to 6-MP in rats treated with 6-MPR-AuNPs led to reduced 6-MP penetration into brain. This in itself is not a limitation since 6-MPR (unlike 6-MP) is itself a biologically active moiety. In general, the AuNPs provided approximately 6-times less conversion of 6-MPR to 6-MP in plasma. This is not unexpected and consistent with the high 6-MPR clearance (6076 ± 412 mL/min/kg) in the control group, compared to the clearance (41.88 ± 3.24 mL/min/kg) in rats that were given 6MPR-AuNPs. Similarly, the 6-MP clearance for the control group was 3149.51 ± 354 mL/min/kg compared to 136.23 ± 16.1 mL/min/kg for 6-MPR-AuNPs treated rats. These results are not unremarkable considering that the surface area of

brain capillaries is one-tenth that of the liver and with one-fifth the blood transit time of liver. Furthermore, the dose of AuNPs administered in this study was less than 0.2% of the LD50 of 1.9 nm AuNPs.[18]

Despite rapid elimination of 6-MPR and 6-MP, equilibration between plasma and CSF compartments after the administration of 6-MPR is achieved within one-half hour, albeit at low drug concentrations. Interestingly for the control group, the CSF concentration of 6-MP was much higher than the total plasma concentration of 6-MP. Since in general only the unbound fraction of drug in plasma can diffuse across the blood-brain barrier, the results suggest the possibility for plasma protein-binding. The free drug concentration available for brain penetration is influenced by processes, such as tissue binding in blood and brain, metabolism in the liver and brain, and active influx and efflux. Certainly on the basis of the physicochemical properties of 6-MP, passage into the CNS is to be expected.[36] The results provide additional evidence to substantiate the potential clinical benefits of 6-MP for treating leukemic meningitis.[37] The presence of 6MP in CSF after intravenous administration was first reported by Hamilton and Elion.[38] However, data on its disposition to CSF has not been available until now.

Given the extensiveness of thiopurine metabolism, conventional assessment of CNS drug delivery based on brain-plasma and CSF-plasma partition coefficients provided little useful information. Rapid conversion of 6-MPR to metabolites as well as highly exaggerated concentrations of 6-MPR in plasma (for rats given 6-MPR-AuNPs) prevented equilibrium from being reached, which is a prerequisite for performing such analyses. This study further highlights several important considerations when interpreting CNS data. Many investigators report brain-plasma and CSF-plasma ratios. However, because drug entry into CNS may be delayed and the half-life of drug in CNS could differ significantly from that of blood, the drug brain-plasma or

87

CSF-plasma ratio could lead to erroneous conclusions. Exaggerated drug pharmacokinetics, typical of drug carrier systems, as well as the timing of specimen collection must be properly considered. Therefore a more appropriate parameter to measure in CNS studies is the absolute concentration of free drug relative to the therapeutic concentration.[39] In general, tools traditionally used to assess the ADME properties of NCEs have not been able to adequately describe nanotechnology drug-delivery systems. [40]

Increases in 6MPR and 6MP concentrations in the brain and CSF of rats immediately after the administration of 5 nm 6MPR-AuNPs is significant because of the potential implication on the delivery of important CNS drugs. Much like drugs which successfully cross the BBB, the brain uptake of 6-MPR-AuNPs raises the possibility that these particles have unique physicochemical properties that facilitate BBB penetration.

Table 3-2. 6-MPR and 6-MP mean (n = 3) plasma concentrations following intravenous injection of 5nm 6MPR-AuNPs (5 mg/kg active) to Sprague-Dawley rats.

Subject	Hours	Brain (ng/g)		CSF (ng/mL)		Plasma (ng/mL)	
		6MPR	6MP	6MPR	6MP	6MPR	6MP
Rat 7, 8, 9	0.083	499.5 ± 121	3870 ±1024	217.5 ±67	632 ±114	4760 ±874	2375 ±324
Rat 10,11,12	0.25	332 ± 91	1800 ±412	69.95 ±13	226.5 ±85	3710 ±684	996.5 ±144
Rat 13,14,15	0.50	131 ±34	505 ±132	13.49 ±87	104.5 ±41	2735 ±304	613.5 ±94
Rat 16,17,18	0.75	123.7 ±74	342.5±87	8.45 ±2	95.85 ±24	1081 ±128	418 ±124

Table 3-3. 6-MPR and 6-MP mean (n = 3) plasma concentrations following intravenous injection of 6-MPR (5 mg/kg) to Sprague-Dawley rats.

Subject	Hours	Brain (ng/g)		CSF (ng/mL)		Plasma (ng/mL)	
		6MPR	6MP	6MPR	6MP	6MPR	6MP
Rat 19,20,21	0.083	149 ±95	1950 ±758	47.4 ±24	249 ±87	47.7 ±14	168 ±80
Rat 22,23,24	0.25	105 ±83	593 ±169	34.4 ±14	157 ±86	24.8 ±8	24.4 ±11
Rat 25,26,27	0.50	47 ±31	222 ±91	15 ±9*	110 ±64*	12.8 ±6	26.8 ±13
Rat 28,29,30	0.75	49 ±39	191 ±89	8.87 ±6	99 ±47	10.9 ±5	5.15 ±2

* Sample deactivated due to blood contamination; values are interpolated based on noncompartmental analysis.
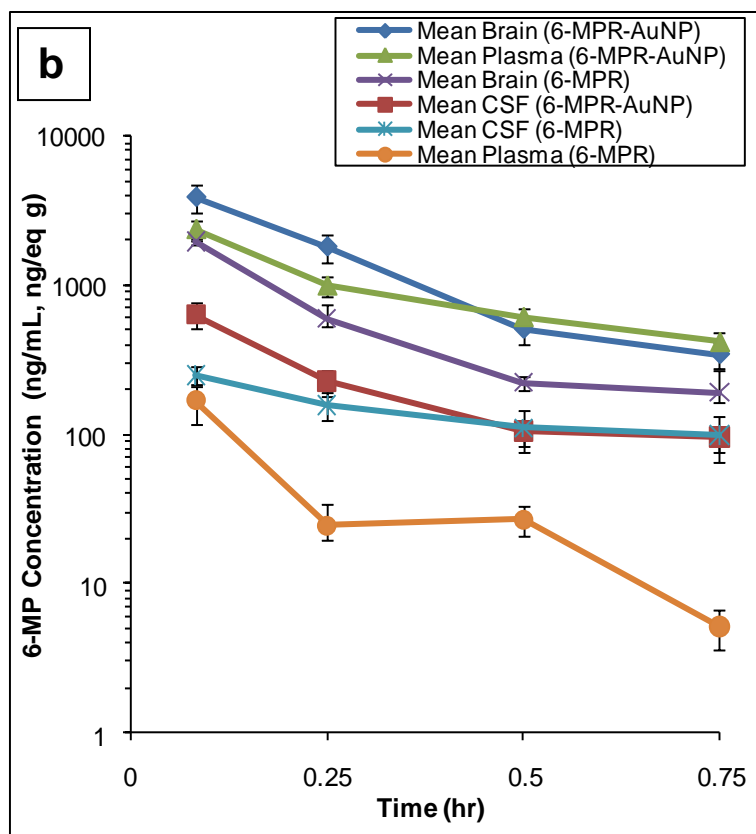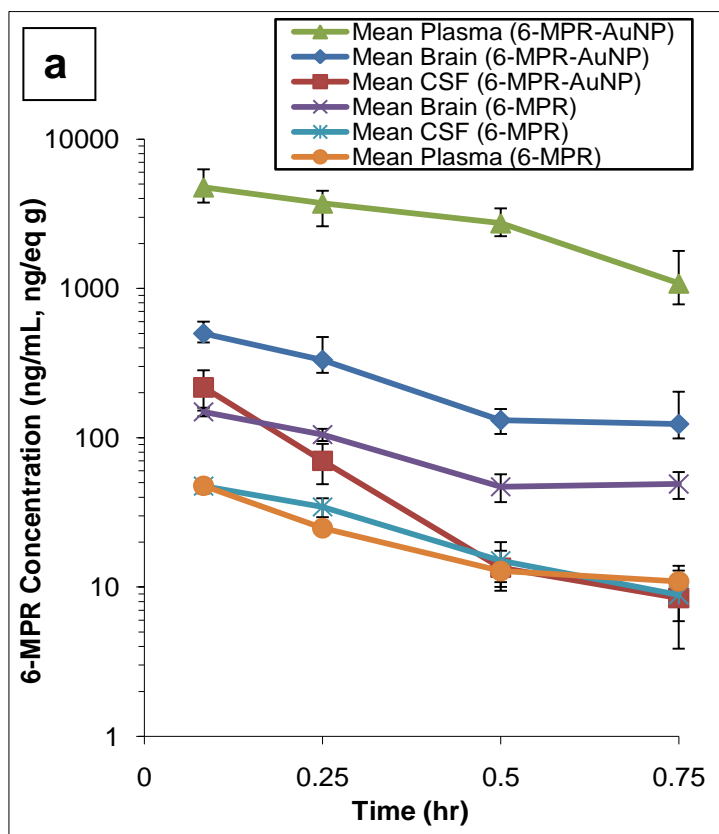
Figure 3-2-4. Mean brain, CSF and plasma concentration-time profiles of (a) 6-MPR (b) 6-MP in Sprague Dawley rats following single intravenous administration (5 mg/kg 6-MPR) of 5 nm 6MPR-AuNPs or unconjugated 6-MPR. Each point and bar represents the mean (n = 3) ± S.D.

Table 3-4. Pharmacokinetic parameters of 6-MP and 6-MPR in brain, CSF and plasma of rats following intravenous administration (5 mg/kg 6-MPR) of 6MPR-AuNPs or 6-MPR. Each value represents the mean (n = 3) ± S.D.

Parameters	6MPR			6-MPR-AuNPs		
	Brain (ng/g)	CSF (ng/mL·h)	Plasma (ng/mL·h)	Brain (ng/g)	CSF (ng/mL·h)	Plasma (ng/mL·h)
AUC(6MPR) $_{0.083-0.75\ h}$	52 ± 9	16 ± 4	14 ± 7	159 ± 9	37 ± 7	1990 ± 23
C_0 (ng/mL)	192 ± 35	65 ± 15	55 ± 8	422 ± 17	248 ± 12	955 ± 15
$T_{1/2}$ (hours)	–	–	0.19 ± 0.10	–	–	0.71 ± 0.18
CL (mL/min/kg)	–	–	6076 ± 810	–	–	42 ± 19
V_{dss} (mL/kg)	–	–	7184 ± 305	–	–	87 ± 13
AUC(6MP) $_{0.083-0.75\ h}$	366 ± 18	93 ± 7	27 ± 4	868 ± 11	138 ± 16	612 ± 14
C_0 (ng/mL)	2151 ± 25	278 ± 27	178 ± 25	4599 ± 15	697 ± 12	2664 ± 75
$T_{1/2}$ (hours)	–	–	BLQ*	–	–	0.38 ± 0.05
CL (mL/min/kg)	–	–	BLQ*	–	–	136 ± 31
V_{dss} (mL/kg)	–	–	BLQ*	–	–	

*Value below 6.76ng/mL

"– ": Estimation of brain and CSF PK parameters is outside the scope of current experiments. Modeling experiments will be needed to determine these values

3.2.1.5   Brain, CSF, and Plasma TEM Imaging

TEM imaging was performed on brain, CSF and plasma samples to determine whether or not AuNPs were present in these tissues. Representative images of the dosing solution and biological samples are presented with accompanying scale bar markers (Figure 3-2-5a - 3-2-5h). Large numbers of particles were observed in brain, CSF and plasma samples, confirming the presence of AuNPs in the CNS. AuNPs can be seen in brain matrix at 5, 15, 30 and 45 minutes after injection of 6-MPR-AuNPs. In all cases, though to a lesser extent in plasma, the hydrodynamic size of the nanoparticles increased relative to the dosing solution.

Proteins present in blood, CSF and brain matrixes may have adsorbed onto the surfaces of AuNPs and altered the effective hydrodynamic size.[41] The extent of this effect is dependent on protein concentration and other thermodynamic factors.[42] It was also observed that the

number of particles in brain significantly decreased within forty-five minutes, indicating lack of

persistence of the AuNPs in the CNS. Translocation of nanoparticle via the lymphatic system

and microglia scavenger cells of the CNS has been previously reported.[43]

Ultra-thin sections of rat brain were examined by TEM to confirm that 6-MPR-AuNPs

indeed penetrated intact BBB and were distributed into cerebral parenchyma. 6-MPR-AuNPs

were not only found inside the cytoplasm of vascular endothelial cells and the foot processes of

astrocytes, but more importantly were also found inside the cylindraxile of neurons which are not

attached to cerebral vessels (Figure 3-2-6a - 3-2-6c). The presence of 6-MPR-AuNPs inside

neurons indicates that the nanoparticles diffused through the vascular endothelial cells and the

astrocytes at the BBB before reaching the neurons in the cerebral parenchyma. It is worth noting

here that the nanoparticles are diluted at least 200-fold after leaving the endothelial cells.[44]

The mechanism of transport of nanoparticle across the BBB has been proposed [45] to

involve one or a combination of the following events: (1) transcytosis of vascular endothelial

cells, (2) opening of tight junctions due to nanoparticle disruption of BBB, solubilization of

endothelial cell membrane, and (3) diffusion due to a high concentration gradient across the

endothelial cell layer due to retention of the nanoparticles in the brain capillaries. In this study,

TEM images (Figure 3-2-6) show that the integrity of tight junction and BBB function during

treatment with AuNPs were maintained. Membrane morphology, intracellular endocytic vesicles

and tight junctions all appear normal, demonstrating that AuNPs did not induce changes to the

endothelial cell membrane. In addition, AuNPs were also found within the cytoplasm of vascular

endothelial cells. The mechanism underlying the brain penetration by AuNPs is not fully

understood but the authors propose that transcytosis of vascular endothelial cells is the most

likely mechanism involved. Additional studies on the mechanism by which nanoparticles cross

the BBB are needed.
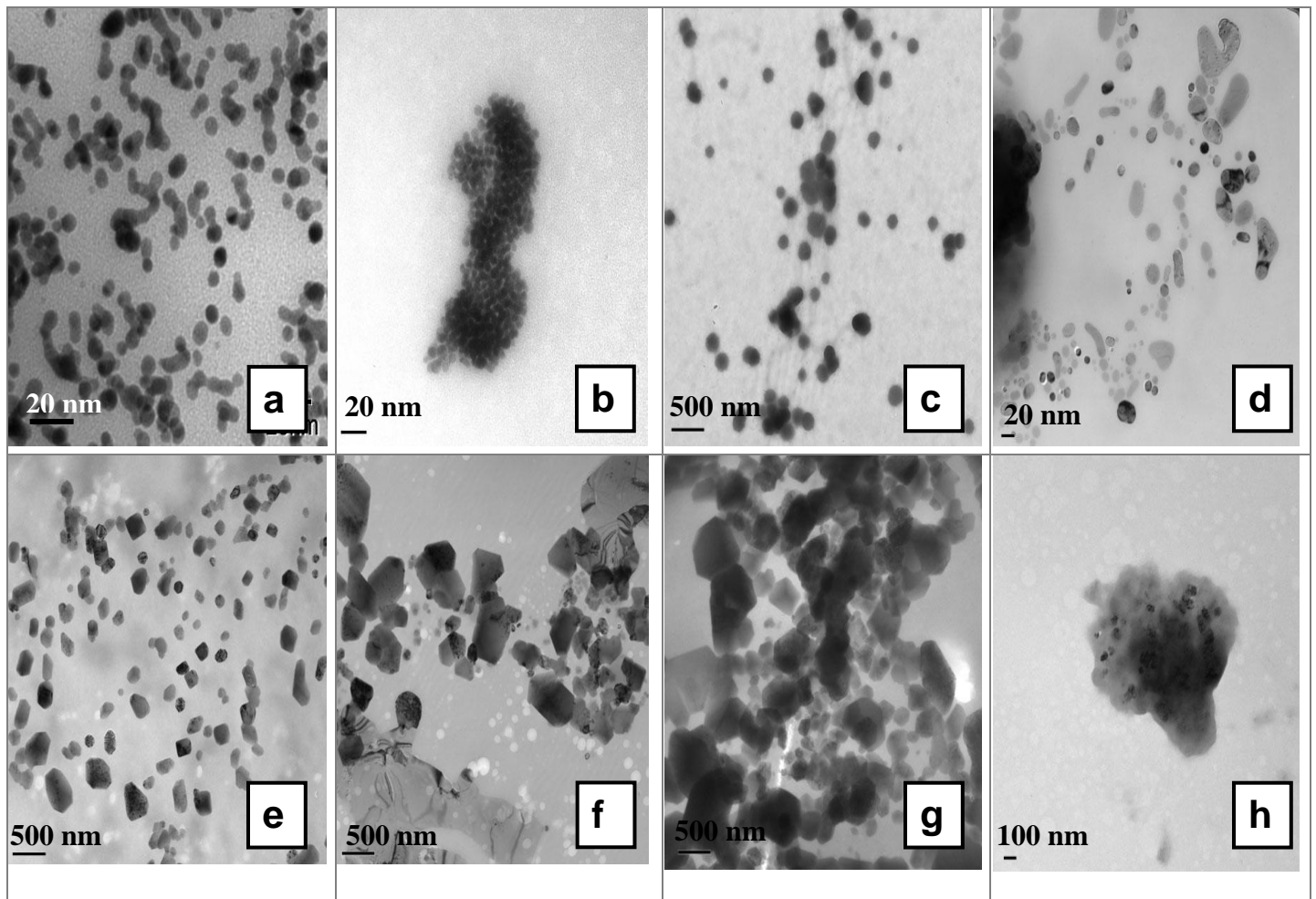
Figure 3-2-5. TEM images of AuNPs observed in (a) 5 nm 6MPR-AuNP dosing solution (control) (b) plasma (c) CSF (d) brain – 5 minutes (e) brain – 5 minutes (adjacent grid from (d)) (f) brain – 15 minutes (g) brain – 30 minutes (h) brain – 45 minutes, after intravenous injection of 5 nm 6MPR-AuNPs (5 mg/kg active). Images are representative of 20 different regions in each sample.
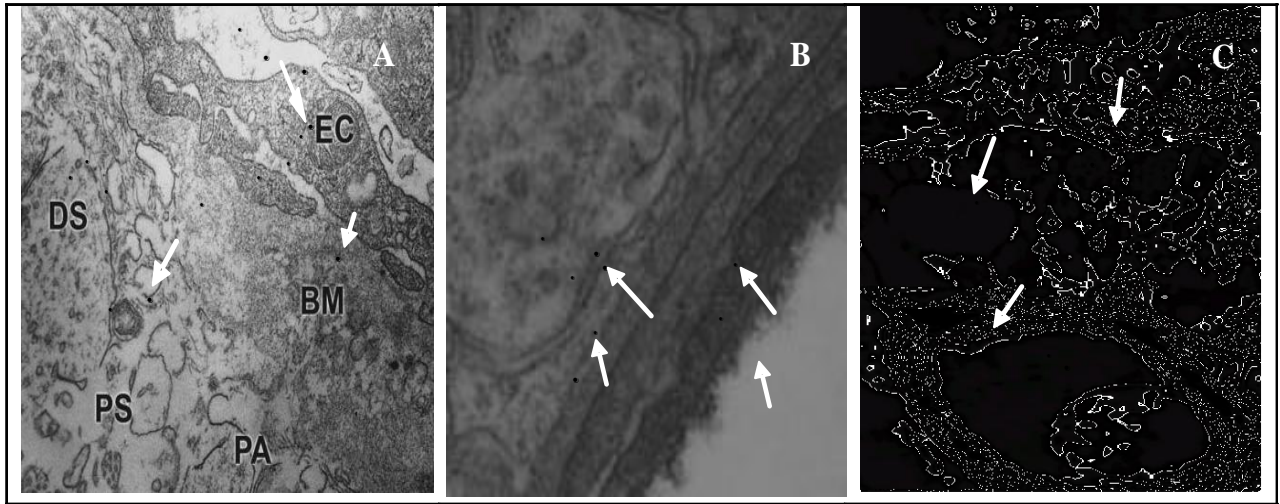
Figure 3-2-6. TEM images of brain sections sacrificed 15 minutes post-injection with 6-MPR-AuNPs. Nanoparticles are indicated by arrow. (**A**) Sagital section showing endothelial cell (EC), basement membrane (BM), astrocytic endfeet (PA) dissociated from the basement membrane, perivascular space (PS) and degenerate synaptic contact (DS). Gold nanoparticles are dispersed in vascular, endothelial and neuronal tissue, scale bar is 0.5 µm. (**B**) Partial magnification of endothelial cell membrane, membranes junction, cerebral vascular. Gold nanoparticles shown inside the cytoplasm of vascular endothelial cells and the foot processes of astrocytes scale bar is 0.3 µm. (**C**) Gold nanoparticles found inside the neurodendron and cylindraxile of neurons, scale bar is 0.3 µm.

3.3 CONCLUSIONS

Collectively, the results of this study provide direct evidence that 6-MPR-AuNPs penetrated the BBB and diffused into cerebral parenchyma and neuronal cells. In contrast, 6-MPR was not found in significant amounts in the brain and CSF. The mere presence of AuNPs in brain tissues, minutes after intravenous administration, is a significant finding and suggests that 5nm AuNPs potentially provide an effective carrier for diagnosis, imaging and treatment of CNS disorders. In addition, enabling brain uptake of 6-MPR has the potential of advancing novel therapeutic uses in the treatment of brain cancer and leukemic meningitis.

REFERENCES

1   Darling, J. Brain Tumor Invasion: Biological, Clinical, and Therapeutic Considerations, Brain 2000, 123(1), 189-190.
2   Deorah, S; Lynch C.F.; Sibenaller Z.A.; Ryken T.C. Trends in brain cancer incidence and survival in the United States: Surveillance, Epidemiology, and End Results Program, 1973 to 2001. Neurosurg Focus 2006, 20(4), E1.
3   Demuth T.; Berens M.E. Molecular mechanisms of glioma cell migration and invasion. Neurooncol. 2004, 70(2): 217–228.
4   Groothuis, D.R. The blood-brain and blood-tumor barriers: a review of strategies for increasing drug delivery. Neurooncol. 2000, 2(1), 45–59.
5   Mason, W.P.; Cairncross, J.G. Drug Insight: temozolomide as a treatment for malignant glioma — impact of a recent trial. Nat Clin Pract Neurol. 2005, 1(2), 88–95.
6   Medical Research Council Brain Tumor Working Party. Randomized trial of procarbazine, lomustine, and vincristine in the adjuvant treatment of high-grade astrocytoma: a Medical Research Council trial. J Clin Oncol. 2001, 19(2), 509–518.
7   Chang C.H. Horton J.; Schoenfeld D., et al. Comparison of postoperative radiotherapy and combined postoperative radiotherapy and chemotherapy in the multidisciplinary management of malignant gliomas. A joint Radiation Therapy Oncology Group and Eastern Cooperative Oncology Group study. Cancer 1983, 52(6), 997–1007.
8   Zunkeler B.; Carson R.E.; Olson J., et al. Quantification and pharmacokinetics of blood-brain barrier disruption in humans. J Neurosurg. 1996, 85(6), 1056–1065.
9   Fortin D. Desjardins A. Benko A.; Niyonsega T. Boudrias M. Enhanced chemotherapy delivery by intraarterial infusion and blood-brain barrier disruption in malignant brain tumors: the Sherbrooke experience. Cancer 2005, 103(12), 2606–2615.
10   Misra A.; Ganesh S.; Shahiwala A.; Shah S.P. Drug delivery to the central nervous system: a review. J Pharm Pharm Sci. 2003, 6(2), 252–273.
11   Vasir, J.; Reddy, M.; Labhasetwar, V. Nanosystems in Drug Targeting: Opportunities and Challenges Current Nanoscience 2005, 1, 47-64.
12   Jin, S.; Ye, K. Nanoparticle-Mediated Drug Delivery and Gene Therapy. Biotechnol. Prog. 2006, 23, 32–41.
13   Bansal, V.; Basu, A.; Bhonde, R. R.; Sastry, M.; Shakula, R. Biocompatability of Gold Nanoparticles and their Endocytotic Fate Inside the Cellular Compartment: A Microscopic Overview. Langmuir 2005, 21, 10644-10654.
14   Ghosh, P.; Han, G.; De, M.; Kim, C. K.; Rotello, V. M. Gold Nanoparticles in Delivery Applications. Adv Drug Del. Rev. 2008, 60, 1307-1315.
15   Han, G.; Ghosh, P.; Rotello, V. M. Functionalized Gold Nanoparticles for Drug Delivery. Nanomedicine 2007, 2, 113–123.
16   Paciotti, G.F.; Myer, L.; Weinreich, D.; Goia, D.; Pavel, N.; McLaughlin, R.E.; Tamarkin, L. Colloidal Gold: A Novel Nanoparticle Vector for TumorDirected Drug Delivery. Drug Deliver 2004, 11,169–183.
17   Peelle, B. R.; Krauland, E. M.; Wittrup, K. D.; Belcher, A. M. Design Criteria for Engineering Inorganic Material-Specific Peptides. Langmuir 2005, 21, 6929-6933.

18 Hillyer J.F.; Albrecht R.M. Gastrointestinal persorption and tissue distribution of differently sized colloidal gold nanoparticles. J Pharm Sci. 2001, 90, 1927-1936.

19 Hillyer, J.F.; Albrecht, R.M. Correlative instrumental neutron activation analysis, light microscopy, transmission electron microscopy, and Xray microanalysis for qualitative and quantitative detection of colloidal gold spheres in biological specimens. Microsc Microanal. 1999, 4, 481-490.

20 Albrecht R.M.; Simmons S.R.; Pawley J.B. Correlative video-enhanced light microscopy, high voltage transmission electron microscopy, and field emission scanning electron microscopy for the localization of colloidal gold labels. New York: Oxford University Press, 1993; 151–176.

21 Hainfeld, J.F.; Slatkin, D.N.; Focella, T.M.; Smilowitz, H.M. Gold nanoparticles: a new X-ray contrast agent. Brit. J. Radiol. 2006, 79, 248–253.

22 De Jong, W.H.; Hagens, W.I.; Krystek, P.; Burger, M.C.; Sips, A. Geertsma, R. Particle size-dependent organ distribution of gold nanoparticles after intravenous administration. Biomaterials 2008, 29, 1912-1919.

23 Siver Moestue, Paula Nunez, Andrew Healey, Roger Bjerke, Bård Indrevoll, Tore Skotland, Svein Olaf Hustvedt Whole-body section fluorescence imaging – a novel method for tissue distribution studies of fluorescent substances. Contrast media and molecular imaging 2009, 4(2),73–80

24 Leblond F.; Davis S.C.; Valdés P.A.; Pogue B.W.; Pre-clinical whole-body fluorescence imaging: Review of instruments, methods and applications. Photochem Photobiol B 2010, 2009, 98(1), 77-94.

25 Nelson, J.A.; Cserr, H.F.; Shih H. Chu, S.H. Distribution of 6-Mercaptopurine Ribonucleoside and Other Purine Analogs to Brain. Cancer Research 1974, 34, 1889-1891.

26 Shi, R.Z.; Lyons, S.D.; Christopherson, R.I. Metabolic effects of thiopurine derivatives against human CCRF-CEM leukaemia cells. Int J Biochem Cell Biol. 1998, 30, 885-895.

27 Burchenal J.H.; Murphy M.L.; Ellison R.R.; Sykes M.P.; Tan T.C.; Leone L.A.; Karnofsky D.A.; Craver L.F.; Dargeon H.W.; Rhoads C.P. Clinical evaluation of a new antimetabolite, 6-mercaptopurine in the treatment of leukemia and allied diseases. Blood 1953, 8, 965-999.

28 Mawatari, H.; Unei, K.; Nishimura, S.; Sakura, N.; Ueda, K. Comparative pharmacokinetics of oral 6-mercaptopurine and intravenous 6-mercaptopurine riboside in children. Pediatrics International 2001, 43, 673–677.

29 Bergmann, F.; Kwietny, H.; Levin, G.; Brown, D.J. The action of mammalian xanthine oxidase on N-methylated purines. J. Am. Chem. Soc. 1960, 82, 598-605.

30 Viudez, A.J.; Madueño, R.; Pineda, T.; Blazquez, M. Stabilization of gold nanoparticles by 6-mercaptopurine monolayers. Effects of the solvent. J Phys Chem B 2006, 36, 17840-17847.

31 Podsiadlo, P.; Sinani, V.A.; Bahng, J. H.; Shi Kam, N.W.; Lee, J.; Kotov, N.A. Gold Nanoparticles Enhance the Anti-Leukemia Action of a 6-Mercaptopurine Chemotherapeutic Agent. Langmuir 2008, 24, 568-574.

32 Sinani, V.A.; Podsiadlo, P.; Lee, J.; Kotov, N. A.; Kempa, K. Gold nanoparticles with stable yellow-green luminescence. Int. J. Nanotechnol. 2007, 4, 239-251.

33 Kadar, P., Wujik, C.E. Remediation of undesirable secondary interactions encountered in hydrophilic interaction chromatography during development of a quantitative LC-MS/MS assay for a dipeptidyl peptidase IV (DPP-IV) inhibitor in monkey serum. E. J. Chromatogr. B 2009, 877, 471-476.

34 Hoffmann, A.; Bredno, J.; Wendland, M.; Derugin, N.; Ohara, P.; Wintermark, M. High and Low Molecular Weight Fluorescein Isothiocyanate (FITC)-Dextrans to Assess Blood-Brain Barrier Disruption: Technical Considerations. Transl Stroke Res. 2011, 2(1), 106-11.

35 Lu W.; Schroit A.J.; Vascularization of melanoma by mobilization and remodeling of preexisting latent vessels to patency. Cancer Res. 2005, 65(3), 913-918.

36 Mellett, L.B. Physicochemical considerations and pharmacokinetic behavior in delivery of drugs to the central nervous system. Cancer Treat Rep. 1977, 61, 527-531.

37 Adamson, P.C.; Balis, F.M.; Arndt, C.A.; Holcenberg, J.S.; Narang, P.K.; Murphy, R.F.; Gillespie, A.J.; Poplack, D.G. Intrathecal 6-Mercaptopurine: Preclinical Pharmacology, Phase I/II Trial, and Pharmacokinetic Study, Cancer Research 1991, 51, 6079-6083.

38 Hamilton, L.; Elion, G.B. The fate of 6-mercaptopurine in man. Ann. N. Y. Acad. Sci. 1954, 60, 304−314.

39 Haas, D.; Stone, J.; Clough, L.; Johnson, B.; Spearman, P.; Harris, V. L.; Zhong, L.; Nicotera, J.; Johnson, R.H.; Raffanti, S.P.; Hoadland, V.; Ju, W.D. Steady-State Indinavir Pharmacokinetics in Cerebrospinal Fluid (CSF) and Plasma Determined by Ultra-Intensive CSF Sampling. The 35th Annual Meeting of the Infectious Diseases Society of America 1999.

40 Zolnik, B.S.; Sadrieh, N. Regulatory perspective on the importance of ADME assessment of nanoscale material containing drugs, Adv Drug Deliv Rev. 2009, 61, 422-427.

41 De Paoli Lacerda, S.H.; Park, J.J.; Meuse, C.; Pristinski, D.; Becker, M.L.; Karim, A.; Douglas, J.F. Interaction of Gold Nanoparticles with Common Human Blood Proteins.ACS Nano 2010, 4, 365–379.

42 Zhang, F.; Skoda, M.W.; Jacobs, R.M.; Zorn, S.; Martin, R.A.; Martin, C.; Clark, G.; Goerigk, G.; Schreiber, F. Gold nanoparticles decorated with oligo(ethylene glycol) thiols: protein resistance and colloidal stability. J Phys Chem A 2007, 111, 12229–12237.

43 Oberdorster, G.; Maynard, A.; Donaldson, K.; Castranova, V.; Fitzpatrick, J.; Ausman, K.; Carter, J.; Karn, B.; Kreyling, W.; Lai, D. Principles for characterizing the potential human health effects from exposure to nanomaterials: Elements of a screening strategy. Part. Fibre Toxicol. 2005, 2, 1–35.

44 Poduslo, J.F.; Curran, G.L. Permeability at the blood–brain and blood–nerve barriers of the neurotrophic factors: NGF, CNTF, NT-3, BDNF, Brain Research Molecular Brain Research 1996, 36, 280–286.

45   Kreuter, J. Nanoparticulate systems for brain delivery of drugs. Advanced Drug Delivery Reviews. 2001, 47, 65–81

CHAPTER 4

GOLD NANOPARTICLES ENHANCE BRAIN PENETRATION AND CENTRAL DOPAMINE RECEPTOR AFFINITY

4.0   INTRODUCTION

Dopamine is synthesized primarily in the central nervous system (CNS) and acts as a neurotransmitter in the brain. Limited production also occurs in the adrenal medulla and nonneuronal tissues, including the pancreas and the anterior pituitary.[1] The five subtypes of dopamine receptors (D1 through D5) are coexpressed at different levels in the CNS and peripheral tissues.

Dysfunction of dopaminergic systems is implicated in the development of defects in cognition, event prediction, emotion, behavior, addiction, attention deficits and schizophrenia.[2,3,4] Recent findings show that the D_2 and D_3 receptors specifically have a diverse role in the pathophysiology of schizophrenia, Parkinson's disease and drug abuse. For instance, deficiency of dopamine in midbrain nigrostriatal neurons has long been recognized in the pathogenesis of Parkinson's disease [5,6], while over-activity of the limbic and cortical dopaminergic neurons has been implicated in schizophrenia and psychoses.[7] In the neuroendocrine axis, dysfunction of hypothalamic dopamine or its pituitary receptors leads to hyperprolactinemia and reproductive disturbances.[8,9,] It is not surprising, therefore, that this

relatively simple molecule (Figure 4-1-1a) has been at the center of interest of basic scientists and clinicians alike for many years.

Dopamine (DA) does not effectively penetrate the blood brain barrier (BBB); thus the brain and central nervous system are dependent upon endogenous dopamine synthesis. [10] L-DOPA (Figure 4-1-1b) which is the precursor to catecholamines (neurotransmitters: dopamine, norepinephrine, and epinephrine) crosses the protective blood-brain barrier and since the 1960s has been used as the gold standard for treating Parkinson's disease. L-dopa crosses the BBB transported by LAT-1 (L or Large amino acid transporter). This transporter moves amino acids like phenylalanine and tyrosine across the BBB.[11] Once inside the central nervous system, L-DOPA is converted into dopamine by the enzyme DOPA decarboxylase (DDC). However, Levodopa-induced motor fluctuations and dyskinesias constitute a significant proportion of adverse effects seen with sole L-DOPA administration.[12] Besides the central nervous system, L-DOPA is also converted into dopamine from within the peripheral nervous system.

The BBB segregates the CNS from the systemic circulation, and its main physiological functions include maintaining homeostasis at the brain parenchyma and protecting the brain from potentially harmful chemicals.[13] The BBB expresses a number of specific carrier-mediated transporters that ensure an adequate nutrient supply for the brain.

The BBB is primarily formed from capillary endothelial cells, which differ from the other tissues. The brain capillary endothelial cells are very closely joined together by tight intercellular junctions that efficiently restrict the paracellular diffusion of drugs.[14] The high metabolic activity of brain capillary endothelial cells, as well as effective efflux systems that actively remove solutes from brain tissue and return them back to the bloodstream, create additional challenges for potential CNS drugs.[15]

Measurement of total drug concentration within the brain is relatively simple to obtain. However it is difficult to correlate this information with CNS effect. Therefore, a more reliable parameter for establishing CNS efficacy of a therapeutic agent is the percent receptor occupancy (RO) of the molecular target, which can be determined from receptor binding studies.[16] This technique involves measuring the displacement (or receptor occupancy) of radioligand by the competing agent, coupled with liquid-scintillation counting and autoradiography. RO data generated this way has provided deep understanding of the involvement of neurotransmitters during the development of neurological disorders such as Parkinson's disease, schizophrenia and depression. [17] These methods however are not without limitations. Suitable radioligands for such a technique (i.e., with adequate specific binding) are not always available for every drug target [18] and may require extensive validation prior to experimentation.[19] The radioligand may also have its own side effects, and being radioactive poses significant safety risks. Therefore, a more rapid and cost-effective imaging ligand for determining receptor occupancy would also be of immense value. We propose that gold nanoparticles could provide a more potent, safer and more cost-effective alternative to current radioligands for preclinical and clinical imaging applications.

Gold nanoparticles have attracted considerable attention in medical research because they are intrinsically biocompatible, have minimal toxicity, are easy to synthesize, and functionalize for specific targeting.[20, 21,22] Also the luminescence of gold and high electron density allow it to be used as a diagnostic and imaging tool for applications, such as spectrophotometry, fluorescence microscopy, computer tomography (CT), and transmission electron microscopy (TEM).[23,24, 25] More significantly, several studies (including our own) have reported the penetration of rat brain by small gold nanoparticles (AuNPs) with diameter cut-off of 50 nm, following intravenous administration.[26,27]

In the present study, we used receptor binding experiments to confirm the potential use of novel 5nm dopamine-AuNPs (Figure 4-1-1c) to overcome the low BBB permeability of dopamine, while enhancing binding affinity and specificity (and therefore pharmacological properties) at dopaminergic receptors. Also, AuNPs may provide a more potent, safer and more cost-effective alternative to current radioligands. To date no studies have used dopamine-AuNPs to cross the BBB, and bind to dopamine target.
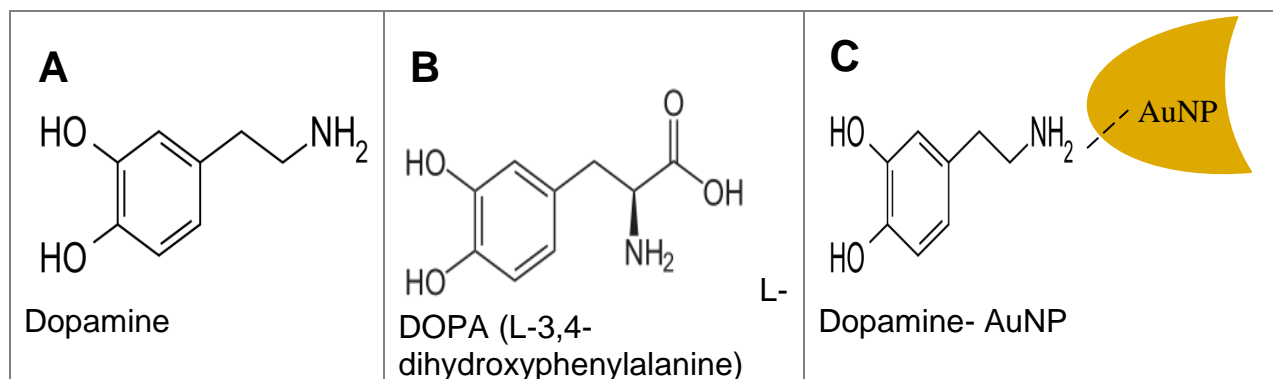
Figure 4-1-1. Chemical structure of (A) Dopamine (B) L-3,4-dihydroxyphenylalanine (L-DOPA) (C) Schematic representation of Dopamine-AuNP. L-DOPA crosses the blood brain barrier and is a precursor Dopamine which does not cross the blood brain barrier.

4.1   METHODS

4.1.1   Materials

Hydrogen tetrachloroaurate ($HAuCl_4 \cdot 4H_2O$) and sodium citrate ($C_6H_5Na_3O_7 \cdot 2H_2O$) were purchased from Sigma Aldridge, USA. Solvents, nitric acid (HNO_3), hydrochloric acid (HCl) and sodium alginate were also purchased from *VWR* International. Deionised water (H_2O) was purified by a Millipore system (Milli-Q). All other chemicals and solvents were of reagent grade. All these chemicals were used without purification.

Fetal calf serum was obtained from PAA Laboratories. EDTA, EGTA, Tris-HCl buffer, NaCl, KCl, CaCl2, MgCl2, NaH2PO4, KH2PO4, D-glucose, and *N*-methyl-D-glucamine (NMDG) were obtained from Sigma-Aldrich. PBS and Hepes were obtained from Invitrogen Life sciences. Complete protease inhibitor cocktail tablets were obtained from Roche Diagnostics. Dopamine was purchased from US Pharmacopeia (Rockville, MD). 81.4 *Ci/mmol* [3H]dopamine ([3H]DA) *and* 29.2 Ci/mmol GBR12783 were purchased from Amersham, Les Ulis, France. The reference drugs were stored in a 1mM solution at -20 °C and diluted to the required concentration on ice, immediately before binding assays. All Chemicals used were of chemical grade.

4.1.2   Animals

All animal experiments were conducted according to procedures approved by the Pfizer Global Research and Development Animal Care and Use Committee and complied with the NIH guidelines for the Care and Use of Laboratory Animals. Male Sprague-Dawley rats were purchased from Charles River Laboratories (Willmington, MA). The rats were housed one per cage under reversed light/dark conditions using a 12 hour on/off schedule. Room temperature

was maintained at 21 ± 1°C with a relative humidity of 55 to 60%. Food and water were available ad libitum. The animals were allowed 1 week of adaptation to laboratory conditions before being used in experiments.

4.1.3   Preparation of DA-AuNPs

DA-AuNPs of average particle sizes 15, 50, 100 and 200 nm were synthesized using a method pioneered by Turkevich,[28,29] with certain variation. The method involved reducing hydrogen tetrachloroaurate with sodium citrate in the presence of dopamine. Briefly, hydrogen tetrachloroaurate was weighed accurately (10 mg) and dissolved in 2 mL of purified water. Sodium citrate (400mg) weighed and dissolved in 10 mL of purified water. Hydrogen tetrachloroaurate solution was then added to 48 mL of the purified water which was subsequently added in three neck round bottom flask attached further to reflux condenser. The solution was heated to 100∘C and the required quantity of the sodium citrate solution (1.54×10^{-2} M for 15 nm, 1.74×10^{-3} M for 50 nm, 1.41×10^{-3} M for 100 nm and 1.15×10^{-3} for 200 nm) was added. The color change of hydrogen tetrachloroaurate solution following addition of sodium citrate solution was noticed. The solution was heated for 10 minutes and the resulting nanoparticulate suspension was allowed to cool at room temperature.

To prepare DA-AuNPs, 40 mL aqueous solution containing 12.5mg of dopamine was brought into contact with gold sol using a process developed in our laboratory (Figure 4-1-2). The two solutions were fed via peristaltic pumps at 1 mL/min and are subsequently combined in a single tube which is either diverted to a recirculation loop controlled by valve 3, or collected at the outlet (valve 4). The reaction mixture was recirculated until the measured free drug concentration achieves steady state. The resulting gold nanoparticles were centrifuged (40,000

rpm for 30min) and washed three times with millipore® water. The gold nanoparticles were finally suspended in 0.5% (w/v) sodium alginate solution as a suspending agent. Sodium alginate solution was filtered through 0.22 um millipore® filter prior to use to ensure sterility. The 5nm DA-AuNPs were prepared as previously described; we however substitute 6-MPR with dopamine.[30]

AuNP solution

Dopamine solution

v1

pump

v2

pump

v3

v4

DA-AuNP solution
(Pre-purification)

v1: inlet valve 1
v2: inlet valve 2
v3: recirculation valve
v4: discharge valve
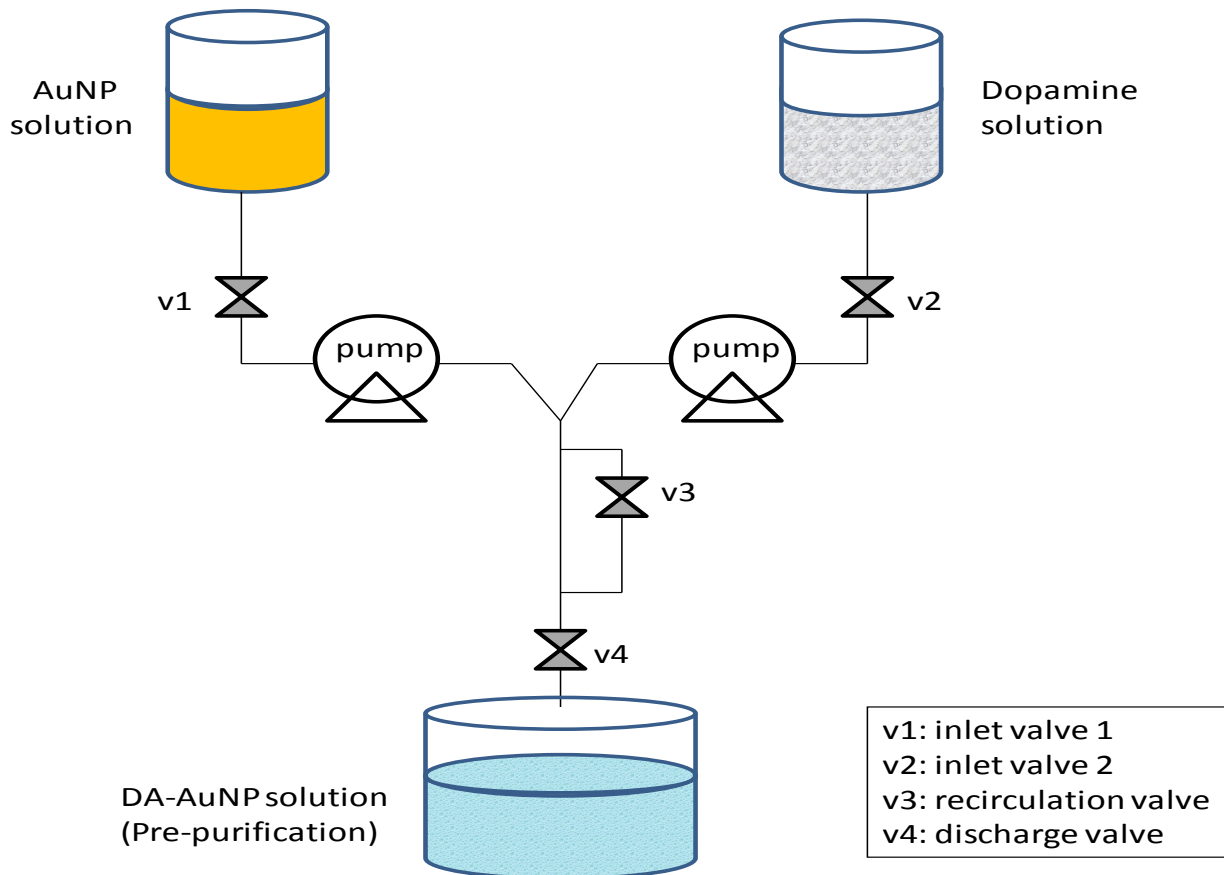
Figure 4-1-2. Process for preparing AuNP with high dopamine loading on the surface. Dopamine is brought into repeated contact with gold solution. Feed solutions are fed via peristaltic pumps and recirculation loop (valve 3). The process ensures maximum contact between dopamine and nanoparticles solutions, thereby resulting in high dopamine loading on the surface of the AuNPs.

4.1.4 Characterization of gold nanoparticles

The particle size and morphology of the 5, 15, 50, 100 and 200 nm DA-AuNP solutions were examined by transmission electron microscope (FEI Tecnai, G2 Sphera). Imaging was performed at 100,000 times magnification. Mean surface area and diameter of the particles were then determined using Image-Pro Plus software (Media Cybernetics). To prepare samples for TEM, 2-5 µL aliquots of the sample were placed onto carbon-coated formvar covered support grids and air-dried overnight in a protective environment. Representative images from samples at 100,000x were used to acquire sufficient (greater than 100) nanoparticle objects for image analysis. Images were processed to optimize particle segmentation. Statistics and frequency histograms were generated. The zeta potential of DA-AuNP was measured using Zetasizer Nano ZS, Malvern Instruments. Finally, High Pressure Liquid Chromatography (Agilent HPLC System) was used to determine the concentration of dopamine bound to the surface of AuNPs by digesting the gold colloids with potassium cyanide. Gold nanoparticles was resuspended in phosphate buffer (pH: 7.4, 0.154M) and the zeta potential was measured at 37°C.

4.1.5 Human whole-cell dopamine receptor binding

4.1.5.1 CHO-D2S cell growth and membrane preparation

Chinese hamster ovary (CHO) cell line expressing the short isoform of the human D2 dopamine receptor (CHO-D2S) cells were grown as monolayers in RPMI medium supplemented with 2 mM glutamine, 200 mg/mL active Geneticin, and 5% heat-inactivated fetal calf serum at 37°C in a moist, 5% CO2 atmosphere. When confluency was reached, cells were washed with 5mL of ice-cold buffer **A** (20 mM HEPES, 1mM EDTA (free acid) 1 mM EGTA, pH 7.4, with

KOH), removed from the flask by gentle shaking with 2mm diameter glass beads in 5 mL of buffer A, and homogenized with 30 strokes of a ThermoFisher Scientific Dounce homogenizer. The homogenate was centrifuged at 260 rpm, $3g$ for 10 minutes and the resulting supernatant centrifuged at 48000 rpm, $3g$ for 1 hour at 4°C. The membrane pellet was resuspended in ice-cold buffer A to achieve a final protein concentration of 5–10 mg/mL (Bradford protein determination; Bio-Rad Laboratories, Inc.). Aliquots were stored at -70 °C.

4.1.5.2 Competitive binding

Binding experiments were performed by incubating 0.5mL aliquots of the membrane preparation containing 3 –15 mg of protein per tube, with [3H]-DA (81.4 Ci/mmol) in 0.2 mL of buffer at 37°C for 90 minutes. After incubation with the radioligand, 10^{-3}–10^3 M of dopamine (with or without selective dopamine inhibitor, GBR12783) and DA-AuNP (with or without GBR12783) were added. 250μl of AuNPs alone or mixed with dopamine, or with membrane suspension were used as controls. Each experiment was performed in triplicate and incubated at 25 °C for 7 hours, by which time all binding ligands had reached equilibrium.

Experiments were terminated by separation of bound and free radioligand by rapid filtration through Whatman GF/C glass fiber filters pretreated with 0.2% poly-L-lysine, using a BrandelM-24R cell harvester followed with four washes of 3 mL of ice-cold phosphate-buffered saline (140 mM NaCl, 10mM KCl, 1.5 mM KH2PO4, 8 mM Na2HPO4). Filter discs were soaked in 2 mL each of Optiphase Hi-Safe 3 (Wallac) for at least 6 hour, 2.5 mL Perkin Elmer Ultima Gold Scintillation cocktail was added and the total radioactivity was determined by a liquid-scintillation counting system (LS5000 CE; Beckman Coulter, Fullerton, CA).

4.1.5.3 [3H]-Dopamine Autoradiography

After experiments were terminated, tissues were mounted onto silane-coated microscope slides and allowed to dry at room temperature. The slides were then placed in the chamber of the Beta-Imager 2000 instrument (BioSpace Lab, Cambridge, MA) and data were collected from the brain sections for 12 hours. The levels of bound radioactivity in striatum (cpm/mm2) were directly determined by counting the number of beta-particles emerging from the delineated area using the image analysis software, BetaVision (BioSpace Lab, Cambridge, MA).

4.1.5.4 Data Analysis

Data from binding experiments were analyzed using nonlinear least-squares curve-fitting method (Prism 5.01, GraphPad Software Inc, San Diego, CA). Bound [3H]-DA was calculated using the method of Golds *et al* [31], to correct for radioligand depletion. Bound radioligand concentration was taken as total-bound minus free concentration in the absence of competitor. Data were fitted to four-parameter logistic equations, and the best fit between a variable Hill coefficient and a Hill coefficient fixed to unity was determined using an F-test. The statistical significance of differences between data was determined at the 0.05 level, using ANOVA or Student's *t* test, as appropriate. At $p < 0.05$, statistical significance was considered to be achieved.

4.1.6 *Ex vivo* dopamine receptor binding

4.1.6.1 Animal dosing

Twenty-seven Sprague-Dawley rats weighing 280 to 320 g were used in these studies. Due to lack of brain penetration of dopamine, all test articles were injected directly into the cerebral parenchyma. Each group (n=4 rats per group) received 8 mg/kg intracerebral injections

of cold dopamine (with or without the selective dopamine inhibitor GBR12783), dopamine-AuNPs (with or without GBR12783). AuNP solution mixed with dopamine, or mixed with brain matrix served as control. Increasing concentrations of dopamine (ranging from $0 – 1.3uM$) were evaluated. Representative flow diagram of receptor occupancy protocol is shown in Figure 4-1-3.

Rats were anesthetized 50 minutes after administration. Anesthesia was induced with 5% isoflurane in an induction box and maintained with 2% isoflurane administered in a 50:50 air-oxygen mixture. A total of 120ug of atropine was administered intraperitoneally immediately after induction. Blood oxygen saturation and heart rate were monitored throughout the procedure (pulseoximeter; Nellcor), and temperature was maintained at 37°C using a locally manufactured rectal temperature–regulated heating pad and heating lamp. Rats were then decapitated and striatal tissues were excised, pooled, and stored at 70°C until used. For each rat, one striatum was used for binding assays, and the contralateral striatum was used for autoradiography. The striatum side (left and right) used for the binding assays was counterbalanced from one rat to the other.

4.1.6.2 Tissue preparation

Briefly, the tissues were thawed and homogenized in a glass Teflon homogenizer at 500 rpm in ice-cold 50 mM Tris-HCL buffer pH 7.4 for 20 minutes. The homogenates were centrifuged at 20,000 g for 20 mins at 5°C. The resultant pellets were rehomogenized in the same buffer and centrifuged again. The supernatant was discarded and the final pellets were resuspended in 5 to 10 mL assay buffer (50 mM Tris preset, 120 mM NaC1,5 mM KCI, 2 mMCaCl2 and 1mM MgCl2). The protein concentration of homogenate was determined by the methods of Lowry and Bradford. [32] The samples were stored at approximately -80°C until used.

4.1.6.3 Competitive binding

The assays were performed as described previously.[33] Briefly, striatal membranes (50ug protein per well) were incubated with [3H]-DA (56 - 62 mCi/mmol specific activity) in assay buffer (50 mM Tris preset, 120 mM NaCl, 5 mM KCl, 1 mM MgCl2, 2 mM CaCl2, pH 7.4). Incubation was for 45 minutes at 37°C. All assays were performed in duplicates. The reaction was terminated by rapid filtration through GF/B filter mats presoaked in 0.3% polyethyleneimine, followed by three 1mL washes with ice-cold 50 mM Tris –HCl buffer (pH 7.4). Filters and incubates were dissolved in 4 mL of scintillant (Ready Solve; Beckman Coulter) at room temperature. Radioactivity binding was determined by a liquid-scintillation counting system (LS5000 CE; Beckman Coulter, Fullerton, CA).

4.1.6.4 Autoradiography

Slide-mounted sections were allowed to equilibrate to room temperature for approximately one hour and encircled using a PAP Pen (Dako Denmark A/S, Glostrup, Denmark). Assay solutions were removed by aspiration. Slides were dipped briefly in ice-cold distilled water to remove buffer salts and allowed to dry at room temperature. The slides were then placed in the chamber of the Beta-Imager 2000 instrument (BioSpace Lab, Cambridge, MA) and data were collected. The levels of bound radioactivity in striatum (cpm/mm2) were directly determined by counting the number of β-particles emerging from the delineated area using the image analysis software, BetaVision (BioSpace Lab, Cambridge, MA).

4.1.6.5 Data analysis

Nonlinear least-squares fitting of the data were performed using GraphPad Prism 5.01 (GraphPad Inc, San Diego CA) data analysis software. Competition data was fitted to four-parameter logistic equations, and the best fit between a variable Hill coefficient and a Hill coefficient fixed to unity was determined using an F-test. The ratio of counts per milligram of tissue in the striatum provided a measure of the total number of binding sites (specific and nonspecific) for [3H]-DA. The ratio of counts per milligram of tissue, after rat exposure to GBR 1278, is used to define specific binding and correct data. Percent dopamine receptor occupancy (D2/D3-RO) in treated samples was calculated as (binding in treatment group – binding in vehicle group) /(binding in vehicle group). The percentage of [3H]-DA remaining in the presence of the test articles was plotted against the concentrations of dopamine or AuNPs. The statistical significance of differences between data was determined at the 0.05 level, using ANOVA or Student's t test, as appropriate. When, $p<0.05$, statistical significance was considered to be achieved.

4.1.7   In vivo dopamine receptor binding

4.1.7.1 Animal dosing

Twenty-four (n=4 per group) Sprague-Dawley rats weighing 280 to 320 grams were used in these studies. Due to lack of brain penetration of dopamine, and AuNPs with article size greater than 5 nm, all articles were injection directly into the cerebral parenchyma. Each group received 8 mg/kg injection of 5, 15, 50, 100, 200 nm DA-AuNPs, and the dopamine inhibitor GBR12783. One group of rats received an intravenous injection of DA-AuNPs in order to

confirm BBB penetration. A representative flow diagram of receptor occupancy protocol is shown in Figure 4-1-3.

4.1.7.2   Competitive binding and Tissue preparation

Fifteen minutes after receiving test articles, each rat received 8.0 µL of [3H]-DA (56–62 mCi/mmol specific activity) intracerebrally. The concentration of the [3H]-DA solution was 0.9 µCi/µL, equivalent to 3µg /µL. Rats were anesthetized, decapitated and the brains were removed immediately from the skull. The brain for autoradiographic imaging was placed into a brain mold with the region of interest uppermost. This was covered thoroughly with Tissue-Tek (Sakura Finetek Europe, Zoeterwoude, The Netherlands) and flash frozen in isopentane (cooled to between -20°C and -30°C with dry ice).

Tissues were processed as previously published.[34] Briefly, sagittal sections containing striata 1–1.7 mm from bregma, were cut with a VT1000S vibratome (Leica, Nussloch, Germany), thaw-mounted onto silane-coated microscope slides and stored in bubbled artificial CSF (ACSF) with kynurenic acid (1 uM) for 30 minutes. Six adjacent brain slices from the same animal were collected per microscope slide. Sections were encircled using a PAP Pen (Dako Denmark A/S, Glostrup, Denmark). All the sections were then washed twice for 2 minutes, each with 200 uL of ice-cold buffer (3 mm $MgCl_2$, 1 mm KH_2PO_4, pH 6.8). Slides were then dipped briefly in ice-cold distilled water to remove buffer salts and allowed to dry at room temperature.

4.1.7.3   Autoradiographic imaging

The slides were then placed in the chamber of the Beta-Imager 2000 instrument (BioSpace Lab, Cambridge, MA), and data were collected from the brain sections for 12 hours.

The levels of bound radioactivity in striatum (cpm/mm^2) were directly determined by counting the number of beta-particles emerging from the delineated area using the image analysis software, BetaVision (BioSpace Lab, Cambridge, MA). The ratio of counts per milligram of tissue in the striatum provided a measure of the total number of binding sites (specific and nonspecific) for [3H]-DA. The ratio of counts per milligram of tissue after rat exposure to GBR1278, is used to define specific binding and correct the data. Percent dopamine receptor occupancy (D2-RO) in treated samples was calculated.

4.1.7.4 TEM imaging of rat brain striata

Striata specimens of the rats injected intravenously with 5nm DA-AuNPs were fixed in chilled glutaraldehyde and then embedded in sample block. 60-80 nm thin sections are cut on ultramicrotome using a diamond knife. Sections are then air-dried for several hours overnight in a protective environment and placed onto carbon-coated formvar-covered support grids. The specimen was examined under a transmission electron microscope (FEI Tecnai, G2 Sphera) at 10,000 – 200,000 times magnification using accelerating voltages between 50kV and 120kV.
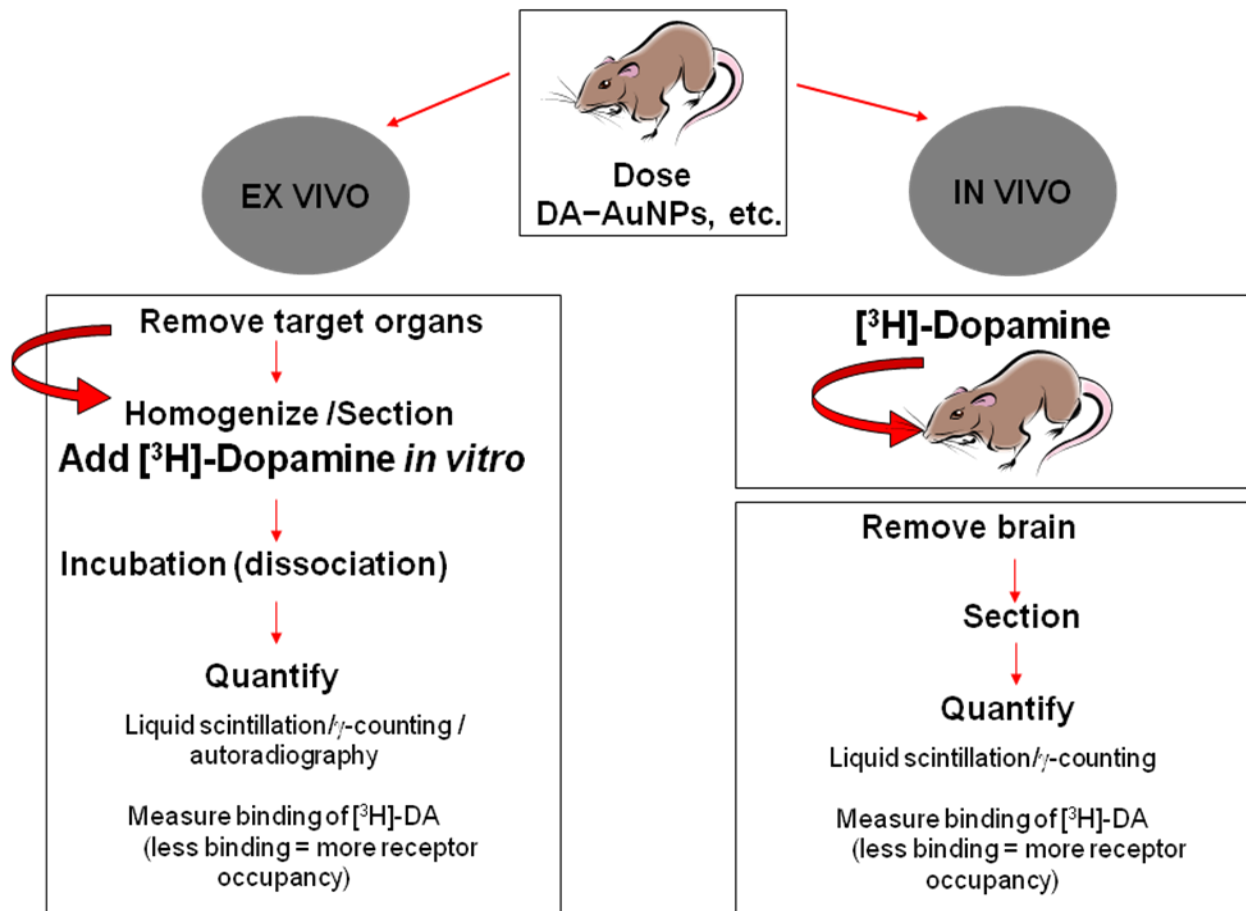
Figure 4-1-3. Flow diagram of *ex vivo* and *in vivo* receptor occupancy protocol. Diagram shows the differences between *ex vivo* and *in vivo* procedure.

4.2 RESULTS AND DISCUSSION

4.2.1 DA-AuNP synthesis and characterization

We developed a robust process (figures 2) to prepare DA-AuNPs with particle sizes from 5 to 200 nm (Figure 4-2-1). Efficient mixing and repeated recirculation of NP and drug solutions ensured maximum loading of dopamine unto AuNPs. The reaction was terminated after 2.5 hours when free drug concentration determined by HPLC achieved steady-state (Figure 4-1-2). A gradual change in the color of the effluent solution from intense red to a consistent dark purple after 4 hours of operation, provided visual confirmation of HPLC results.

During the chemical synthesis of gold NPs by citrate reduction of auric acid, NP size and stability were controlled by the negatively charged citrate ions at the freshly formed NP surface. The charge helps quench NP growth and accounts for the negative zeta potential of AuNPs.[35] Generally NPs with zeta potential above ±30mV prevents aggregation of the particles and result in stable suspensions.[36] In our experiment, the size of the NPs decreased from 200 to 15 nm as the ratio of citrate to chloroauric acid increased. Correspondingly, the zeta potential increased from -29 to -36 mV suggesting that citrate molecules actively bind to the Au surface.

Subsequent addition of dopamine to the citrate stabilized NPs changed the zeta potential from negative to positive (+7.9 to +9.6). This change of surface charge occurs due to displacement of citrate ions and association of dopamine ligands to the gold surface. Strong interaction between $Au(3+)$ and the lone electron pair on the nitrogen atom of the amine group, is likely responsible for long term stabilization of dopamine NPs.[37, 38] Table 4-1 summarizes the properties of AuNPs.
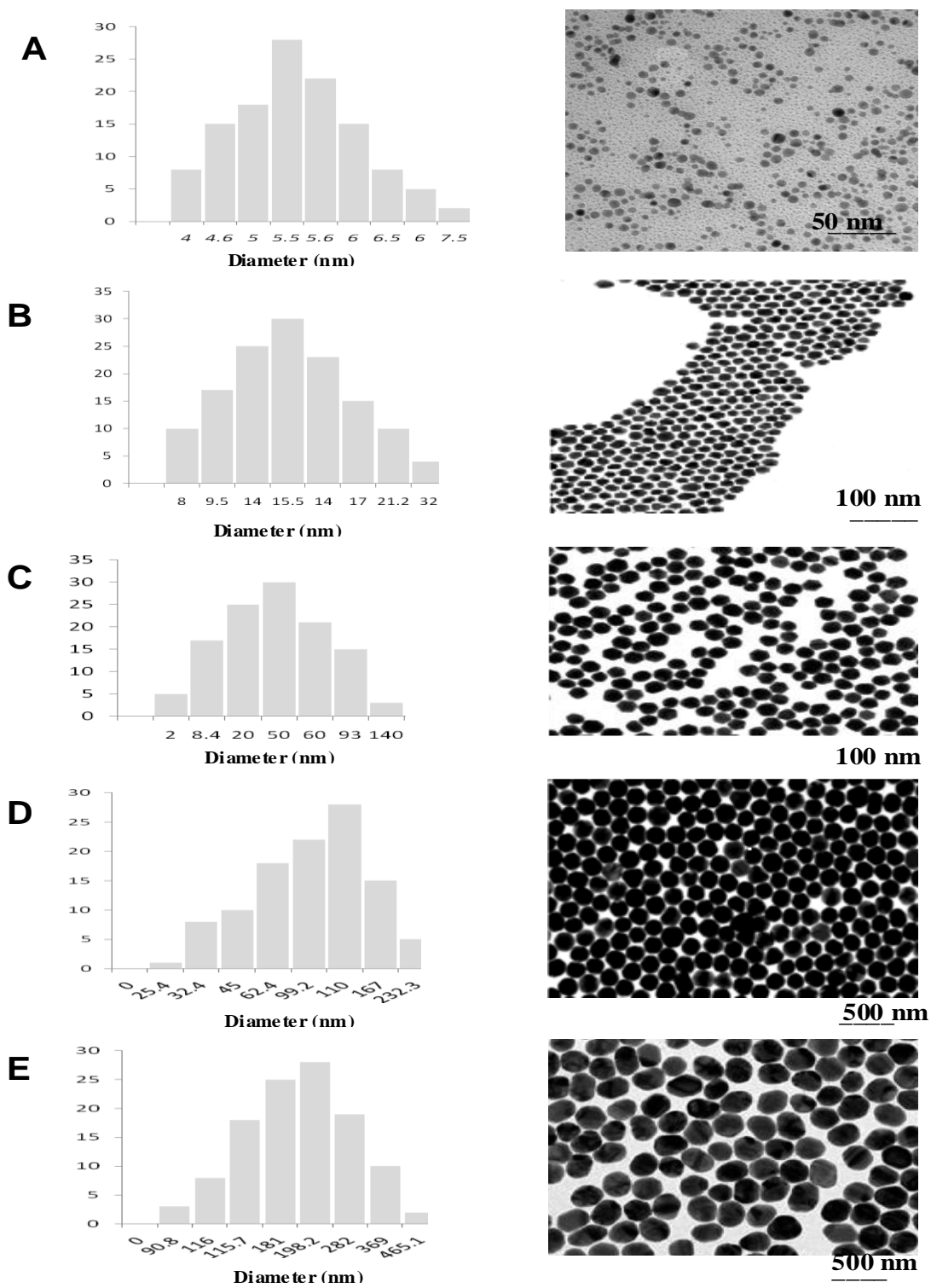
Figure 4-2-1. Particle size histogram(Left) and Transmission electront micrograph(Right) of DA-AuNPs 5 nm (A), 15nm (B), 50nm (C), 100nm (D), 200nm (E).
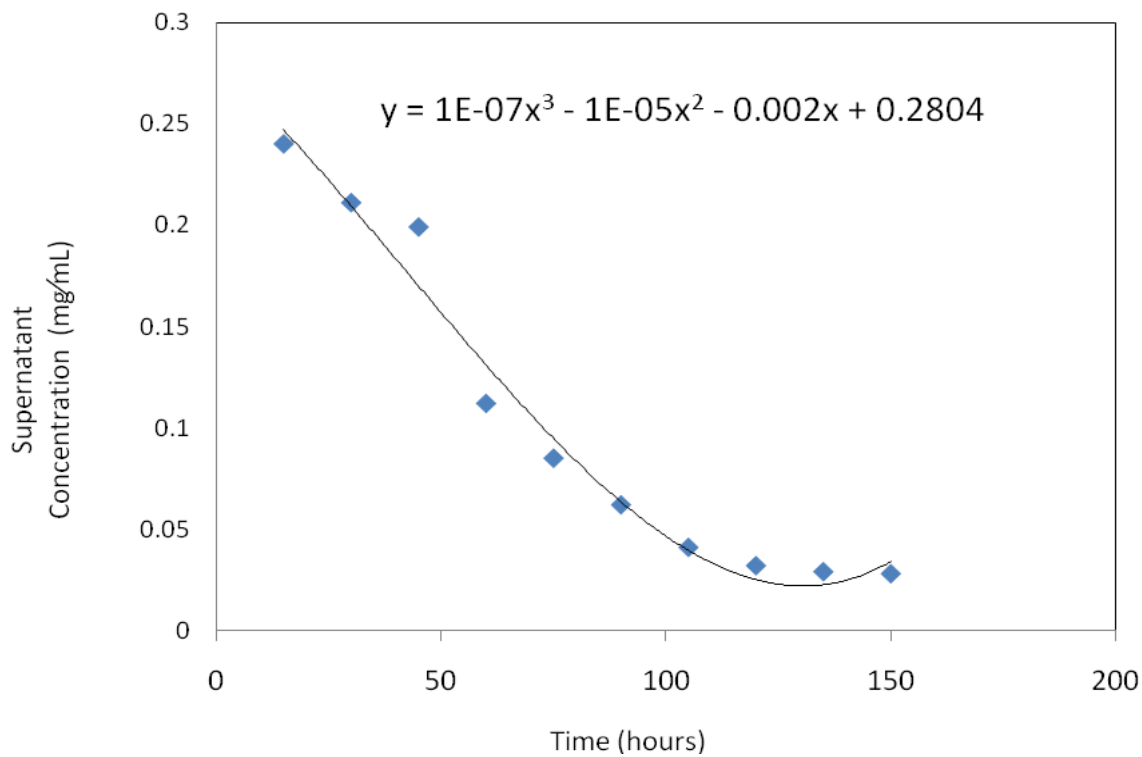
Figure 4-2-2. Reaction solution dopamine concentration-time curve. Free dopamine in solution decreases as dopamine is bound to the surface of AuNPs.

Table 4-1. Characterization of 5, 15, 50, 100 and 200nm DA-AuNPs.

Particle size (nm)	5 ± 1.30	15 ± 2.30	50 ± 5.65	100 ± 5.56	200 ± 7.56
Sodium citrate (mM)	1.51	15.4	1.74	1.41	1.15
Polydispersity Index	0.27 ± 0.05	0.24 ± 0.05	0.19 ± 0.08	0.31 ± 0.07	0.20 ± 0.06
Zeta potential (mV) (Citrate-AuNP)	-29.3 ± 0.91	-32.1 ± 1.07	-33.2 ± 0.71	-35.3 ± 1.01	-36.4 ± 1.21
Zeta potential (mV) (Dopamine-AuNP)	+7.9 ± 0.91	+8.3 ± 1.07	+8.8 ± 0.71	+9.4 ± 1.01	+9.6 ± 1.21

4.2.2 Human whole-cell dopamine receptor binding

Chinese hamster ovary (CHO) cell lines expressing the short isoform of the human D2 dopamine receptor (CHO-D2S) cells were used for competition binding experiments. The binding curves are presented in Figure 4-2-3, and showed dose-dependent binding of DA-AuNPs to D2 receptors. The radioligand (3H-DA) was displaced from receptors in the presence of a cold DA-AuNP challenge. The affinity of DA-AuNPs for human D2 receptor (D2R) was found to be 10-fold greater than free dopamine. 3H-DA binding decreased dramatically as the concentration of dopamine increased confirming that DA-AuNPs have greater affinity for D2R than dopamine alone. Furthermore, in the presence of dopamine inhibitor (GBR 12783) the binding of DA-AuNPs decreased to levels similar to those observed with free dopamine incubated with GBR12783. This provides direct evidence that the dopamine receptor is responsible for the binding with DA-AuNPs. GBR 12783 1-[2-(diphenylmethoxy) ethyl] 4-(3-phenyl-2-propenyl)-piperazine, is the most potent and specific DA uptake inhibitor ever described.[39]

Unconjugated gold nanoparticles failed to compete for dopamine binding sites, and essentially no receptor binding was observed with AuNPs alone. The mixture of dopamine and AuNPs exhibited at least 3 to 5-fold less binding than dopamine alone, and fifty percent less than DA-AuNPs. As expected, the affinity of dopamine increased with the concentration of dopamine in the mixture. When GBR12783 was added to the mixture, previous AuNP binding was reestablished. These findings suggest that the binding of dopamine and AuNP mixture was essentially due to dopamine, not AuNPs. We further infer from these results that the increase in dopamine receptor binding (as observed with DA-AuNPs) is strongest in the bound form of dopamine compared to the unconjugated form. These results also confirm that drugs conjugated

to AuNPs do not lose their biological activity, but rather may experience an enhancement in their potency.

Autoradiographic images of brain sections confirm these findings as well. In the presence of GBR 12783, binding of AuNPs (or mixture of dopamine and AuNPs) to DA receptors is turned off as shown by loss of radioactivity. DA-AuNPs also displaced dopamine radioligand, however as expected, the receptors retained some amount of DA binding in the presence of GBR 12783.
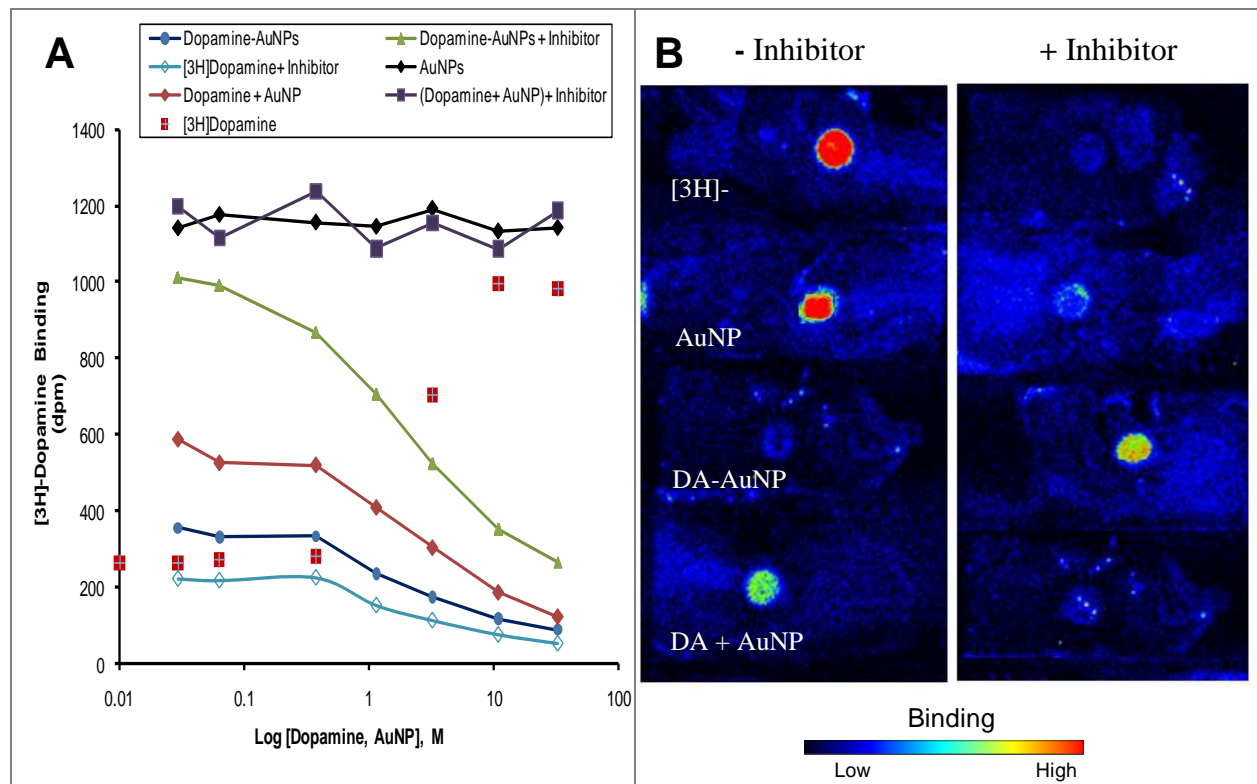

Figure 4-2-3. (A) Binding curves illustrating CHO-human D2 receptor binding with increasing dose of test agents. (B) Autoradiographic images showing [^{3}H]-DA binding in CHO human D2 receptor clone after incubation with test agents

4.2.3 Ex vivo dopamine receptor binding

Ex vivo binding and autoradiography studies of dopamine-AuNPs were conducted in striatal membrane homogenate from Sprague-Dawley rats. The baseline binding of radioligand to D2R and the changes in radioligand binding due to DA-AuNP challenge were determined. The DA-AuNPs show significantly ($p<0.05$) high affinity to central D2R, in a dose-dependent manner (Figure 4-2-4A). There is gradual and complete inhibition of [3H]-DA binding with increasing doses of DA-AuNPs. In comparison, AuNPs and other combinations tested could only partially prevent [3H]-DA binding at the highest dose concentration. A correlation therefore exists between this ability to bind D2 receptors and dose. Of all agents tested, DA-AuNPs produced the highest receptor occupancy, approaching 100% at 1uM dose. Free dopamine achieves only 80% occupancy at 1uM.

The experiments were also performed in the presence of the DA uptake blocker 1 μM GBR 12783[40] added to the medium 2 hours before sample collection. The receptor occupancy of DA-AuNP and free DA decreased in the presence of GBR 12783. However, in the presence of GBR12783, the affinity of DA-AuNP was slightly lower compared to dopamine. Loss of binding in the presence of inhibitors confirms the involvement of dopamine receptors in the binding with DA-AuNPs, and excludes off target binding.

Unconjugated NPs or a mixture of dopamine and AuNPs showed marginal binding. Once again, we can infer that bound dopamine rather than free dopamine was responsible for the increase in the affinity to D2 receptor relative to free DA. The results are consistent with findings from binding studies using human dopamine receptor whole cells, and further confirmed by autoradiographic images of brain sections. [3H]-DA were bound to receptors and then displaced

by the more potent DA-AuNPs. Digital images, obtained with β-imager, showed complete

inhibition of [3H]-DA at high doses of DA-AuNPs (Figure 4-2-4B). In comparison, a mixture of

dopamine and AuNPs could only partially prevent [3H]-DA binding. [3H]-DA binding

represents 100% D2 receptor occupancy, and was displaced from the DA receptor in the

presence of GBR12783.

The advantage of labeling the receptor on tissue sections (*ex vivo*) rather than in tissue

homogenates (*in vivo*) has been already demonstrated.[41,42] In that manner, the dissociation of the

drug-receptor complex formed in vivo can be kept minimal by immediate freezing of the brains,

omitting preincubations of the sections, and by using short incubations with the radioligand. The

short incubation time is critical for ex vivo autoradiographic protocols, particularly when the

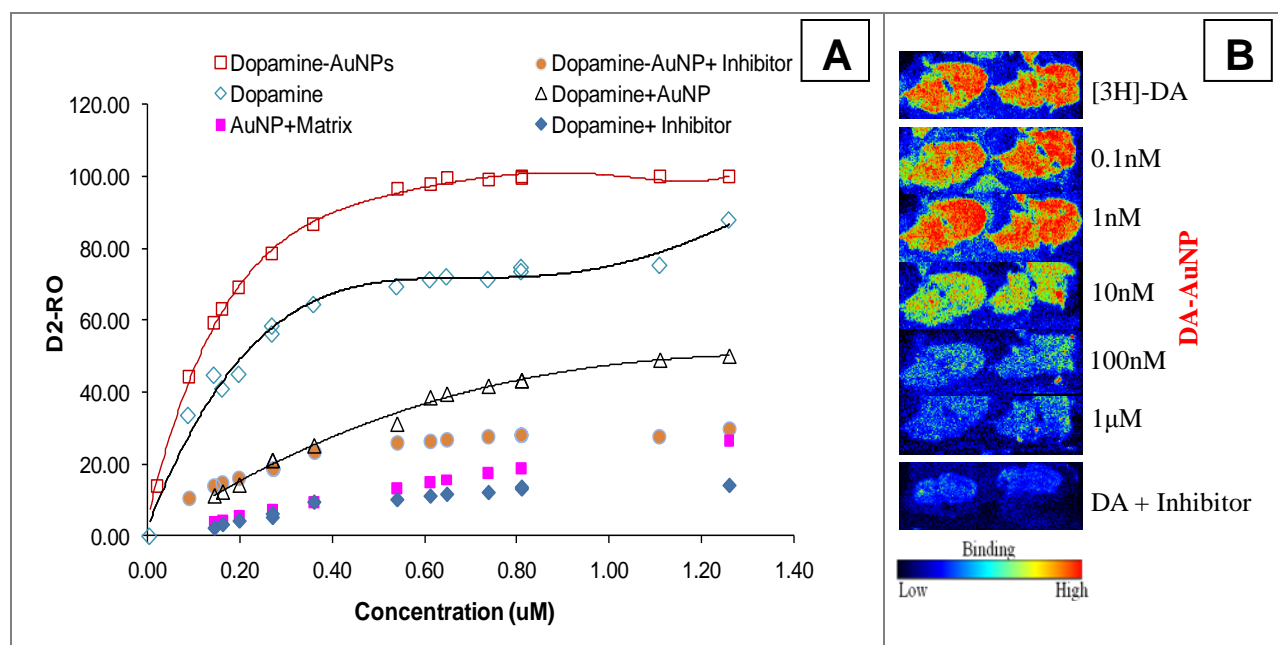method is used for evaluation of compounds with unknown properties.

Figure 4-2-4. (A) Mean binding curves illustrating the dose-dependent occupancy of D2 receptors by DA-AuNPs and derivatives in rat brain striata. (B) [3H] Dopamine autoradiographic binding in rat brain striata after treatment with increasing doses of DA-AuNPs and derivatives. Digital images obtained after acquisition with the β-imager.

4.2.4 In vivo dopamine receptor binding

Using dopamine (a poor brain penetrant) as the model drug, we investigated the effect of NP size on the binding affinity of dopamine. NPs with sizes 5, 15, 50, 100, and 200 nm were injected directly into cerebral parenchyma of Sprague-Dawley rats following pretreatment with radioligand. From the dopamine receptor occupancy curves (Figure 4-2-5A), we see that D2-RO increased with decreasing particle size of 5nm DA-AuNPs. The RO of 5, 15, 50nm AuNPs were 90%, 60%, and 20%, respectively. The 100 and 200 nm NPs each registered meager occupancies of about 5%. 5nm DA-AuNP, administered either intracranial or intravenously, provided 5 % and 10% more binding affinity, respectively than dopamine alone.

Small NPs, because of their large surface area may provide multiple sites for binding with receptors as well as promote stronger and more thermodynamically stable bonds. Furthermore, the spatial distribution of receptor binding and radioactivity in rat brain sections (Figure 4-2-5B) were confirmed in radiographic images. As expected, the dopamine inhibitor - GBR 12783, displaced dopamine from the dopamine receptor and this is reflected in the loss of radioactivity (Figure 4-2-5B).

Since receptor occupancy measurement is a good predictor of the drug free fraction available within brain interstitial space, the pharmacodynamics and efficacy after injection of DA-AuNPs can be inferred. It is expected that the AuNPs will enhance the dopaminergic effects of dopamine and potentially other CNS agents, as a result of higher brain penetration and binding conferred on drug molecules by AuNPs. However, it is unclear if DA retains the agonist binding, or switches from agonistic to antagonistic after conjugation to AuNPs. Functional assays may be needed to probe the mode of interaction between DA-AuNP and DA receptor. More studies are also needed to determine the selectivity of DA-AuNP for dopamine receptors.

5nm drug-NPs may provide a simple, inexpensive and safer alternative to radioligands for evaluating the potency of CNS drug candidate. Together these studies also show that the conjugation of dopamine to AuNPs does not diminish dopamine binding affinity. Rather, affinity and consequently pharmacological activity increased. To date, no studies have demonstrated the ability of dopamine conjugated NP to cross the BBB. This is also the first time that receptor binding studies involving NPs have been undertaken.
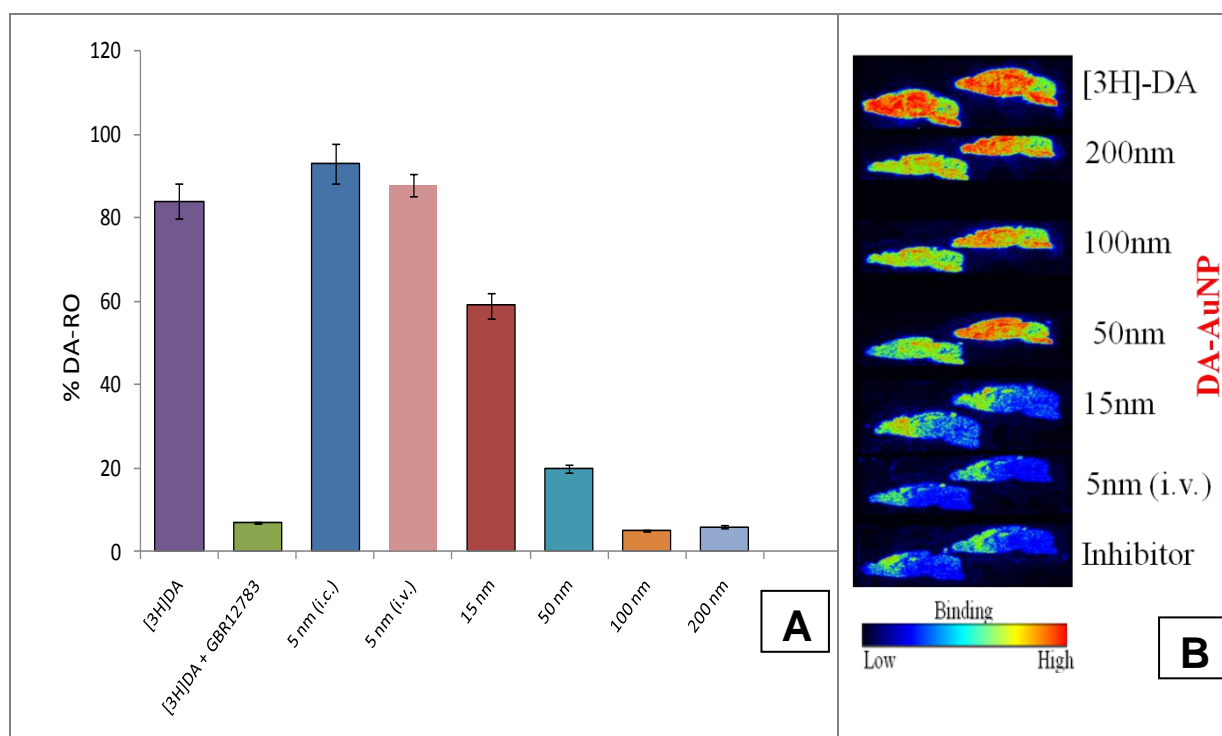

Figure 4-2-5 (A)DA receptor binding of 5-200nm DA-AuNPs in rat brain striata (B)Autoradiographic images of rat brain sagittal sections showing spatial distribution of different sizes of DA-AuNP.

4.2.5   TEM imaging of rat brain striata

The BBB penetration and distribution of DA-AuNPs in rat brain were investigated at the subcellular level using transmission electron microscopy (TEM). TEM imaging on ultra-thin sections of rat brain was used to confirm BBB penetration of DA-AuNPs after intravenous injection. The resulting TEM images showed NPs in brain parenchyma. Specifically DA-AuNPs were found inside the cytoplasm of vascular endothelial cells as well as inside neurons, which are not attached to cerebral vessels (Figure 4-2-6). The presence of DA-AuNPs inside neurons indicates that the nanoparticles diffused through the vascular endothelial cells at the BBB before reaching the cerebral parenchyma. The results provide direct evidence that in addition to effective D2R binding, DA-AuNPs penetrated the BBB and spread into the brain parenchyma. Similarly we previously demonstrated that 6-MPR-AuNPs unlike free 6-MPR could cross the BBB.[43]
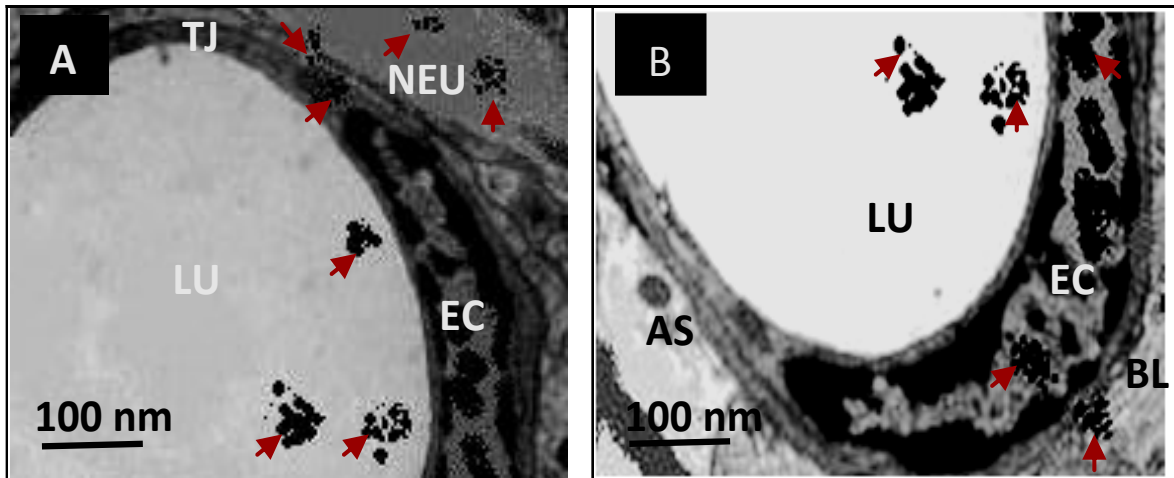
Figure 4-2-6. Electron microscopy (TEM) images of rat brain section showing gold nanoparticles inside brain parenchyma after intravenous injection with 5nm dopamine-AuNPs. AuNPs (red arrows) are shown inside the cerebral vascular lumen(LU), cytoplasm of endothelial cells (EC)and neuronal tissues. Also shown are lumen (LU), endothelial cell (EC), neuron (NEU), tight junction (TJ), basal lamina(BL), and astrocytic end-feet (AS). **A** and **B** are different views of EM slides.

4.3   CONCLUSIONS

This study was designed to answer the central question of whether conjugation of dopamine to AuNPs might enhance its brain penetration and dopamine-binding affinity to D2R. To this end, we are the first to describe the use of novel dopamine-conjugated AuNPs to overcome the low BBB permeability of dopamine, while enhancing dopaminergic receptor binding (and therefore pharmacological activity). The study shows that AuNPs enabled BBB penetration of dopamine, while maintaining dopamine efficacy. Furthermore, the AuNPs increased the binding affinity of dopamine to doparminergic receptors in the brain.

 In addition to potentially enabling unique therapies for dopamine, AuNPs may also offer a safer, more potent and inexpensive alternative to radioligands for preclinical and clinical receptor binding studies. This research also provides a drug-delivery tool for testing potential CNS drug candidates that otherwise cannot be evaluated due to lack of BBB permeability.

REFERENCES

1   Koob, G.; Nestler E.; The neurobiology of drug addiction. J Neuropsychiatry Clin Neurosci, 1997, 9, 482-497.
2   Wise, A.; Drug-activation of brain reward pathways. Drug and Alcohol Dependence 1998, 51, 2, 13-22.
3   Tarter, R.; Vanyukov, M.; Dawes, M.; Blackson, T. Etiology of early onset substance use disorder: a maturational perspective. Dev Psychopathol. 1999, 11, 657–683
4   Vallone, D.; Picetti, R.; Borrelli, E. Structure and function of dopamine receptors. Neuro and Biobehavioral Reviews 2000, 24 125–132.
5   Olanow, C.; Tatto, W.; Etiology and pathogenesis of Parkinson's disease. Annu. Rev. Neurosci, 1999, 22, 123–44.
6   Lotharius, J.; Brundin, P. Pathogenesis of Parkinson's disease: dopamine, vesicles and α-synuclein, Nature Rev. Neuro. 2002,3,1.
7   Dolan, R. Emotion, cognition, and behavior. Science 2002, 298, 1191–1194.
8   Luciano A. Clinical Presentation of Hyperprolactinemia. J. Reproductive Med. 1999, 44 (12 Suppl.), 1105-1110.
9   Roberto, P.; Gabriele, G.; Angela, P. Evidence for a pathological reduction in brain dopamine metabolism in idiopathic hyperprolactinemia Acta Endocrinol. 1991, 125, 246-252.
10 Oldendorf, W.; Blood-Brain Barrier Permeability of Drugs. Annual Review of Pharmacology. 1974, 14, 239-248.
11 Cotzias, G.; Papavasiliou, P.; Gellene, R. L-dopa in parkinson's syndrome. The New England journal of medicine, 1969,281, 5, 272.
12 Horstink, M.; Zijlmans, J.; Pasman, J.; Berger, H. Severity of Parkinson's disease is a risk factor for peak-dose dyskinesia. J. Neuro Neurosurg. Psychiatry 1990, 53, 3, 224–226.
13 Weiss, N.; Miller, F.; Cazaubon, S.; Couraud, P.; The blood-brain barrier in brain homeostasis and neurological diseases 2009, 1788, 4, 842–857.
14 Hawkins, B.; Davis, T.; The Blood-Brain Barrier/Neurovascular Unit in Health and Disease, Pharmacological Reviews 2005, 57, 173-185.
15 Reichel, A.; Addressing CNS Penetration in Drug Discovery: Basics and Implications of the Evolving New Concept. Chem and biodiversity 2009 , 6, 2030-2049.
16 Kapur, S.; Zipursky, R.; Jones, C.; Remington, G.; Houle, S.; Relationship between dopamine D(2) occupancy, clinical response and side effects: a double-blind PET study of first-episode schizophrenia. Am J Psychiatry 2000, 157, 514–520.
17 Watson, J.; Wright, S.; Lucas, A.; Clarke, K.; Viggers, J.; Cheetham, S.; Jeffrey, P.; Porter, R.; Reed, K. Receptor Occupancy and Brain Free Fraction, Drug Metabolism and Disposition 2009, 37(4), 753-760.
18 Guo, Q., Brady, M., Gunn, R., A Biomathematical Modeling Approach to CNS Radioligand Discovery and Development, Journal of nuclear medicine, 2009, 50, 10, 1715-1723.
19 Laruelle, M., Slifstein, M., Huang, Y., Relationships between radiotracer properties and image quality in molecular imaging of the brain with positron emission tomography. Mol Imaging Biol. 2003, 5, 363–375.
20 Ghosh, P., Han, G., De, M., Kim, C., Rotello, V., Gold NPs in Delivery Applications. Adv. Drug Del. Rev. 2008, 60, 1307-1315.

21 Tiwari, P.M.; Vig, Komal; Dennis, V. A.; Singh, S. R. Functionalized Gold Nanoparticles and Their Biomedical Applications. Nanomaterials 2011, 1, 31-63.

22 Hillyer J.F.; Albrecht R.M. Gastrointestinal persorption and tissue distribution of differently sized colloidal gold nanoparticles. J Pharm Sci. 2001, 90, 1927-1936.

23 Melancon, M.; Lu, W.; Li, C. Gold-based magneto/optical nanostructures: Challenges for in vivo applications in cancer diagnostics and therapy. Mater. Res. Bull. 2009, 34, 415–421.

24 Huang, Xiaohua; Jain, P.K.; El-Sayed, I.H.; El-Sayed, M.A. Plasmonic photothermal therapy (PPTT) using gold nanoparticles, Lasers Med Sci 2008 23, 217–228.

25 Hillyer, J.F.; Albrecht, R.M. Correlative instrumental neutron activation analysis, light microscopy, transmission electron microscopy, and Xray microanalysis for qualitative and quantitative detection of colloidal gold spheres in biological specimens. Microsc Microanal. 1999, 4, 481-490.

26 Hillyer, J.F.; Albrecht, R.M. Gastrointestinal persorption and tissue distribution of differently sized colloidal gold nanoparticles. J Pharm Sci. 2001, 90, 1927-1936.

27 De Jong, W.H.; Hagens, W.I.; Krystek, P.; Burger, M.C.; Sips, A.; Geertsma, R.; Particle size-dependent organ distribution of gold nanoparticles after intravenous administration. Biomaterials 2008, 29, 1912-1919.

28 Turkevich, J.; Stevenson, P.; Hillier, J.; A study of the nucleation and growth processes in the synthesis of colloidal gold, Discuss. Faraday. Soc. 1951, 11, 55-75.

29 Kimling, J.; Maier, M.; Okenve, B.; Kotaidis, V.; Ballot, H.; Plech, A.; "Turkevich Method for Gold Nanoparticle Synthesis Revisited", J. Phys. Chem. B 2006, 110, 15700-15707.

30 Podsiadlo, P.; Sinani, V.A.; Bahng, J. H.; Shi Kam, N.W.; Lee, J.; Kotov, N.A. Gold Nanoparticles Enhance the Anti-Leukemia Action of a 6-Mercaptopurine Chemotherapeutic Agent. Langmuir 2008, 24, 568-574.

31 Hall, H.; Wedel, I. Comparisons between the in vitro binding of two substituted benzamides and two butyrophenones to dopamine-D-2 receptors in the rat striaturn. Acta Pharmacologica et Toxicologica 1986, 58, 368–373.

32 Verhoeff, N.; Bobeldijk, M.; Feenstra, M.; Erdtsieck-Ernste, E.; de Bruin, K.; van Royen, E.A. In vitro and in vivo D2-dopamine receptor binding with [123I]S(-) iodobenzamide ([123I]IBZM) in rat and human brain. Int J Rad Appl Instrum B. 1991, 18 (8), 837-46.

33 Seeman, P.; Guan, H.; Civelli, O.; VanTol, H.H.; Sunahara, R.K.; Niznik, H.B. The cloned dopamine D2 receptor reveals different densities for dopamine receptor antagonist ligands. Implications for human brain positron emission tomography. Eur J Pharmacol 1992, 227, 139–146.

34 Wadenberg, M.; Kapur, S.; Soliman, A.; Jones, C.; Vaccarino, F. Dopamine D2 receptor occupancy predicts catalepsy and the suppression of conditioned avoidance response behavior in rats. Psychopharmacology. 2000,150: 422–429.

35 Amir, T., Fatma, A., Hakan, A. Gold Nanoparticle Synthesis and Characterisation. Hacettepe J. Biol. and Chem. 2009, 37 (3) 217-226.

36 Aboubakar, M.; Puisieux, F.; Couvreur, P. Study of the mechanism of insulin encapsulation in poly(isobutylcyanoacrylate) nanocapsules obtained by interfacial polymerization. J. Biomed. Mater. Res. 1999, 47, 568-576.

37 Zhou, J.; Ralston, J.; Beattie, D.; Sedev, R. Colloid stability of thymine-functionalized gold nanoparticles. Langmuir 2007, 23(24):12096-103.

38 Ariyasu, S.; Onoda, A.; Sakamoto, R.; Yamamura, T. Conjugation of Au11 cluster with Cys-rich peptides containing the α-domain of metallothionein. Dalton Trans. 2009, 21, 3742-3747.

39 Allison, D.; Mentore, J.; Heo, M. Antipsychotic-induced weight gain: a comprehensive research synthesis. Am J Psychiatry 1999, 156(11), 1686-1696.

40 Bonnet, J., Costentin, J. GBR 12783, a potent and selective inhibitor of dopamine uptake: biochemical studies in vivo and ex vivo. Eur J Pharmacol 1986, 121(2), 199-209.

41 Schotte, A.; de Bruyckere, K.; Janssen, P.; Leysen, J. Receptor occupancy by ritanserin and risperidone measured using ex vivo autoradiography. Brain Res. 1989, 500, 295-301.

42 Schotte, A.; Janssen, P.; Megens, A.; Leysen, J. Occupancy of central neurotransmitter receptors by risperidone, clozapine and haloperidol, measured ex vivo by quantitative autoradiography. Brain Res. 1993, 631,191-202.

43   Nkansah, P.; El-Kattan, A.; Rago, B.; Poe, J.; Bommana, M.; Merzlikine, A.; Varma, M.; Rotter, C.; Thomas, V.H.; Kotov , N. Brain Penetration, Distribution and Pharmacokinetics of 6-Mercaptopurine Riboside Conjugated Gold Nanoparticles (Thesis 2013: Chapter 3).

CHAPTER 5

THESIS CONCLUSION

5.0   FUTURE RESEARCH AND PERSPECTIVES

5.1.1 Central nervous system nanonotherapeutics

Application of nanotechnology to neuroscience is already having significant effects, which will only continue for the foreseeable future. In the coming years, nanoparticles will provide simultaneous brain imaging, diagnostics and therapy (so-called theranostic). Similarly, intelligent molecular "trojan horse" will someday be able to effectively ferry drugs and non-viral plasmid DNA into the brain. Nanoparticles can facilitate this by binding to an exofacial epitope that is spatially removed from the binding site of the endogenous ligand on the BBB receptor. This will allow drug nanoparticles to "piggy back" across the BBB via receptor-mediated transytosis without interfering with endogenous transport systems. In the next decade it is expected that new multifunctional therapeutics consisting of a homing device for targeting, imaging moiety for sensing/imaging, and drug therapy will translate into clinical use.

Future brain targeting studies involving nanoparticles will need to determine the extent, rate, and effect of drug and nanoparticle uptake into the brain. Parameters like administration route, sampling time points, and the way in which the data are presented should be taken into account. Furthermore, the intracellular fate of nanoparticles, remains unclear. There is limited information on the effect of the physicochemical properties of nanoparticles on their distribution, cellular uptake, metabolism, accumulation and elimination. Also, though several mechanisms

including receptor mediated endocytosis have been proposed to explain nanoparticle transport across the BBB, more investigations are still needed to fully elucidate the binding, brain uptake and transport mechanism of gold nanoparticles. Finally, faster and more sensitive detection methods are needed to study uptake and trafficking of nanoparticles in biological systems. Current static imaging techniques for studying the biodistribution of nanoparticles cannot detect small fractions of nanoparticles in vascular beds, blood stream, and inner organs of the body.

5.1.2. Nanotoxicity

One significant benefit of nanoparticles as a drug carrier is the prolonged mean residence time in the body. While this may desirably increase the exposure of drugs to disease targets, it can also increase toxicity. This is especially true for nanoparticles because of their large surface area, and therefore unique physicochemical and biological properties.[1,2] Nanoparticles may also have the potential for generating free radicals and exhibit oxidative tendency depending on their surface characteristics. There are only a few long term toxicology studies on nanomaterials, primarily SiO_2, CNT, and TiO_2. The available information indicates that certain nanoparticles may be genotoxic or phototoxic. However, the toxicokinetics and metabolism of nanomaterials have not been studied in detail. In particular, there is limited information about how the physicochemical parameters of nanoparticles affect absorption and transport across barriers of skin, gut, lungs and eyes. Additionally, the accumulation, metabolism and excretion from secondary target organs require further research.

Current studies with 6MPR-conjugated AuNPs or dopamine-conjugated AuNPs were well-tolerated with no adverse events observed. However, there is still a need for data-extensive

toxicological evaluation of AuNPs and other metal nanoparticles with respect to their systemic and CNS effects. These questions are well outside the scope of this thesis.

5.2 CONCLUDING REMARKS

The vast majority of small molecule drugs (>98%) do not cross the BBB, and therefore cannot treat CNS diseases. As discussed in chapter one, several strategies to get drugs across the BBB have been attempted, with limited success. These involve direct injection of drugs into the brain, transport via the olfactory and trigeminal nerves innervating the nasal passages, or opening of BBB tight-junctions by means of osmotic agents, as well as exploiting endogenous transport systems within the BBB using medicinal chemistry strategies.

Several studies are available on the utility of AuNPs for diagnostic and therapeutic applications. However, there are no reported cases of using AuNPs to enhance the brain penetration and pharmacological activity of CNS drugs. Therefore, in this thesis, we describe the successful use of a novel CNS drug delivery system involving conjugating drugs to 5nm AuNPs. We combined detailed in vitro and in vivo experiments with imaging and bioanalytical techniques to investigate the pharmacokinetics, BBB penetration, and receptor binding of drugs conjugated to AuNPs. Specifically, we demonstrated that 6-MPR and dopamine conjugated to AuNP are able to cross the BBB into brain parenchyma.

Our findings also show that AuNPs significantly inhibit xanthine oxidase metabolism of 6-MPR. Finally, based on receptor binding experiments with dopamine-AuNPs, it is observed that the AuNPs not only enabled brain penetration of dopamine, but they also increased the binding affinity of dopamine to dopaminergic receptors in the brain. To our knowledge, this is the first time transvascular delivery of a therapeutic agent across the BBB (with the possibility of also enhancing drug receptor-binding potential) has been achieved using small AuNPs.

Even though the present study primarily focused on the brain uptake of model

compounds (6-MPR and dopamine), the strategy described here is applicable to a wide range of

drug candidates with low BBB permeability. Future advances in CNS biology, neuroimaging and

bioanalytical techniques, specifically as they pertain to nanoscale systems, will provide further

insights into the design, performance and toxicity of drug delivery systems involving

nanomaterials.

REFERENCES

1 Soenena, S.J.; Rivera-Gilb, P.; Montenegrob, J-M.; Parakb, W.J.; De Smedta, S.D. Cellular toxicity of inorganic nanoparticles: Common aspects and guidelines for improved nanotoxicity evaluation, Nano Today. 2011, 6 (5), 446–465.
2 Karakoti, A.S.; Hench, L.; Seal, S. The potential toxicity of nanomaterials – the role of surfaces. J Miner, Met Mater Soc. 2006, 58, 77–82.